Design of High Energy Particle Detectors for Lunar and Low Earth Orbit Missions

by

Katelyn Ball

A thesis submitted in partial fulfillment of the requirements for the degree of

Master of Science

Department of Physics and Department of Electrical Engineering

University of Alberta

Abstract

The study of energetic particles of solar and cosmic origin, and those accelerated in the planetary magnetopause, is integral to our developing understanding of the physical processes affecting space radiation in near-Earth space, interplanetary space, and Earth's upper atmosphere. In particular, accurate forecasting of space radiation is crucial when developing radiation risk assessment and mitigation strategies for human and robotic space exploration. This thesis presents an assessment and optimization of the layout and detection performance for three energetic particle telescopes designed for operation on the lunar surface, on-board the Lunar Gateway, and low Earth orbit (LEO). Geant4 monte carlo simulations are carried out to optimize each instrument's response to the expected particle populations at their respective vantage points in space. The instruments use a stack of silicon detectors to measure the particle's energy deposition, which is processed through algorithms designed to identify the particle's species and energy.

The Lunar Lander SWeeping Energetic Particle Telescope (LL-SWEPT) is designed for a 14-day mission on the lunar surface. LL-SWEPT is primarily focused on assessing the relatively constant radiation risk due to Galactic Cosmic Rays (GCRs), as well as the secondary albedo particles from the lunar regolith. To measure statistically significant counts of GCR flux, LL-SWEPT has a geometric factor of 1.3 cm^2sr. Two energy identification regimes are used to measure lower (<165 MeV) and higher energy protons from LL-SWEPT's count rate data, enabling LL-SWEPT to make differential proton measurements with energies from 20 to 370 MeV, which extends past its required measurement range of 30 to 300 MeV. LL-SWEPT is also able to measure alpha particles with energies from 80 to 660 MeV.

The Planetary Sweeping Energetic Particle Telescope (P-SWEPT) is optimized to operate on the Lunar Gateway. It has been shown that electrons accelerated from the Sun during solar energetic particle (SEP) events can reach Earth up to an hour before the proton flux, which provides the potential for an advance warning of strong SEP events. P-SWEPT prioritizes the measurement of proton and electron populations in SEP events, and its geometric factor of 0.113 cm^2sr is suitable for higher flux measurements. The energy identification regimes allow P-SWEPT to measure electrons with energies from 0.3 to 1.5 MeV and protons with energies from 22 to 400 MeV, which covers and extends past P-SWEPT's proton energy measurement requirement of 20 to 300 MeV.

The RADicals High Energy Particle Telescope (RADHEPT) is a particle telescope suite set to fly on the upcoming RADiation Impacts on Climate and Atmospheric Loss Satellite (RADICALS) mission. The instrument suite on the RADICALS mission will study the processes which control space radiation precipitation into the atmosphere. The RADHEPT instrument is designed to measure electrons with energies from 0.08 to 4.4 MeV and protons with energies from 1 to 70 MeV, exceeding RADHEPT's measurement requirement for protons, 1 to 20 MeV, and electrons, 0.1 to 3 MeV. To make pitch angle resolved particle measurements, RADHEPT is required to measure particle count rates over six orders of magnitude. To do so, RADHEPT is comprised of two telescopes with geometric factors suitable to measure both the higher energy, low flux particles and the lower energy, high flux particles. The preliminary layout and detector performance of the high and low energy heads of RADHEPT are presented here as well as a scheme to use an anti-coincidence scintillator to detect off axis particles.

The three instruments presented here will enable higher fidelity measurements of the radiation environment on the lunar surface, and in lunar and low Earth orbit, all of which are of significant importance both for the safety of future space exploration missions and impacts on the Earth's upper atmosphere.

Acknowledgements

Thank you to my supervisors, Dr. Ian Mann and Dr. Robert Fedosejevs, who allowed me to explore both the space physics and electrical engineering fields with unwavering support and guidance. Special thanks to Louis Ozeke and Henry Tiedje for their advice and collaboration on many aspects of this thesis. Thank you to my friends and family, particularly to my parents, Lisa, and Ethan for your continuous support and providing perspective on my work.

I am lucky to be apart of such a special community at the UofA where being exactly who you are and being passionate about your work is celebrated. Many thanks to all the folks within the UofA Space Physics group and AlbertaSat past and present who made my time at the UofA an eight year adventure.

Contents

List of Tables

List of Figures

Acronym List

LEO Low Earth Orbit

LOP-G Lunar Orbital Platform-Gateway

LL-SWEPT Lunar Lander Sweeping Energetic Particle Telescope

P-SWEPT Planetary Sweeping Energetic Particle Telescope

RADHEPT RADICALS High Energy Particle Telescope

RADHEPT-LE RADICALS High Energy Particle Telescope: Low Energy

RADHEPT-HE RADICALS High Energy Particle Telescope: High Energy

RADICALS RAdiation Impact on Climate and Atmospheric Loss Satellite

SEP Solar Energetic Particle

GCR Galactic Cosmic Rays

IMF Interplanetary Magnetic Field

CME Coronal Mass Ejection

PCA Polar Cap Absorption

HF High Frequency

L1 Lagrange Point

SSA South Atlantic Anomaly

EMIC Electromagnetic Ion Cyclotron

FOV Field of View

Geant4 GEometry And Tracking 4

ADC Analog to Digital Converter

FPGA Field Programmable Gate Array

CSDA Continuous Slow Down Approximation

NIST National Institute for Standards and Technology

TRIUMF TRI-University Meson Facility

SAPPHIRE Solar Accumulated and Peak Proton and Heavy Ion Radiation Environment

SEPEM Solar Energetic Particle Environment Modelling

COSTEP COmprehensive Suprathermal and Energetic Particle analyzer

SOHO SOlar and Heliospheric Observatory

MAVEN Mars Atmosphere and Volatile EvolutioN

MEPED Medium Energy Proton and Electron Detector

POES Polar Orbiting Environment Satellite

NOAA National Oceanic and Atmospheric Administration

Chapter 1

Introduction

1.1 Thesis Motivation

The continuous flow of energetic charged particles of solar and cosmic origin, called space radiation, drives countless processes in near-Earth space and throughout the Solar System. It is also extremely dangerous - even within the protective shield of Earth's magnetic field, a sudden burst of energetic particles from the Sun is capable of catastrophic damage to electronics and other infrastructure on satellites and can affect human health in a matter of hours. This issue is especially important for astronauts living and working outside Earth's magnetic field. A better understanding of the nature of space radiation within our solar system is essential to the safety of future generations of astronauts, especially in deep space, and to better understand the potential impact on the technological systems upon we increasingly rely upon on Earth.

This thesis presents research addressing the optimization of the geometry and particle identification regimes of energetic particle telescopes designed for three applications: to measure protons and alpha particles of solar and cosmic origin on the lunar surface and in lunar orbit on the Lunar Orbital Platform-Gateway (LOP-G), and to measure trapped and untrapped electron and proton populations in the Earth's Van Allen radiation belts. The Lunar Lander Sweeping Energetic Particle Telescope (LL-SWEPT) is designed for the lunar surface, the Planetary Sweeping Energetic Particle Telescope (P-SWEPT) is designed for flight in lunar orbit on the LOP-G, and the RAdiation Impact on Climate and Atmospheric Loss Satellite (RADICALS) High Energy Particle

Telescope, comprising of: RADICALS High Energy Particle Telescope: High Energy (RADHEPT-HE) and RADICALS High Energy Particle Telescope: Low Energy (RADHEPT-LE) is designed for LEO.

In this chapter, an overview of the space environments where LL-SWEPT, P-SWEPT, RADHEPT-HE, and RAD-HEPT-LE will operate is provided. Solar Energetic Particle (SEP) events and Galactic Cosmic Rays (GCR), the two primary radiation sources LL-SWEPT and P-SWEPT measure are detailed. Next, the structures inside the magnetosphere are described, and an explanation on how space radiation is able to permeate the Earth's magnetic field and an overview of the Van Allen radiation belts is given. Finally, some of the processes by which electrons are trapped in LEO and precipitated down to the atmosphere are detailed.

1.2 Sources of Space Radiation

In this section, an overview of the processes which accelerate particles that all three instruments measure is presented. Information on how particles interact with Earth's magnetic field and their characteristics on the surface of the moon is also provided. These topics provide the necessary context to understand the environment each instrument will operate in and the derived measurement requirements.

1.2.1 Particles Travelling from the Sun

A significant portion of the particles the instruments are designed to measure originate from the Sun and travel outwards in the solar wind. The solar wind is a plasma with an ion composition of protons ($\sim$ 96%), alpha particles ($\sim$ 4%), and trace amounts of heavier ions, generated during the nuclear fusion process at the Sun's core (e.g., Wurz, 2005). The heavy particles are created as intermediate products of the fusion process inside the sun's core, with a small percentage expelled from other stars and becoming trapped in the Sun's magnetic field. The solar wind extends outwards reaching past the edges of the Solar System, creating the region of space called the Heliosphere. Some ions

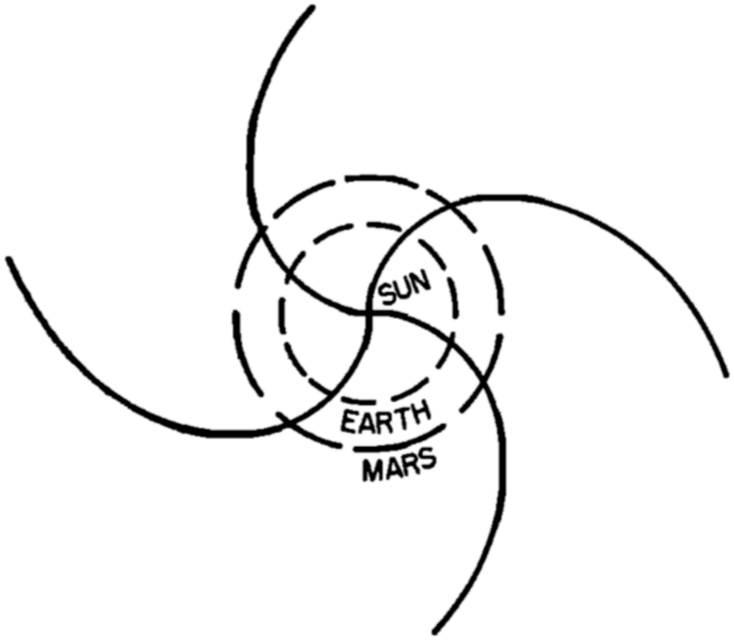

Figure 1.1: Illustration representing the interplanetary magnetic field IMF in the Parker spiral shape frozen in to the solar wind plasma environment (taken from Parker, 1959).

on the Sun's surface are able to escape the Sun's gravitational force through coronal holes, where the magnetic field lines stretch out into interplanetary space rather than creating a closed coronal loops. Solar wind accelerated through corona holes is called fast solar wind, travelling with a speed of around 600 to 800 km/s. Fast solar wind is relatively stable over time in terms of ion composition and speed. Slow solar wind, travelling at 300 to 500 km/s, can originate from the Sun's equatorial streamer belt and is highly variable and turbulent over the 11-year solar cycle (Cranmer, 2005). The solar wind also carries the Interplanetary Magnetic Field (IMF) with it, which is essentially frozen into flow of the solar wind. As the Sun rotates, the solar wind and the IMF become a spiral about its rotation axis. This property of the solar wind was proposed first by Parker in 1959, leading to the phenomena being known as the Parker spiral sketched in Figure 1.1.

1.2.2 Solar Energetic Particle Events

Fast and slow solar wind are continuously travelling from the Sun, and its properties such as flux and composition change and do so abruptly during Coronal Mass Ejection (CME) events.

More energetic particles can also be accelerated close to the sun, such as during CMEs, or in association with solar flares, or at magnetic shock fronts in the solar wind. For example, energetic particles ranging from a few keV to GeV energies can be ejected from the solar surface into interplanetary space (e.g., Malandraki and Crosby, 2018). When they occur, SEP events are the dominant radiation source in the near Earth environment and have the potential to harm humans and infrastructure orbiting outside the Earth's magnetic field. Polar Cap Absorption (PCA) occurs when particles from SEP events precipitate into Earth's polar regions and ionize the D-layer of the ionosphere (50-90 km), causing interruptions to High Frequency (HF) radio signals used for communications in many industries, such as marine, airlines, and shipping (e.g., Fiori, 2020). SEP events can last between hours and days and their timing and intensity are hard to predict. However, the number and intensity of SEP events is correlated with the solar cycle. Figure 1.2 shows the long-term relationship between solar cycle and SEP proton energy spectra and intensity with the OMNI2 data set (data source: https://omniweb.gsfc.nasa.gov/html/ow_data.html5) .

SEPs can reach the Earth from the Sun within one hour, much quicker than the ambient solar wind. The directionality of the particle flux during a SEP changes throughout the event. At the beginning of the SEP, the particle flux is typically in the direction of the IMF, and gradually becomes isotropic. The time it takes for the SEP flux to become more isotropic decreases for large SEP events. For very large events, the particles can deviate and scatter from the magnetic field lines in the IMF, making the directional SEP flux even more unpredictable.

The ionizing radiation present in SEPs are considered the most variable, unpredictable, and intense radiation threat for astronauts and spacecraft.

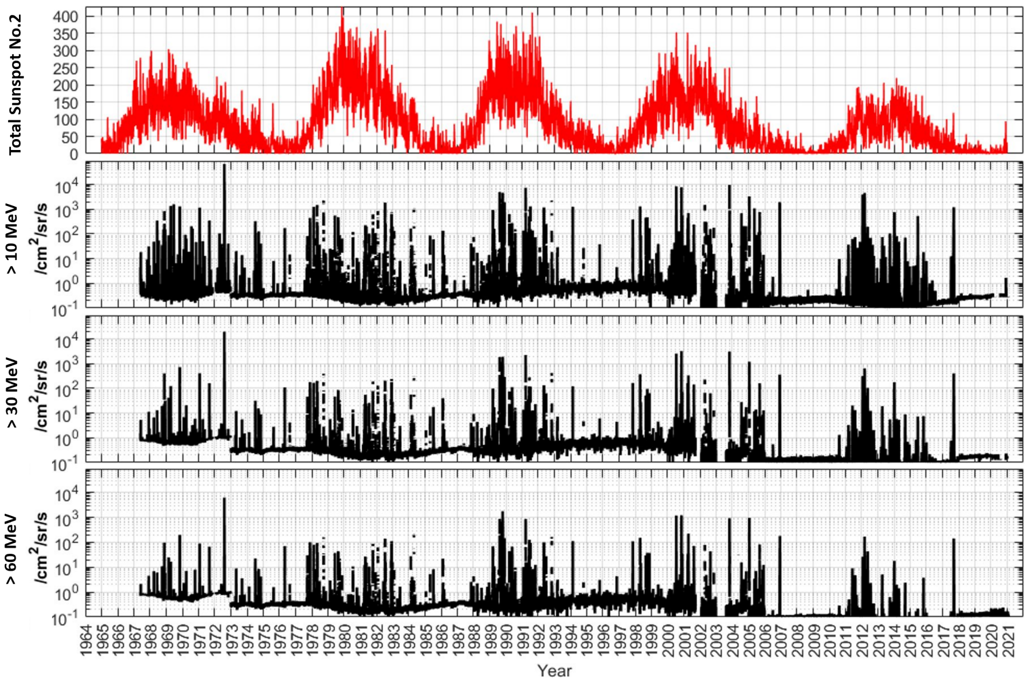

Figure 1.2: Integral proton flux from 1967 to 2019 as a function of solar cycle measured by several spacecraft in geocentric or L1 orbits. Plot courtesy of L. Ozeke.

1.2.3 Galactic Cosmic Rays

A second source of space radiation that the instruments will measure is GCR. GCR flux is nearly isotropic, mostly comprised of protons (87%), alpha particles (12%) and trace amounts of heavy nuclei (e.g., Dunai, 2010). GCRs travel to the near Earth space environment from the remnants of distant supernova and other cosmic objects, and enter the Solar System at near-light speeds with energies up to 10 GeV. Most of the GCRs are blocked by the heliosphere, the region of space around the Sun that is influenced by the IMF. Unlike SEP events, GCRs are continuous, very predictable and have a much lower flux. The intensity of GCRs have an anti-correlation with the solar cycle (e.g., Ross and Chaplin, 2019). GCR flux can become unstable when interacting with magnetic fields associated with large CMEs. The phenomenon is called a Forbush decrease, and they can result in a sharp decrease of up to 20 % of the previous GCR flux, followed by a recovery period which can last days. (e.g., Kilifarska et al., 2020).

1.2.4 Secondary Particle Generation

The third source of radiation in the space environment the instruments measure is radiation due to secondary particle generation. As particles from SEPs and GCRs interact with spacecraft material, they interact with atomic nuclei and generate neutrons and other secondaries. The amount of secondary neutron production depends on the incident particles, shielding material and thickness (Heilbronn et al., 2005). Neutrons and other heavy ions deposit more energy per material unit length, resulting in a larger radiation dose and risk to astronauts (Naito et al., 2020). LL-SWEPT and P-SWEPT are the instrument applications which will be operating close to or on crewed spacecraft where secondary neutron production is especially concerning for human health.

1.3 Near-Earth Space Environment

1.3.1 The Magnetosphere

The IMF and solar wind interact with Earth's magnetic field, creating a complex and dynamic space environment around the Earth. The dynamic pressure of the solar wind and Earth's geomagnetic field come to equilibrium at the magnetopause, the boundary of the magnetosphere. Solar wind primarily travels toward the dayside of the Earth, compressing the magnetopause on the dayside to a standoff distance of about 10 Earth radii. Upstream of the magnetopause boundary, the solar wind slows down at the bow shock. The majority of the solar wind is deflected by the magnetopause and travels around the Earth. On the nightside, the magnetic field lines are stretched, giving the magnetopause a bullet-like structure. The northern and southern magnetic lobes of the nightside magnetopause meet at 200 Earth radii down-tail, defining the magnetotail. See Figure 1.3 for a schematic diagram of the magnetopause structure. The shape of the magnetopause varies heavily with solar activity. Above Earth's magnetic poles at the polar cusp, solar wind is able to permeate the magnetopause by funneling downward along Earth's magnetic field lines.

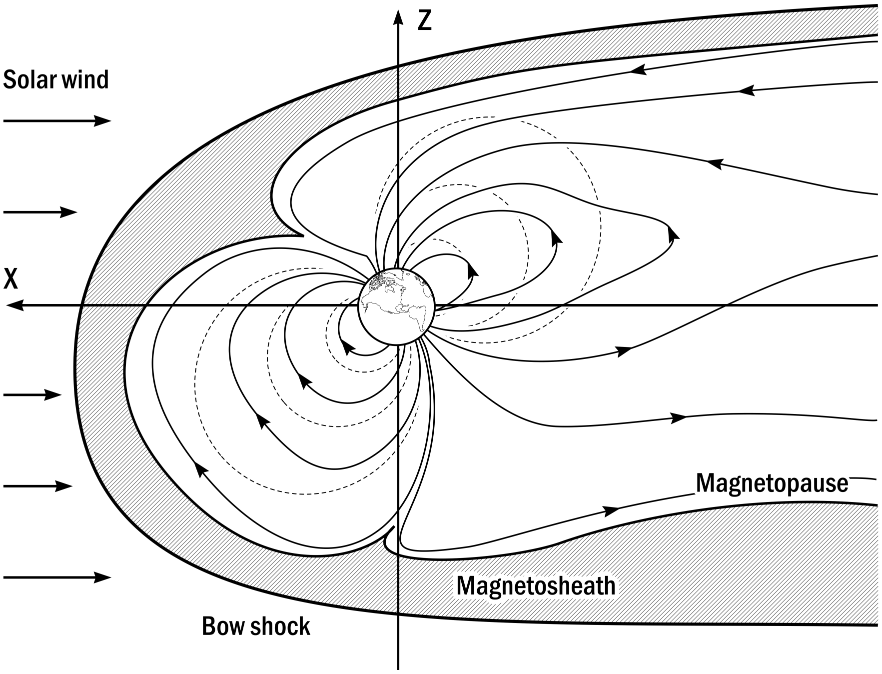

Figure 1.3: Schematic of the Earth's magnetic field, showing the bow shock, and magnetopause. The closed solid lines show the shape and direction of Earth's magnetic field. The dotted lines show a true dipole, for comparison. Photo credit: Andy Kale.

In the northern and southern polar regions, two ovals comprise the Aurora Borealis and Aurora Australis, light emitted as energetic charged particles of solar and terrestrial origin collide with the atmosphere. Outside the polar cusp regions, spatio-temporal fluctuations in the magnetopause allow some particles to penetrate it, especially during periods of strongly southward IMF. Inside the magnetopause boundary is the magnetosphere, the region of space where the dominant magnetic field is that of the Earth. Plasma in the magnetosphere makes up different regions that vary in temperature and density (e.g., Sadiq, 2012). Figure 1.3 shows the magnetic field around Earth and the distortion in the magnetosphere as a result of interaction with the solar wind.

Radiation Belts

Energetic charged particles in the magnetosphere can be trapped in two doughnut shaped rings surrounding the Earth called the Van Allen radiation belts.

The inner Van Allen belt begins at 640 km and extends to 1.0×10^4 km from the Earth's surface and traps mostly protons with energies from 10 MeV to 1 GeV (Selesnick et al., 2014), along with electrons with energies $<$900 keV (Fennell et al., 2015), and a few heavier elements (e.g., Walt, 1994). The origin of the charged particles trapped in the inner belt is partially from the interaction of solar and cosmic energetic particles with the Earth's neutral atmosphere and is generally more stable in particle density and energy than the outer belt (e.g., Li and Hudson, 2019). The outer belt ranges from 1.3×10^4 to 5.8×10^4 km and mostly contains trapped relativistic electrons with energies $>$0.5 MeV (Walt, 1994). The outer belt's shape and density is very dynamic and can change by orders of magnitude in a matter of hours in response to changes in the outer magnetosphere driven by solar activity.

Charged particles in the Van Allen belts are accelerated by plasma waves in the Earth's magnetic field and have unperturbed motion which is characterized by three types of periodic motion: cyclotron motion about the magnetic field lines, bounce motion along the field lines and drift motion around the Earth.

Due to the Lorentz force, ions and electrons have a perpendicular component to their motion travelling around the magnetic field in a circular motion. The radius of gyration, called the Larmor radius, is dependant on the mass, m, and charge of the particle, q, its velocity perpendicular to the magnetic field, $v_\perp$, and the magnetic field strength, B, and is given for non-relativistic particles by Equation 1.1.

$$r_g = \frac{mv_\perp}{|q|B} \tag{1.1}$$

In the case of a uniform magnetic field, the charged particles travel in a circular motion perpendicular to the magnetic field. While traveling along the field lines in a non-uniform magnetic fields such as Earth's, the radius of the charged particle orbit changes as it is inversely related to the magnetic field strength. The particles gain or lose speed in the direction parallel to the magnetic field as it decreases or increases the strength, respectively (e.g., Schumacher, 2005).

For particles trapped in the radiation belts, it can be assumed that their gyration frequency is much larger than the background magnetic field's rate of change and can be considered static over the particle's gyration period. Under this condition the particle's magnetic moment is conserved, similarly on the bounce and drift timescales. Three adiabatic invariants associated with the three types of periodic particle are therefore conserved. The first adiabatic invariant, μ, describes the particles gyration around the magnetic field lines:

$$\mu = \frac{mv_{\perp}^2}{2B} = \frac{mv^2}{2}\frac{sin^2(\alpha)}{B}. \tag{1.2}$$

Here $v_{\perp}$ is the component of the particle's velocity perpendicular to the magnetic field and α is the pitch angle, the angle between the particle's velocity vector and the magnetic field, B. Conservation of the first adiabatic invariant causes the pitch angle to increase as the particle drifts to a region of higher magnetic field. The second adiabatic invariant, J (Equation 1.3), relates to the bounce motion of particles travelling between two mirror points in the northern and southern hemisphere along over length s:

$$J = m \oint_{s} v_{\parallel} \mathrm{ds}. \tag{1.3}$$

Where $v_{\parallel}$ is the particle's velocity component parallel to the magnetic field. As particles travel into regions of increasing B-field, the perpendicular velocity component must increase to keep the adiabatic invariant constant, see Equation 1.2 (e.g., Schumacher, 2005). While assuming static magnetic field over the particle's gyration period, and without any accelerating electric fields acting, the total kinetic energy of a particle remains constant, causing the parallel component of the particle's velocity to reduce. At a point in the particle's motion along the magnetic field, the B-field is sufficiently large to stop the parallel motion of the particle. At this point, all the particle's motion is in the perpendicular direction and it bounces back along the field line, regaining kinetic energy in the parallel direction and heads for the equatorial region. The upper and lower limits of the particle's motion are called the mirror points and their latitude depends on the magnetic field profile along the field, and the equatorial pitch angle. Due to their opposing charges, electrons and protons travel in different directions along the magnetic field lines.

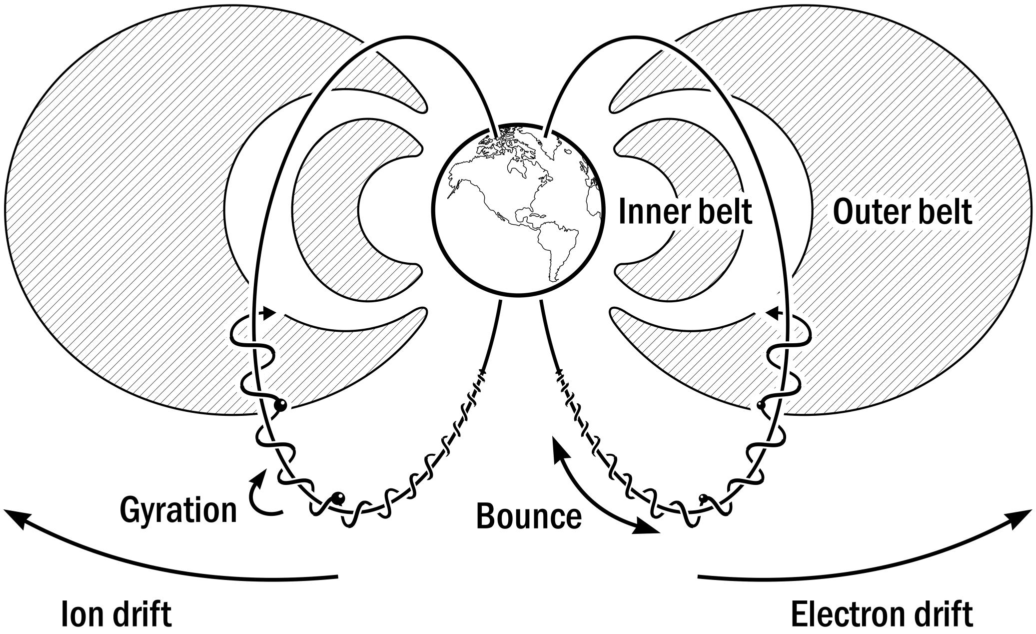

Figure 1.4: Schematic showing the three types of particle motion in the Van Allen radiation belts due to the Earth's magnetic field. Photo credit: Andy Kale.

The third and final motion particles experience in the radiation belts is the slower, longitudinal drift about around the Earth and is governed by the third adiabatic invariant. The third adiabatic invariant states that the total magnetic flux enclosed by the drift surface remains constant over the particle's motion. Like the bounce motion, oppositely charged ions and electrons travel in opposite drift directions, with electrons travelling eastward and positive ions travelling westward. The drift period depends on the energy of the particle, pitch angle and the ambient magnetic field. Figure 1.4 shows the three types of periodic motion that govern particle motion in the Van Allen belts. A more comprehensive description of these three types of periodic motion is presented in text (such as Northrop, 1963 and Chen, 2016) .

The Ionosphere

UV rays incoming from the Sun travel through the magnetosphere and are able to interact with the Earth's neutral atmosphere and ionize particles. Where the atmosphere is more dense, ions recombine and return to a neutral state, but in sparsely populated regions, recombination is less common. This creates a conductive region of the atmosphere called the ionosphere and ranges from 60 to 500 km above the Earth's surface (e.g., Hargreaves, 1992). Like most phenomena in the near-Earth environment, the density, size and temperature of the ionosphere changes with solar activity.

1.3.2 Particle Precipitation into the Atmosphere

As mentioned in Section 1.3.1, particles spiraling about magnetic field lines bounce at mirror points and reflect back to areas of weaker magnetic field. However, the magnetic mirroring only occurs if the particle bounces prior to reaching Earth's neutral atmosphere. The maximum pitch angle in which a particle will mirror above the atmosphere and become trapped at a given longitude is called the bounce loss cone. The angular width of the bounce loss cone is dependant on the ratio of the magnetic fields at the equator to the top of the atmosphere ($\sim$ 100 km).

As mentioned in Section 1.3.1, particles, depending on their charge, slowly drift either westward or eastward around the Earth. The bounce loss cone varies in size at different longitudes on the Earth, partially due to the misalignment between the Earth's rotation axis and its magnetic poles. The areas with the lowest magnetic field strength, and the largest bounce loss cone, define the drift loss cone angle. A particle with a pitch angle in between the bounce and drift loss cone will remained trapped until it drifts into an area of low magnetic strength, such as the South Atlantic Anomaly (SSA) where the local bounce loss cone increases above the particle's pitch angle, and the particle will precipitate. More information on particle behaviour at varying pitch angles can be found in Rodger et al.

Particles in the radiation belts enter the loss cone through wave-particle interactions with plasma waves such as Electromagnetic Ion Cyclotron (EMIC) waves (e.g., Kersten et al., 2014), plasmapheric hiss (e.g., Thorne et al., 1973), and chorus waves (e.g., Shprits et al., 2016). Another theory proposes particles are lost outward through the magnetopause by magnetopause shadowing (e.g., Turner et al., 2012). Wave-particle interactions and magnetopause shadowing

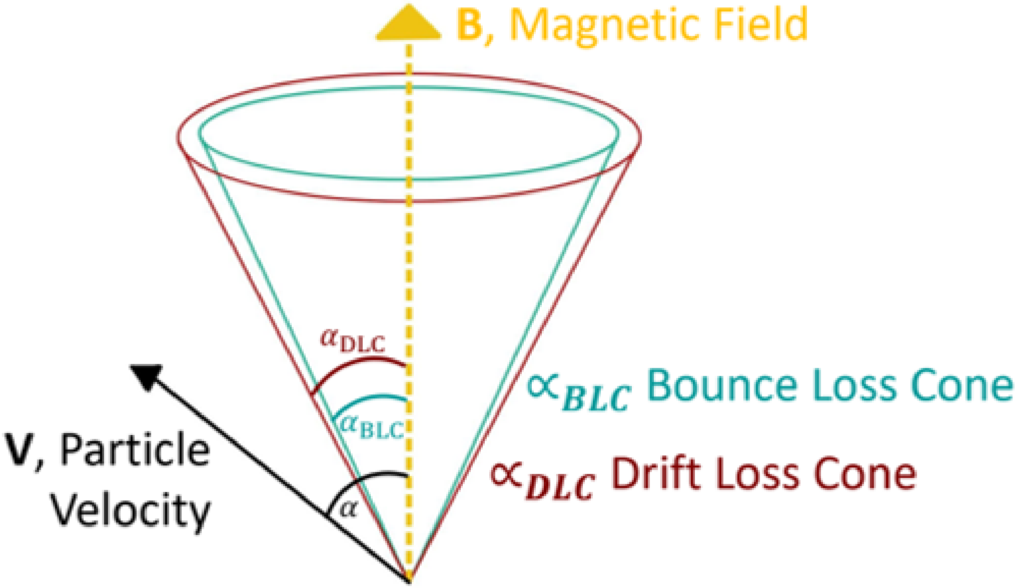

Figure 1.5: A schematic of the bounce and drift loss cone, compared to a charged particle with pitch angle α. The particle's pitch angle is defined as the angle between the particle's velocity vector and the magnetic field. The bounce loss cone (α_{BLC}) is defined as the pitch angle of particles that will reach the atmosphere before mirroring at a given longitude. The drift loss cone (α_{DLC}) is defined as the largest bounce loss cone the particle will experience as it drifts around the Earth. The particle in this schematic has a pitch angle outside both the drift and bounce loss cone, so its mirror point is above the atmosphere and will be trapped along the magnetic field line.

are both believed to cause significant effects on the properties, dynamics, particle populations and densities that exist in the radiation belts. The relative contributions of magnetosphere shadowing and wave-particle interactions to pitch angle scattering loss is a continuing debate in space physics.

1.3.3 Thesis Outline

Chapter 2 presents the details of the physics behind the energetic particle identification methods used in the three telescope applications. Previous work on the development of the University of Alberta design for these energetic particle telescopes will also be discussed, to provide background for the progress reported in this thesis. The open source software GEometry And Tracking 4 (Geant4) used to conceptualize the instruments layout and determine its performance is also summarized. An overview of each telescope application is given, including the purpose, scientific objectives and measurement requirements.

Chapters 3, 4 and 5 detail the progress made on the optimization of the energy identification aspects of LL-SWEPT, P-SWEPT and RAD-HEPT. Baseline geometries for each telescope application are presented. The driving design factors are the Field of View (FOV), the geometric factor, dictated by expected count rates, and the shielding thicknesses, dictated by acceptable dead time periods of maximum expected particle flux.

Chapter 3 shows that LL-SWEPT is able to measure alpha particles with no changes from the layout originally designed to measure protons. A new algorithm is developed to measure the high energy protons that travel through the entire detector stack, which can be used with the original logic binning to increase the measurement range of LL-SWEPT.

Chapter 4 overviews the P-SWEPT baseline geometry. A small augmentation in P-SWEPT's geometry is presented to give P-SWEPT the ability to measure electrons that precede the more dangerous proton flux during SEP events. A detailed dead time analysis is presented which determines P-SWEPT's ability to make scientifically meaningful measurements during large SEP events.

Chapter 5 summaries the RAD-HEPT design, focusing particularly on the use of scintillators as an anti-coincidence detector to directly detect and reject particles travelling outside the instrument's FOV. RADHEPT is comprised of two separate telescopes to measure the high and low energy range of particles defined by the instrument's measurement requirements. The design of the low and high energy head is presented and their response isotropic electron and proton sources.

Chapter 6 summarises the design work and analysis presented in this thesis. Each instrument has a different development timeline, as they are slated to fly on spacecrafts with a differing in scientific priorities and funding sources. The long term plans for each instrument, and the spacecrafts they are set to fly on, are detailed in Chapter 6.

Chapter 2

Theory and Background

2.1 Energetic Particle Identification

Space radiation can only be studied if it is properly measured with due regard to efficiencies in the instrument such as its noise floor and its ability to measure particle energy accurately. Energetic particles can be measured with various instruments that operate on different physical principles. The specific particle detection techniques discussed below are used in the designs for the LL-SWEPT, P-SWEPT and RADHEPT instruments.

2.1.1 Solid State Detectors

When charged particles travel through solid state detectors, they create a signal whose amplitude is proportional to the energy deposition of the particle. Silicon is a common semiconductor material used in solid state detectors as it is able to make energy measurements with impressive time, energy and spatial resolution (e.g., Lutz and Klanner, 2020). All three instruments utilize silicon detectors as their primary energy measurement technique. Every four atoms in the silicon crystal lattice share a covalent bond. When a charged particle travels through the silicon substrate the valence electrons are knocked from the valence to conduction band, breaking their covalent bond. This interaction results in a charged pair; one electron free in the conduction band and absence of an electron in the valence band called a hole. Charged particles create charged pairs as they travel through the detector's substrate. Typically, the thicker the substrate, the more charged pairs and therefore a greater signal the detector creates. Electrons and holes are able to travel within the crystal lattice, and do so when an electric field is applied to opposite sides of the detector. Electrons travel anti-parallel and holes travel parallel to the electric field, and reach the external electrode connected to the detector's readout electronics. A charge amplifier and a pulse shaping amplifier create pulses with amplitudes proportional to the energy deposited in the substrate, which become digitized by an Analog to Digital Converter (ADC) circuit and sent to a Field Programmable Gate Array (FPGA) processor for on-board data processing. As mentioned previously, the amount of charge collected at each electrode is proportional to the energy deposited in the detector and is used to determine the initial energy of the incident particle. For silicon, 3.6 eV of energy is required to create a charged pair at room temperature (e.g., Lutz and Klanner, 2020).

Different forms of ionizing radiation exhibit various energy deposition behaviour as they travel through a detector's substrate. Ions travel in a ballistic fashion through the silicon due to their relatively high momentum. Since their motion through the substrate thickness is predictable, its motion can be described analytically. The energy loss of protons, alphas, or atomic ions per unit length, the stopping power (dE/dx), is described with the Bethe-Bloch formula:

$$\frac{dE}{dx} = \frac{4\pi N_a z^2 e^4}{m_e c^2 \beta^2} B \tag{2.1}$$

$$B = \frac{Z\rho}{A}[ln(\frac{2m_e c^2 \beta^2}{I(1-\beta^2})) - \beta^2 - \frac{C}{2} - \frac{\Delta}{2}] \tag{2.2}$$

where x is the path length of the ion travelling through the stopping material (detector substrate), N_a is Avogadro's number, z is the charge of the ion, e is the elementary charge, m_e is the electron rest mass. β is $\frac{\nu}{c}$ for protons, where v is particle velocity and c is the speed of light. Z, ρ and A are the atomic number, mass density and atomic weight of the stopping material and I is the averaged exciting potential per electron in the stopping material. Δ is the is the density correction, which is only significant at high ion energies (around

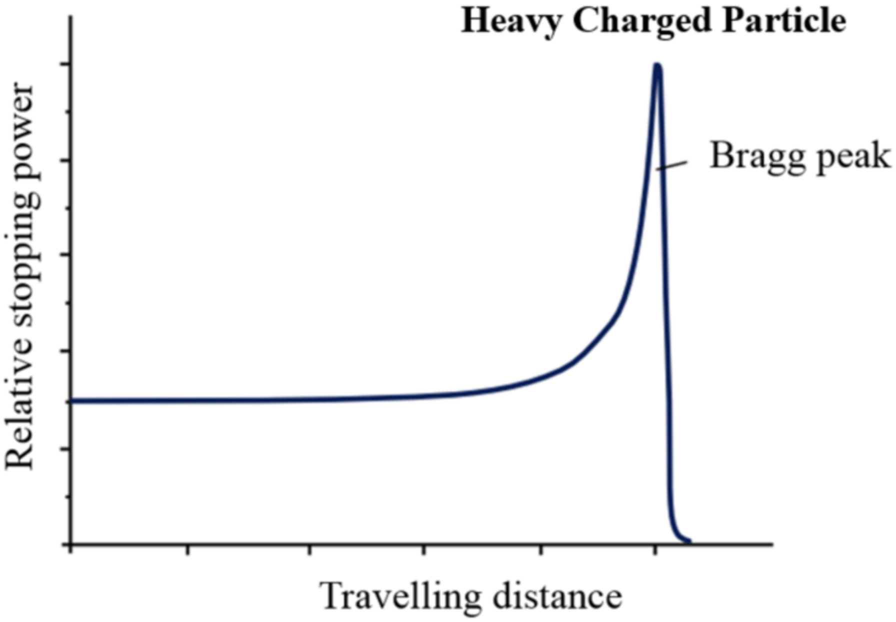

Figure 2.1: Relative stopping power of a heavy particle as a function of distance travelled through a stopping medium, showcasing the Bragg peak (taken from Grdanovska, 2015).

1 GeV for protons). The shell correction, C, is significant only for lower ion energies. Values for C and Δ can be found in Janni, 1982.

The Bethe-Bloch formula only holds if there are sufficient collisions between the incident charged particle and detector substrate to assume the particle's energy loss is continuous. This assumption is called the Continuous Slow Down Approximation (CSDA). As shown in Equation 2.1, the stopping power of different particles travelling through a given substrate is proportional to the square of their atomic numbers. For example, alpha particles will deposit four times the energy compared to single charged protons for a given path length in the same stopping material.

Figure 2.1 shows the ionization loss for a proton as a function of path length. The inverse relation between ionization loss and particle speed results in the large spike in energy deposition shown at the right of Figure 2.1, called the Bragg peak. It will be shown in the subsequent chapters that this feature is used in the identification of the energy of protons and alpha particles.

Interactions between the incident particle and the stopping material can result in angular scattering which changes the trajectory of the particle without significant kinetic energy reduction. Scattered particles which follow an angular path through a thin detector element will deposit more energy than a particle travelling straight through. Therefore, particles travelling through the detector at an angle can be misidentified as lower energy particles. Scattering can be compounded and become an issue when the particles are travelling through thick or multiple detectors. Protons and atomic ions travel in a relatively straight path through the detectors as they are more difficult to scatter. Electrons on the other hand, are consistently pushed off course as they interact with free conductance electrons of equal mass in the detector, causing significant backscattering. The collisions between incident electrons and atoms making up the substrate emit bremsstrahlung radiation (Stacy and Vestrand, 2003). The energy radiated during such a process generally escapes the thin detector element and cannot be accurately measured by the silicon detectors. While travelling through particle instrument's complex geometries, electron trajectories, and their energy deposition in the detectors is unpredictable when compared to protons. Understanding the instrument's response to electrons is best done through modelling the instrument in a particle simulation software such as Geant4, or empirical data from instrument prototypes.

The National Institute for Standards and Technology (NIST) has online databases which list the CSDA ranges and stopping power of protons, alpha particles and electrons travelling through common materials called PSTAR, ASTAR and ESTAR, respectively.

2.2 Geant4 Modeling

The Geant4 radiation-transport code is an open source software package capable of simulating the passage of particles through matter using Monte Carlo methods (e.g. Allison et al., 2016, Agostinelli et al., 2003). Geant4 is used to determine the performance of geometry trade offs for each instrument. Geant4 is capable of simulating a wide range of physical processes which results in very accurate predication of the particle behaviour. The performance of an earlier prototype of the HEPT instrument was tested inside a proton beam at the TRI-University Meson Facility (TRIUMF) and the prototype's performance was in good agreement with the results from the instrument modeled in Geant4 (Sadiq, 2012). The work completed in Geant4 in previous HEPT and SWEPT designs provide the basis for the additional simulation work completed in this thesis.

Geant4 allows users to select only the relevant physical processes to keep the simulations accurate while minimizing the required CPU resources. Geant4 provides users with reference physics lists which includes the relevant physics processes for common applications. All three instrument applications use the FTFP BERT high precision physics list, which uses the Bertini intranuclear cascade model to simulate medium energy hadron-nucleus interactions. It is a suitable physics list when the primary hadrons are below 10 GeV. It contains the standard electromagnetic physics processes appropriate for electrons and ions up to 100 TeV (Wright and Kelsey, 2015).

2.3 Geometric Factor

To determine the total particle flux of the environment in which the telescope operates, the telescope's geometry and field of view must be taken into account. A telescope's gathering power is defined as the factor of proportionality relating number of particles the instrument counts and the number of particles incident on the instrument. In the case of an isotropic incident particle source, the gathering power of the telescope is called the geometric factor (Sullivan, 1971). The geometric factor, G, is required to determine the particle source, I, from the measured counts, C,

$$C = GI \tag{2.3}$$

G is in units of cm^2sr and I in units of counts/cm^2/sr respectively, and C is simply the number of particles counted by the detector. The geometric factor is determined differently depending on the geometry of the particle telescope.

The geometric factor for a particle telescope comprised of a single sided flat open detector of area, A, is calculated simply as $A\pi$. For an ideal cylindrical symmetric telescope with two circular detectors as shown in Figure 2.2, the geometric factor is

$$G = [\frac{1}{2}\pi[R_1^2 + R_2^2 + l^2 - ((R_1^2 + R_2^2 + l^2)^2 - 4R_1^2R_2^2)^{\frac{1}{2}}] \tag{2.4}$$

For instruments with more complicated geometries, the geometric factor can only be approximated with computer simulations (Sullivan, 1971). For the instruments discussed in this thesis, the geometric factor is calculated for the first two circular detector elements using Equation 2.4 and is used as an approximation for the instrument's overall geometric factor. Geant4 simulations are used to determine the energy dependant geometric factor for each detector element, see Chapters 3, 4 and 5 for more details.

2.4 Instrument Background

This section provides a technical description of the three instruments whose development is presented in this thesis, LL-SWEPT, P-SWEPT, and RADHEPT. Previous versions of the LL-SWEPT and P-SWEPT instrument designs have been matured under multiple technology development contracts at the University of Alberta over the past 15 years. Each instrument has different layouts to better measure different particle populations at different vantage points in near Earth and interplanetary space. As mentioned, a four channel energetic particle telescope prototype was tested at TRIUMF to determine how the entire instrument performed in-situ. The performance of the prototype agreed well with the expected results from previous Geant4 modelling. Scripts used to identify particle energy were written and tested on data from the Geant4 models and the TRIUMF tests. This work provided a foundation for the development for the new designs and component selection for the instruments presented in this thesis.

LL-SWEPT and P-SWEPT's missions have previously been defined and their scientific goals finalized. RADHEPT will be flying on the RADICALS

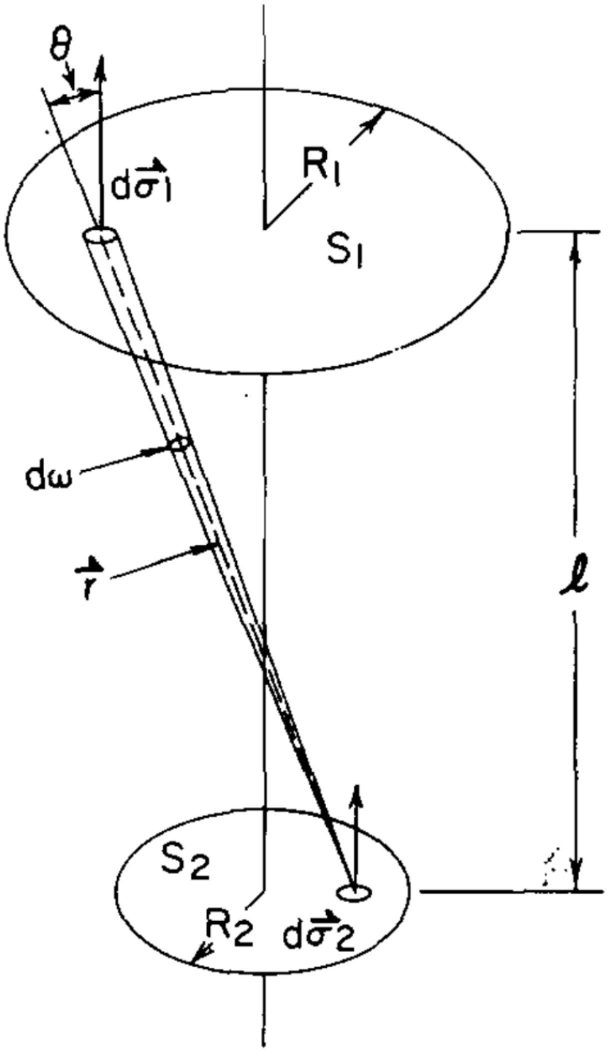

Figure 2.2: An ideal cylindrically symmetric telescope with two circular detectors, S_1 and S_2. (taken from Sullivan, 1971).

mission which is undergoing pre-phase A development at the time of this writing. All three missions have recently received funding for their continuing development as the Canadian Space Agency focuses on the space radiation risks which will be faced during deep space crewed missions slated for launch in the next decade. The following subsections provide a general overview of the three instruments, and whose design and performance will discussed in more detail in Chapters 3, 4 and 5.

2.4.1 LL-SWEPT

LL-SWEPT is a high energy proton telescope capable of measuring the direction dependant proton and alpha particle flux, designed for operation on the lunar surface. LL-SWEPT is designed to measure the energy range and count rates of particles traveling from the Sun during SEP events, GCRs travelling from outside the solar system, and albedo particles reflected from the lunar surface and from spacecraft habitats. LL-SWEPT will be able to point to all elevations over a single hemisphere with its single axis rotation gimbal mount. LL-SWEPT will use the directional pointing to attempt to measure both incident particle flux and albedo flux from the lunar surface. LL-SWEPT will be able to resolve the spatial changes in SEP flux during the early phases of an evolving SEP event while the flux is believed to be anisotropic. Its data would be used to better understand and predict the radiation risks faced by future astronauts and their electronic hardware. It has also been shown that the energy range and direction of albedo particles could provide evidence for the presence of water on the lunar surface, and LL-SWEPT is capable of directly measuring the albedo particles to investigate such claims (e.g., Schwadron et al., 2016). The incoming SEP flux is expected to be highly directional and evolving in time through the course of a SEP event. Therefore, the measurement of the lunar albedo proton spectrum due to primary GCR and SEP flux will require steering the telescope at different angles from the lunar surface. Figure 2.3 shows a schematic of LL-SWEPT during its mission.

To capture the scientifically useful range of GCR and SEP flux, LL-SWEPT shall measure protons from 30 to 300 MeV and alpha particles from 100 to

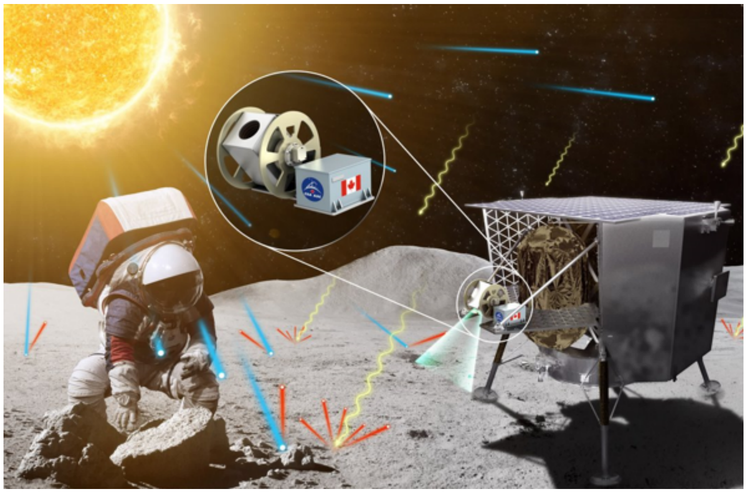

Figure 2.3: LL-SWEPT render integrated on the lunar lander during its mission.

900 MeV. An energy identification resolution of Δ E/E <0.5 is sufficient to capture the expected GCR and SEP flux spectrum for LL-SWEPT. Ideally the energy resolution shall be Δ E/E <0.4 to account for any unexpected sharp changes in the energy dependant flux. Figure 2.4 shows the integral proton flux estimated for solar max (peak solar proton flux) and the difference in flux between the two primary particle sources modelled by the Solar Accumulated and Peak Proton and Heavy Ion Radiation Environment (SAPPHIRE) model. The SAPPHIRE model is based on data from the European Space Agency's (ESA) Solar Energetic Particle Environment Modelling (SEPEM) reference data set version 2.1 and is available on the SEPEM application server. More information on the SAPPHIRE model can be found in Jiggens et al., 2018. The expected count rate range is used to optimize the geometric factor and define the required shielding to keep the dead time fractions at an appropriate level. The details of the analysis are written in Chapter 3. Figure 2.5 shows the expected integral flux of protons and alpha particles during solar maximum and minimum, from the ISO-15390 model (data source: https://www.iso.org/standard/37095.html).

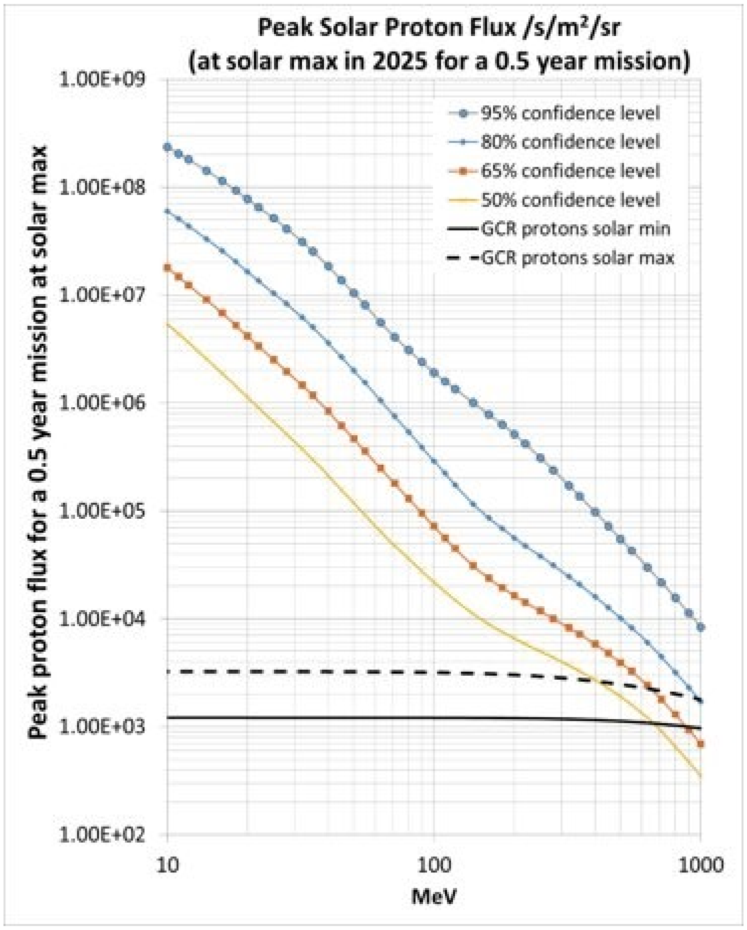

Figure 2.4: The integrated SEP flux levels above a given energy are plotted verses energy derived using the SAPPHIRE model. The confidence levels indicate the likelihood that the flux will not be exceeded during a 0.5 year mission. Plot courtesy of Louis Ozeke.

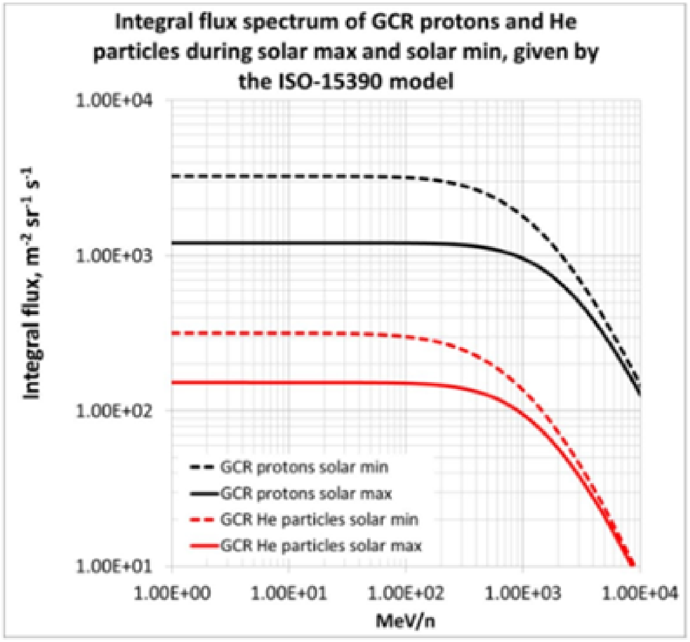

Figure 2.5: The integrated proton and alpha particle flux populations in GCR flux during solar maximum and minimum.

2.4.2 P-SWEPT

Like LL-SWEPT, P-SWEPT is a high energy particle telescope designed to measure particles from GCRs and SEPs events in interplanetary space outside the earth's magnetosphere to better understand the processes behind both particle fluxes and the risks they pose to astronauts. P-SWEPT is designed to use on the LOP-G or a similar platform. LOP-G is a planned space station which will serve as a transfer station for crewed missions to the moon and as a laboratory for deep space research. P-SWEPT shall measure protons from 20 to 300 MeV, a suitable range to properly measure GCR and SEP flux. P-SWEPT will be mounted on a dual axis rotating platform to make angular resolved measurements. Figure 2.6 shows a CAD model of the P-SWEPT instrument on its gimbal mount. P-SWEPT will be have a mission lifetime of 4 to 5 years, so there is a larger chance the instrument will witness a large SEP event. The geometric factor is optimized to allow P-SWEPT to fully resolve the expected flux for a one in twenty year SEP event. Figure 2.9 shows the differential flux for a large one in twenty year (95th percentile) SEP event.

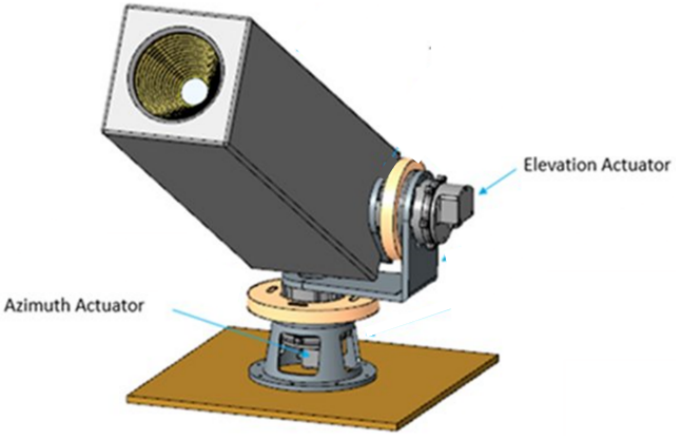

Figure 2.6: CAD model of P-SWEPT and its dual axis gimbal mount.

As mentioned, SEP events can have very unpredictable onsets which presents a threat to astronauts unprotected by the Earth's magnetic field. It has been shown that relativistic electrons accelerated from the Sun during magnetically connected SEP events can reach the Earth up to an hour before the proton flux (Posner, 2007, Núñez, 2015). The intensity and timing of electron flux can give an advance warning of the strength and rise time of the upcoming SEP event. The early onset electron flux can be used as an early warning system to predict the arrival of the dangerous proton and heavy ion flux, providing valuable time for crewed missions to implement safety measures, or set up experiments. While P-SWEPT was initially designed to measure protons, an additional coincidence detector at the instrument's aperture can be added to detect the earlier electron flux. This design augmentation is described in detail in Section 4.2.

The COmprehensive Suprathermal and Energetic Particle analyzer (COSTEP) particle flux observations from 1995 to 2005 show that all SEP events containing significant fluences of greater than 30 MeV/n ions are accompanied by enhancements in relativistic electrons (Posner, 2007). Electron detection instruments on board the SOlar and Heliospheric Observatory (SOHO), and the Mars Atmosphere and Volatile EvolutioN (MAVEN) orbiter have measured the electron flux preceding a SEP event. Figure 2.7 shows electron flux data from the MAVEN spacecraft and Figure 2.8 shows electron and proton flux over various SEP events from SOHO. Particle flux data from both spacecraft shows the rate of increase in electron flux is much steeper than the proton flux. Figures 2.7 and 2.8 also show that lower energy electrons reach the instrument first and can provide the longest range forecast for proton flux in SEP events and have the largest relative flux. Generally, particles of lower energy are easier to detect with higher efficiency with silicon detectors as they require less silicon length to deposit all their energy into a detector, negating the need for additional detectors and degraders, which increases particle scattering. From the SOHO and MAVEN electron flux data, it is clear an electron energy detection range of 0.05 to 2 MeV would provide data useful enough to properly identify electron flux that precedes proton and ion flux during a SEP event.

2.4.3 RADHEPT

The RADICALS High Energy Particle Telescope (RADHEPT) is one of the four payloads slated to fly on the upcoming RADICALS mission. The RADICALS is a Canadian microsatellite mission designed to measure the energetic particle environment in LEO to better understand the physical processes driving charged particle precipitation from the Van Allen Belts into Earth's atmosphere. An artist's rendition of the RADICALS mission is shown in Figure 2.10. Energetic particle precipitation has become a topic of high scientific priority as it is believed to have a potential impact on long term climate change patterns and to disrupt HF communications on Earth. Like LL-SWEPT and P-SWEPT, the telescopic RADHEPT instrument will be able to make angular resolved measurements since its field of view will rotate as the RADICALS spacecraft will be spinning with a period of approximately 30 seconds. Two identical RADHEPT instruments will be mounted on the RADICALS spacecraft, pointed in opposite directions, see RADHEPT #1 and #2 in Figure 2.10. In this configuration, the spacecraft will be able to take particle flux measurements inside and outside the loss cone at the same position once every half spin. This will result in pitch angle resolved energetic particle data, filling a gap in the capabilities of existing missions being designed to resolve

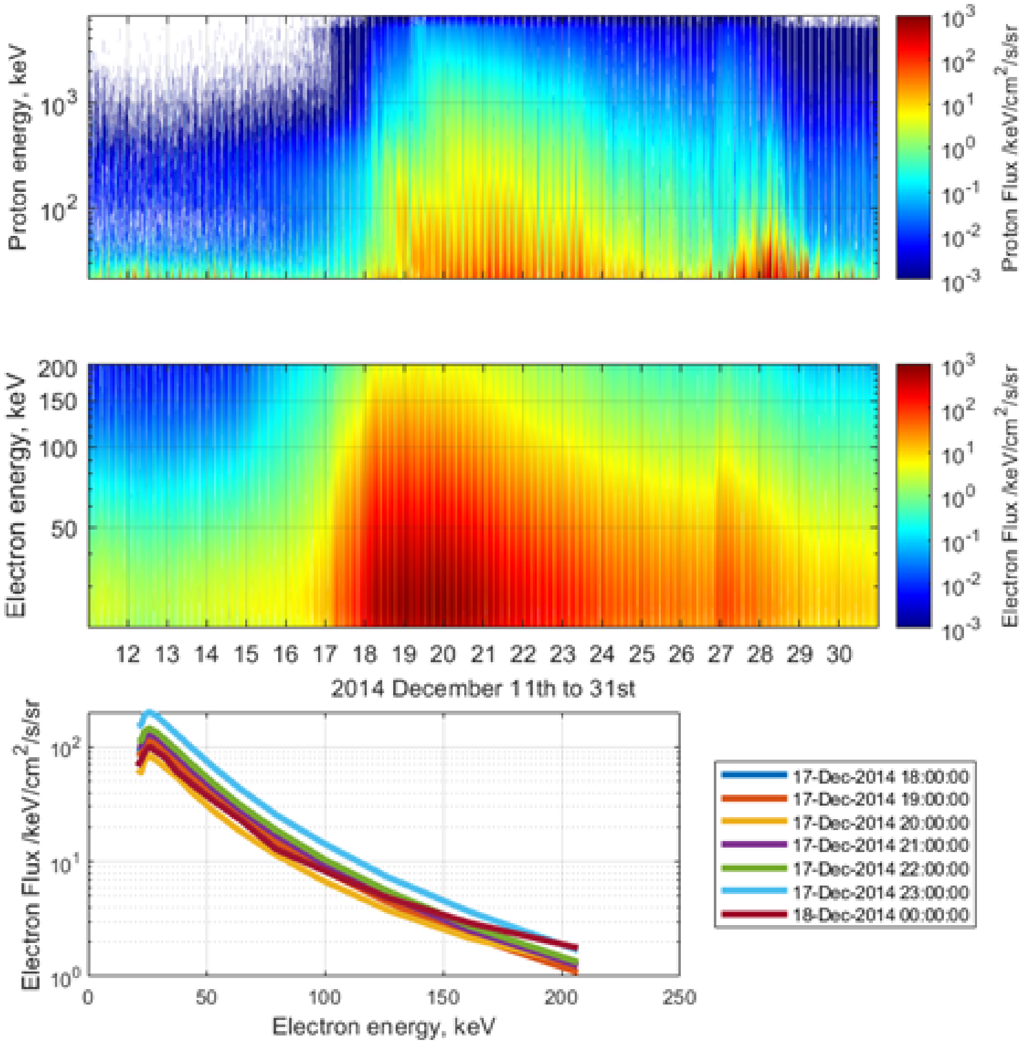

Figure 2.7: Top panel: Proton differential flux data during a SEP event from December 11th to 31st, 2014. Middle panel: Electron differential flux data during a SEP event from December 11th to 31st, 2014. Bottom panel: Electron differential flux against electron energy for select times in the initial rise time of electron flux during the SEP event. Data from the front detector (F1) on the MAVEN spacecraft. Data source: https://pds-ppi.igpp.ucla.edu/search/view/?f=yesid=pds://PPI/maven.sep.calibrated /data/spec/2014/12. Plot courtesy of Louis Ozeke, University of Alberta.

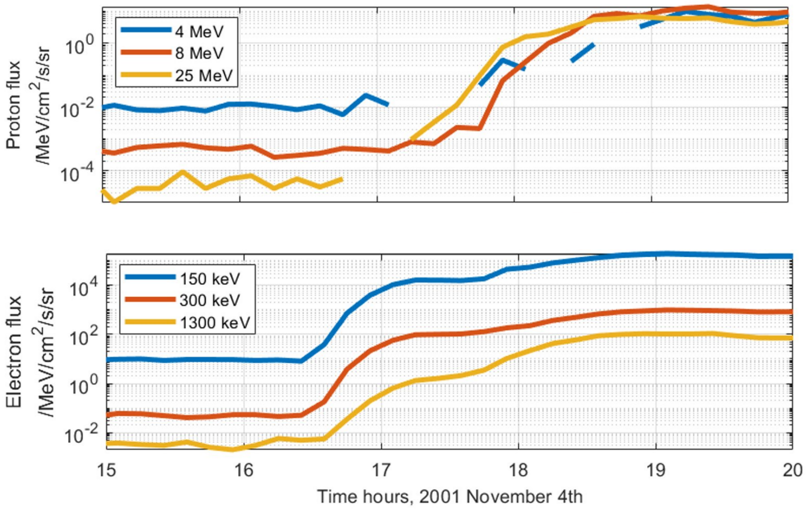

Figure 2.8: Top panel: Differential proton flux during a SEP event in November, 2001. Bottom panel: Differential electron flux during a SEP event in November, 2001. Data take from the Electron, Proton and Helium Instrument on the SOHO Spacecraft. Data source: http://www2.physik.uni-kiel.de/SOHO/phpeph/EPHIN.htm. Plot courtesy of Louis Ozeke.

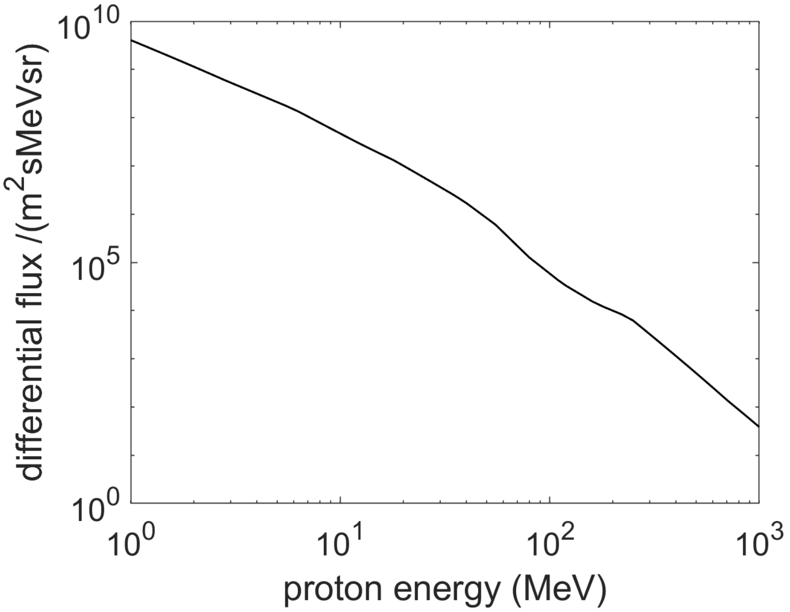

Figure 2.9: Differential SEP proton flux during a one in twenty year (95 % percentile during a one year mission) from the SAPPHIRE model, linearly interpolated for data points with energies from 1 through 1000 MeV with a 1 MeV step size.

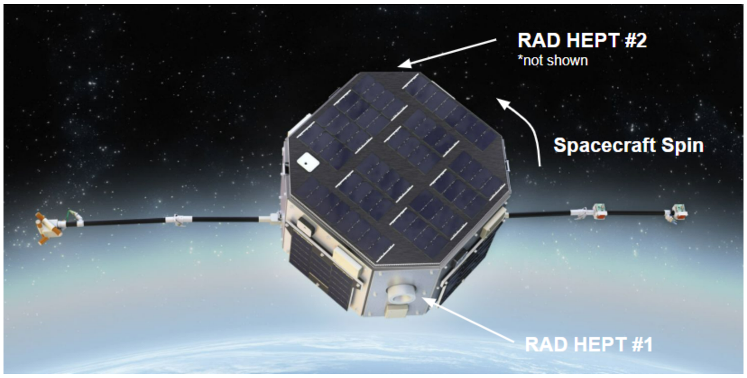

Figure 2.10: Artist rendition of the proposed RADICALS satellite. Photo credit: Andy Kale.

the angular distributions of both trapped and precipitating electrons in the Van Allen Belts. The fully pitch angle resolved electron flux data will be used to determine the spatial distribution of particle precipitation to better understand the processes that drive it. At the poles, the high energy proton data will quantify the flux, energy spectrum and spatio-temporal extent of strong and weak energetic proton precipitation from SEP events into the polar cap. At low latitudes, measurements of inner zone protons in the radiation belt will be used to better understand the drivers behind energetic proton precipitation. Collectively, this will in aid in the development of improved models and forecasts for HF radio communication interruptions arising from the precipitation of energetic protons.

To make comprehensive particle measurements, RADHEPT is required to measure protons with energies from 1 to 20 MeV and electrons with energies from 0.1 to 3 MeV. RADHEPT is broken up into two energy heads, RADHEPT-LE (low energy) and -HE (high energy) to be able to measure the large range of expected counts over RADHEPT's required energy range. RADHEPT-LE targets the lower energy proton (1 to 8 MeV) and electron (0.1 to 1 MeV) range. RADHEPT-HE covers the upper energy range, up to 3 MeV electrons and 20 MeV protons.

Figure 2.11 shows electron and proton integral flux data from the Polar Orbiting Environment Satellite (POES) 14 from 1998 to 2010 for L-shells from 3 to 6. Figure 2.11 provides an estimate of the approximate electron and proton populations that RADHEPT will measure. The POES satellites have two particle detectors oriented perpendicular to each other, to measure the particle population from the zenith and anti-ram (opposite to the direction of travel) directions. The zenith (0 degree) facing detector usually (at higher L-shells) measures particle populations inside the loss cone, and the backwards facing detector typically measures trapped particles in the core of the radiation belts. The particle detector suite on the POES satellites is called the Medium Energy Proton and Electron Detector (MEPED) (Yando et al., 2011). Figure 2.12 shows the electron flux from the 0 and 90 degree detector as a function of L-shell from MEPED, along with the pitch angle measurements as a function of L-shell from both detectors.

The plot in the fifth row, second column, of Figure 2.11 shows that MEPED on POES-14 rarely measures > 6900 keV protons with a count rate exceeding 1000 counts/sec. The plot in the third row, first column, of Figure 2.11 shows that MEPED on POES-14 rarely measures > 300 keV electrons with a count rate exceeding 10,000 counts/sec. Therefore, the maximum approximate MEPED count rate is 11,000 counts/sec for protons > 6900 keV and electrons > 300 keV, which is the approximate energy range RADHEPT-HE is designed to measure. MEPED has a geometric factor of 0.01 cm^2sr, so the reasonable maximum isotropic flux RADHEPT HE is expected to measure in is 1.1×10^6 counts/s/cm^2/sr. POES has an altitude of 872 km so the maximum count rates at RADICAL's altitude, ≈ 600 km, will typically be very slightly less as Earth's magnetic field will reflect some of the particles travelling from the outer magnetosphere.

Precipitating electrons (electrons inside the loss cone, measured by the 0 degree detector) have a lower count rate than trapped electrons at the L-shell range over $\mathrm{L} = 3$ to 6 and for all integral energy channels measured by MEPED on POES. High energy proton flux will only be measured during polar cap absorption events or in the inner radiation belt where high particle counts are expected. Therefore, the RADHEPT-HE's minimum count rate is derived from the 1st percentile expected electron population >300 keV inside the loss cone, estimated to be 10 counts/s/cm^2/sr, see the second row, third column

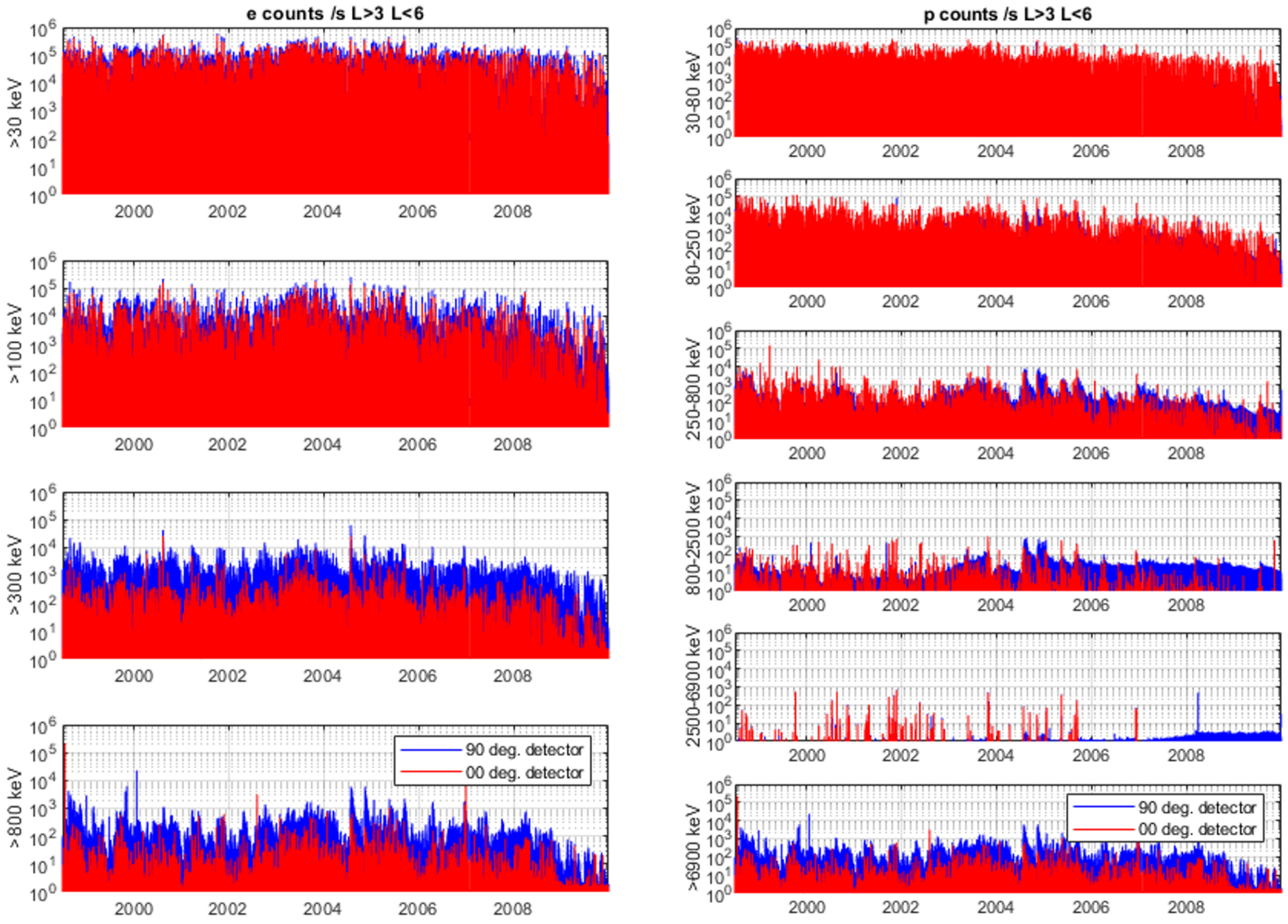

Figure 2.11: Electron and proton count rates from 1998 to 2010, between L-shells 3 to 6, spanning the outer radiation belt from the MEPED detector on the POES 14 spacecraft. Left column: Integral electron count rate with integral channels >30 keV, >100 keV, >300 keV, and >800 keV collected by MEPED's 90 and 0 degree detector, see text for details. Right column: Differential proton count rate channels 30-80 keV, 80-250 keV, 250-800 keV, 800-2500 keV, 2500-6900 keV, and integral channel >6900 keV collected by MEPED's 90 and 0 degree detector, see text for details. Data source: https://www.ngdc.noaa.gov/stp/satellite/poes/dataaccess.html. Plot courtesy of Louis Ozeke, University of Alberta.

plot (>300 keV electron flux, 0 degree detector) in Figure 2.12.

As mentioned, RADHEPT-LE will measure electrons with energies from 0.1 to 0.3 MeV and protons from 1 to 8 MeV. The plot in the second row, first column of Figure 2.11 shows that >100 keV electron flux rarely exceeds 1×10^5 counts/sec from MEPED, or 1×10^7 counts/s/cm^2/sr. The plot in the third row, first column of Figure 2.11 shows that electron flux above RADHEPT-LE's upper measurement limit, 300 keV, rarely exceeds 1×10^4 counts/sec from MEPED, or 1×10^6 counts/s/cm^2/sr. >300 keV electron flux is therefore a small contribution to the >100 keV electron flux, and it is not subtracted from the estimated maximum electron flux for RADHEPT-LE. The second column in Figure 2.11 shows that MEPED's proton channels which fall within RADHEPT-LE's proton energy range (800 to 2500 keV, 2500 to 6900 keV, and >6900 keV) have very low count rates when compared to the electron flux RADHEPT-LE will measure. Additionally, a majority of the protons counted into the >6900 keV integral channel are likely to be higher than RADHEPT-LE's upper proton energy limit, 8 MeV. Therefore, the maximum estimated count rate RADHEPT-LE is required to measure is based on the 99th percentile electron flux >100 keV measured by MEPED, approximately 1×10^7 counts/s/cm^2/sr. Similarly to RADHEPT-HE, the minimum count rate for RADHEPT-LE is defined by the minimum electron flux measured by the MEPED detector within RADHEPT-LE's energy range, shown in the left hand plots in Figure 2.12. The minimum (1st percentile) flux (excluding at very low L-shells) for >100 keV electrons is between 10 to 20 counts/s/cm^2/sr, as seen in column two, row two, of the left hand plots in Figure 2.12. As column three, row two shows, the minimum (1st percentile) flux for electrons >300 keV is below 10 counts/seconds. Therefore, an approximate minimum estimated count rate for electrons between 100 and 300 keV, RADHEPT-LE's approximate energy range, is 10 counts/s/cm^2/sr.

RADHEPT-HE measures particles travelling through the entrance cone with a stack of seven silicon detectors. Instead of shielding the particle identification elements with a very large amount of high-Z outer shielding, an anti coincidence scintillator is proposed to discriminate against the particles trav-

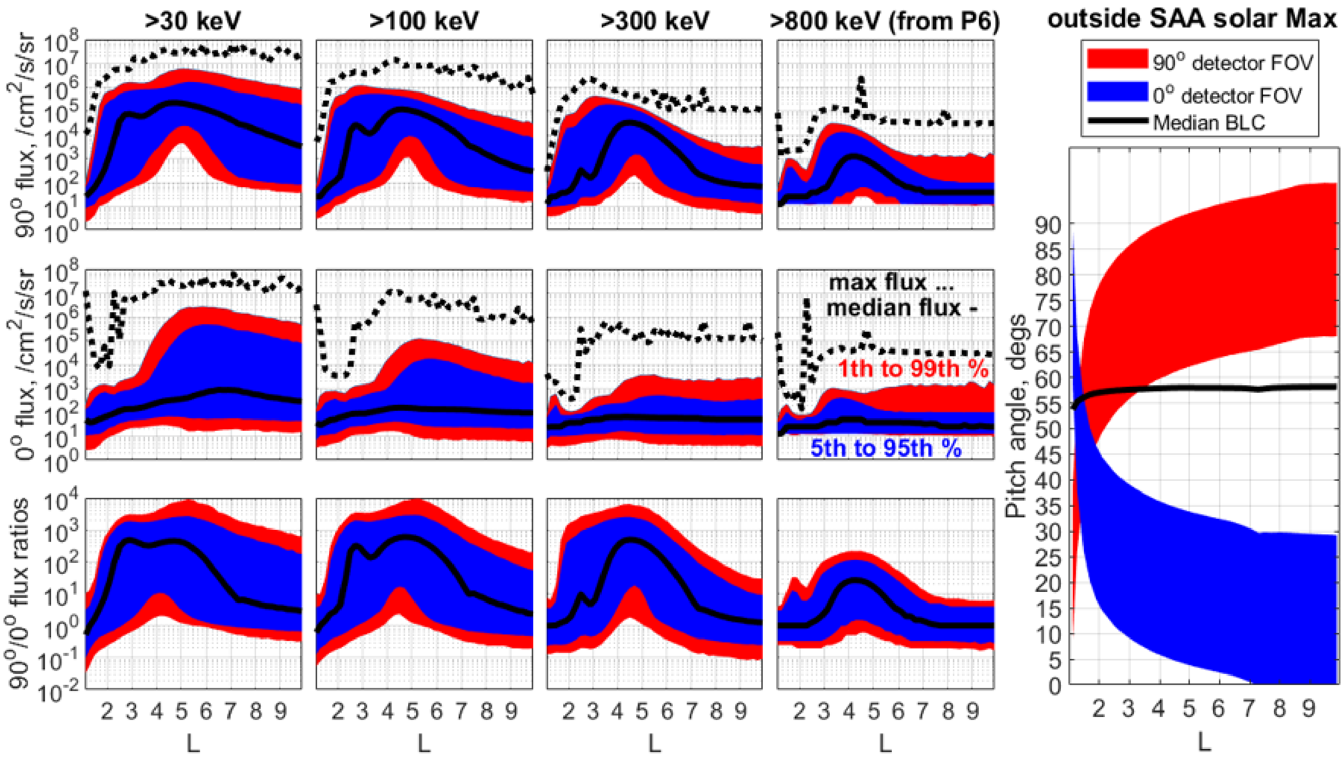

Figure 2.12: POES-14 electron integral flux rate statistics outside the South Atlantic Anomaly during solar maximum from the MEPED detector. Left plots, first column: 95th percentile (blue), 99th percentile (red), and maximum (black dotted) electron integral flux >30 keV from the 90 degree detector as a function of L-shell (first row), from the 0 degree detector as a function of L-shell (second row), and the ratio between >30 keV electron flux in the 90 and 0 degree detector as a function of L-shell. Identical rows in columns 2, 3 and 4 for >100 keV, >300 keV and >800 keV electron integral channels. Right plot: Pitch angle measurements from the 90 degree (red) and 0 degree (blue) detector as a function of L-shell. The black curve shows the median bounce loss cone as a function of L-shell. Data source: https://www.ngdc.noaa.gov/stp/satellite/poes/dataaccess.html. Plot courtesy of Louis Ozeke, University of Alberta.

eling through the detector sides, outside its field of view from the valid counts which enter through the aperture. RADHEPT-LE is comprised of three silicon detectors capable of measuring the lower energy electrons and protons, mounted behind an entrance cone to restrict the field of view of the detector. The detailed design and performance of RADHEPT-HE and RADHEPT-LE are detailed in Chapter 5.

Chapter 3

LL-SWEPT

Chapter 3 presents the design and simulation work completed on the LL-SWEPT instrument. A previous version of the SWEPT instrument provides the basis for this work, including a Geant4 model and low energy particle identification algorithm. LL-SWEPT's geometry is optimized to detect GCR and SEP events from the lunar surface, and the shielding around its silicon detectors is designed to protect against off-axis particles, ensuring acceptable dead time losses during the expected proton and alpha particle flux LL-SWEPT will experience during its 14 day mission lifetime on the moon. A separate proposed regime for identifying high energy protons is presented. The analysis behind these design decisions and data processing regimes are shown in the subsequent sections. Geant4 modelling done for previous SWEPT contracts provides the basis for this work.

3.1 LL-SWEPT Instrument Introduction

LL-SWEPT measures the energy of particles as they slow down and deposit energy in a stack of nine silicon detectors. See Section 2.1.1 for details on energetic particle detection with silicon detectors. Detector D0 is positioned behind the entrance cone and is separated from the rest of the detector stack, see Figure 3.1 for positions of the silicon detectors D0 to D8 within the instrument. LL-SWEPT has a full angle FOV of 20 ° and targets a geometric factor of 1.3 cm^2sr. The nominal geometric factor of the instrument is initially defined by the radius and spacing of the detectors D0 and D1 using Equation 2.4, and the energy-dependant geometric factor of the instrument is be found empirically with simulated performance data from the instrument (e.g Sullivan, 1971). Energy deposition in D0 and D1 provide a coincidence condition to discriminate between particles travelling inside and outside LL-SWEPT's FOV. In the space between detector D0 and the rest of the detector stack, copper baffles prevent scattered and off-axis particles from reaching the back detector stack. Protons with energies >20 MeV have enough energy to travel to D1, which defines the lower proton measurement limit LL-SWEPT can accurately measure. The radius of the detector stack increases with detector number to maximise the detection of particles travelling through the aperture and along the inside of the entrance cone. The larger detectors will also compensate for particles which scatter off their original trajectory as they travel through the stack.

LL-SWEPT's silicon detectors are surrounded by 2.35 mm of aluminum support wall and a 2 mm aluminum outer package that encloses the entire instrument. Behind the detector stack, a 3.8 mm copper back shield protects against particles entering directly through the backside of the instrument. The side shielding protects up to 30 MeV protons and the back shielding protects up to 60 MeV protons. Aluminum, copper and tungsten degraders in between the detectors increase the energy range of protons which come to rest in the detectors, which is a simple method to increase the energy measurement range of the instrument while minimizing the required number of detectors and preamplifer electronics.

Representative electronics are mounted to the back of the instrument. The material, surface area and height of the electronics is based on previous SWEPT studies and is scaled to the number of detectors in the stack. The average elemental composition of the electronics package is shown in Table 3.1 and is based on common materials and relative composition found in printed circuit boards (e.g., Gerbase and Oliveira, Camila Reis de, 2012).

This design is referred to as LL-SWEPT baseline geometry throughout this text, a schematic of the baseline geometry is shown in Figure 3.1. LL-SWEPT's baseline geometry has an approximate mass of 4.5 kg and with the

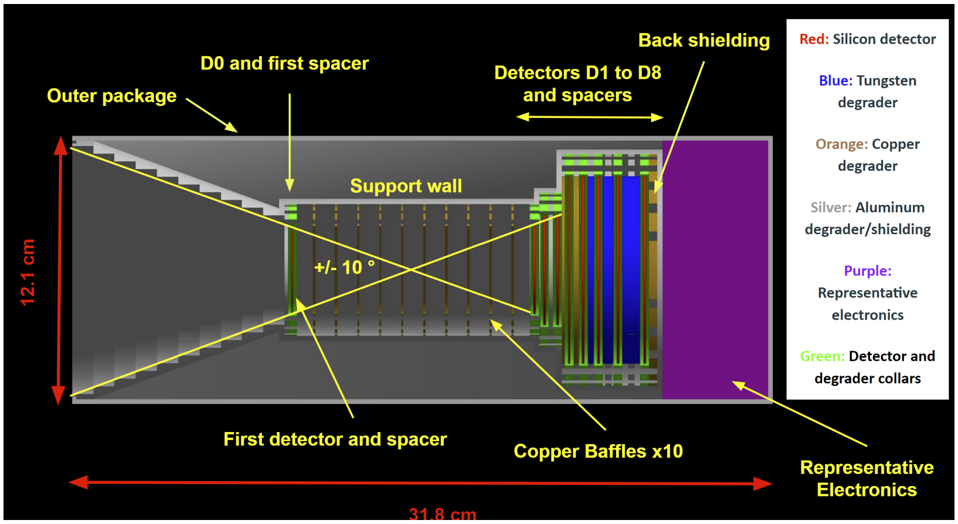

Figure 3.1: An annotated cross-section of LL-SWEPT baseline geometry in Geant4.

dimensions of 12.1 cm by 12.1 cm by 31.8 cm. Figure 3.1 is a cross-sectional view of the LL-SWEPT baseline geometry modelled in Geant4. Tables 3.2 and 3.3 show the size and mass breakdown of the LL-SWEPT baseline geometry. Table 3.4 gives the thickness of the silicon detectors as well as degrader materials and thickness in front of each detector.

3.2 Energy Deposition and Particle Identification

This section provides an overview of LL-SWEPT's response to proton and alpha particles travelling directly through its FOV.

3.2.1 LL-SWEPT Proton Response

As mentioned in Section 2.2, Geant4 proton and alpha particle simulations are used to determine the response of the LL-SWEPT instrument. Figure 3.2 shows the average energy deposition as a function of proton energy in each of LL-SWEPT's detectors. The data in this plot is from a Geant4 simulation shooting a pencil beam of 1000 protons at energies from 15 to 450 MeV at 1 MeV steps directly through the centre of LL-SWEPT's FOV. The along axis simulation results in the best case expected performance of the instrument,

Table 3.1: Elemental % composition of representative electronic material used in the LL-SWEPT instrument.

Material	% Composition
Copper	14%
Iron	6%
Nickel	2%
Zinc	2%
Tin	2%
Lead	2%
Bakelite Plastic	19%
Boron	4%
Aluminum Oxide	14%
Pyrex *represent glass and ceramic	35%
Total	100%

Table 3.2: LL-SWEPT baseline geometry dimensions.

LL-SWEPT Subsystem Geometry		
Parameter	Value	Unit
Number of Detectors	9	
Geometric Factor	1.3	cm^2sr
FOV (full angle)	20	°
Support Wall Thickness	2.35	mm
Back Shielding Thickness	3.84	mm
Package Thickness	2	mm
Detector Collar Thickness	4	mm
Degrader Collar Thickness	3	mm
LL-SWEPT Overall Dimensions		
Width	12.1	cm
Length	31.8	cm

Table 3.3: LL-SWEPT baseline geometry mass breakdown.

Mass	Value (kg)	% of Total Mass
Total Mass	4.52	
Collar Degrader Mass	0.12	2.7%
Collar Detector Mass	0.10	2.2%
Degrader Mass	1.75	38.7%
Detector Mass	0.08	1.8%
Backplate Mass	0.30	6.6%
Baffle Ring Mass	0.14	3.1%
Entrance Cone Mass	0.28	6.2%
Wall Mass	0.35	7.7%
Package Mass	0.91	20.1%
PCB Mass	0.49	10.8%

Table 3.4: LL-SWEPT silicon detector thicknesses and degrader material and thicknesses.

Detector	Silicon Detector thicknesses		Degrader thicknesses		
0	0.05	cm	Aluminum	0.15	cm
1	0.1	cm	Aluminum	0.01	cm
2	0.1	cm	Aluminum	0.05	cm
3	0.1	cm	Aluminum	0.18	cm
4	0.1	cm	Copper	0.13	cm
5	0.1	cm	Copper	0.24	cm
6	0.1	cm	Tungsten	0.29	cm
7	0.1	cm	Tungsten	0.48	cm
8	0.1	cm	Tungsten	0.82	cm

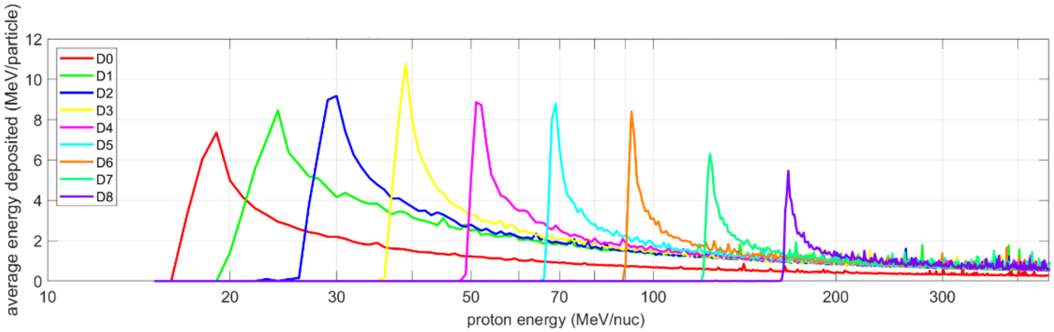

Figure 3.2: Average energy deposition as a function of proton energy for each detector element in the LL-SWEPT baseline geometry for a proton beam travelling on-axis through LL-SWEPT's aperture in Geant4.

as it only models particles travelling in one direction. Particles traveling at angles inside and outside LL-SWEPT's FOV are therefore not represented. As mentioned in Section 2.1, as ions slow down in material they deposit a disproportionately large burst of energy just before they come to rest, known as the Bragg Peak. The thickness of the degraders sandwiched between each detector are sized such that Bragg Peaks which occur in two subsequent detectors do not overlap in proton energy. The sharp increase in energy deposition in a single detector provides a simple and robust method to measure particles whose energies are low enough to stop in the detector stack. The distinct Bragg peak energy deposition values are incorporated into the binning thresholds for the energy channels. As the proton energy increases, it becomes less likely that the proton will come to rest in the stack. Particles which do not come to rest in the stack do not deposit a large amount of energy in any of the detectors and therefore cannot be immediately identified with the aforementioned method. A proposed method to identify higher energy protons that do not come to rest in the detector stack is detailed in Section 3.5.

Protons which satisfy the coincidence condition are sorted into logarithmic spaced energy channels defined in Table 3.5. The energy a proton deposits within each detector must fall within an assigned energy deposition range to be sorted into a given energy channel. As Table 3.5 shows, the lowest energy deposition required to fall within any energy deposition range is 0.1 MeV.

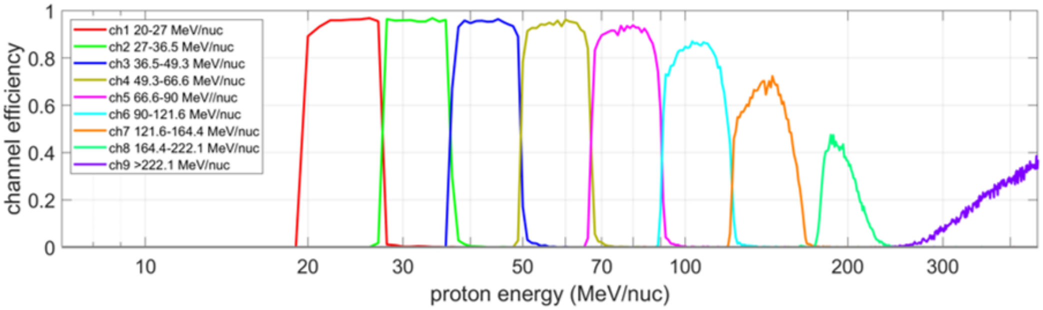

Figure 3.3: LL-SWEPT channel efficiency as a function of proton energy for a proton beam travelling on-axis through LL-SWEPT's entrance aperture in Geant4.

It is expected that noise floor of the detectors will be around 0.1 MeV, so any energy deposition below this threshold may be indistinguishable from the noise. The 0.1 MeV noise floor is chosen due to the detector noise response of $\sim$ 30 keV and allowing for additional noise from the digitization of the signals and detector degradation over the lifetime of the mission. Protons from the on-axis Geant4 simulation are sorted into energy channels and the channel efficiency as a function of proton energy for the LL-SWEPT baseline geometry is plotted in Figure 3.3.

3.2.2 LL-SWEPT Alpha Particle Response

As mentioned in Section 1.2.1, a typical SEP event and background GCR flux can have a significant alpha particle population. Heavier particles deposit more energy per unit length than lighter ones for a given energy, therefore are more damaging to humans (e.g., Chancellor et al., 2018). Special consideration toward detecting alpha particles are required given the overall biological risks of SEPs and GCRs.

A Geant4 simulation study to determine LL-SWEPT's response to alpha particles is performed. A pencil beam travelling on-axis through the LL-SWEPT's aperture of 1000 alpha particles between the energy range 60 to 1000 MeV with a step size of 1 MeV is simulated in Geant4. As shown with the Bethe-Bloch equation (Equation 2.2), the stopping power for an ion is dependant on the square of its charge. As a result, it is expected that al-

Table 3.5: Energy deposition decision thresholds in MeV deposited for detectors D0 through D8 for LL-SWEPT proton bins.

Channel 1: 20-27 MeV/nuc									
LL-SWEPT Detector number	D0	D1	D2	D3	D4	D5	D6	D7	D8
Max Energy Deposition	5.00	12.65	6.00	0.10	0.10	0.10	0.10	0.10	0.10
Min Energy Deposition	2.10	4.00	0	0	0	0	0	0	0
Channel 2: 27-36.5 MeV/nuc									
Max Energy Deposition	2.78	6.92	12.65	4.41	0.10	0.10	0.10	0.10	0.10
Min Energy Deposition	1.46	3.17	3.89	0	0	0	0	0	0
Channel 3: 36.5-49.3 MeV/nuc									
Max Energy Deposition	1.93	4.19	5.14	12.65	3.52	0.10	0.10	0.10	0.10
Min Energy Deposition	1.01	2.26	2.46	3.08	0	0	0	0	0
Channel 4: 49.3-66.6 MeV/nuc									
Max Energy Deposition	1.44	2.99	3.25	4.07	12.65	2.79	0.10	0.10	0.10
Min Energy Deposition	0.83	1.70	1.77	1.94	2.41	0	0	0	0
Channel 5: 66.6-90 MeV/nuc									
Max Energy Deposition	1.10	2.25	2.34	2.56	3.19	12.65	2.20	0.10	0.10
Min Energy Deposition	0.65	1.323	1.35	1.41	1.54	1.91	0	0	0
Channel 6: 90-121.6 MeV/nuc									
Max Energy Deposition	0.865	1.75	1.79	1.87	2.04	2.52	12.65	1.76	0.10
Min Energy Deposition	0.52	1.05	1.06	1.09	1.14	1.24	1.53	0	0
Channel 7: 121.6-164.4 MeV/nuc									
Max Energy Deposition	0.69	1.39	1.40	1.44	1.50	1.64	2.02	12.65	1.41
Min Energy Deposition	0.42	0.844	0.85	0.86	0.88	0.92	1.00	1.23	0
Channel 8: 164.4-222.1 MeV/nuc									
Max Energy Deposition	0.56	1.12	1.12	1.14	1.17	1.21	1.32	1.62	12.65
Min Energy Deposition	0.35	0.69	0.70	0.70	0.71	0.72	0.76	0.82	0.99
Channel 9: >222.1 MeV/nuc									
Max Energy Deposition	0.46	0.92	0.92	0.93	0.94	0.96	1.00	1.08	1.31
Min Energy Deposition	0.29	0.58	0.58	0.58	0.59	0.59	0.61	0.63	0.68

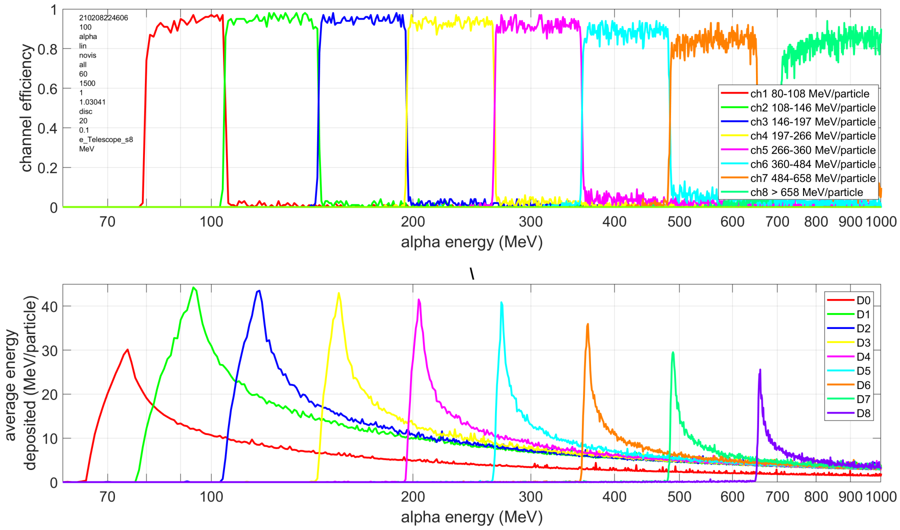

Figure 3.4: Top panel: Channel efficiency as a function of alpha particle energy for an alpha particle beam travelling on-axis through LL-SWEPT's aperture in Geant4. Bottom panel: Average energy deposition as a function for an alpha particle beam travelling through the centre of LL-SWEPT's entrance aperture.

pha particles (He ++) will deposit four times the energy when compared to a single charged proton per unit length travelled. Therefore, a separate set of logic tables is required to efficiently bin the alpha particles. In theory, the channel thresholds in Table 3.5 should simply be multiplied by a factor of four to accurately bin alpha particles. This is done to create preliminary binning thresholds for alpha particles and can be updated if further optimization is required. The average energy deposition and channel efficiency as a function of alpha particle energy for the LL-SWEPT baseline geometry is shown in Figure 3.4.

As expected, the alpha particle energy deposition in each detector is four times larger than for protons. The much larger alpha particle energy deposition is a distinguishing factor which can be used to sort proton and alpha particle events, prior to sorting them into their respective energy channels. When compared to protons, the alpha particle count rate efficiency is approximately five percent larger. Along with the larger energy deposition signals, alpha particles undergo less scattering as they travel through matter due to their relatively high mass when compared to protons. This preliminary alpha particle study concludes that incoming alpha particles with energies 80 to 660 MeV will be accurately counted with the current energy binning technique described above, sufficiently covering the energy range required to resolve the GCR alpha particle flux, see Figure 2.5 for the expected GCR flux spectra during solar minimum. No additional modifications to the LL-SWEPT design or changes to the energy identification algorithm are required to detect alpha particles within the energy range required to monitor SEP and GCR flux with the LL-SWEPT.

3.3 Off-axis and Isotropic Source Geant4 Simulations

The data used to plot the average energy deposition and binning efficiency plots described in Section 3.2.1 is from Geant4 simulations shooting a pencil beam directly through the centre of the instrument's FOV along the long axis of LL-SWEPT. The on-axis simulations provide insight into the instrument's best case performance, as off-axis particles travelling inside and outside the FOV or which scatter within the telescope are not accounted for. Off-axis particles travelling through the FOV will travel through more detector material and therefore deposit more energy in each detector before stopping than particles travelling on-axis. Most particles travelling through the instrument outside the FOV won't satisfy the coincidence condition and will be rejected with the binning logic; nevertheless such particles will increase the dead time of the instrument. This section details the simulation set-up and detector performance in the case of protons travelling off-axis inside and outside the FOV of LL-SWEPT's baseline design.

3.3.1 Angled Proton Source, travelling through LL-SWEPT's FOV

Angled particles travelling through LL-SWEPT's FOV may be misidentified as a particle of lower energy. A Geant4 simulation is performed to determine the

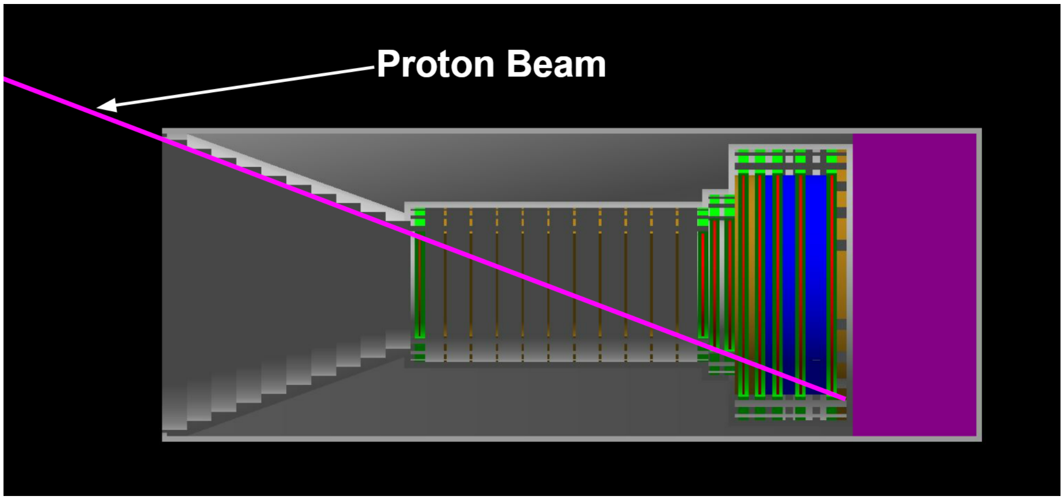

Figure 3.5: A cross-section of LL-SWEPT in Geant4 showing a proton beam travelling through at instrument along the edge of the entrance cone.

binning efficiency for protons travelling off-axis through LL-SWEPT's FOV. A Geant4 simulation comprising of a pencil beam of 1000 protons with energies from 1 to 450 MeV, at a 1 MeV step size, travelling through the aperture of LL-SWEPT parallel to the entrance cone angle is run. The simulation setup is shown in Figure 3.5. This simulation represents the worst case scenario for off-axis particles traveling through LL-SWEPT's aperture within the FOV and are still able to satisfy the coincidence condition. Figure 3.6 compares the binning efficiency, using the bin thresholds shown in Table 3.5, for the on-axis and angled proton beam cases. The black vertical lines are the proton energy threshold values which define each proton energy channel, specified in the right hand side legend of each plot.

As expected, the top plot of Figure 3.6 shows there is a range of protons sorted into energy bins which exceed its upper threshold limit. As the proton energy channel number increases, the number of protons sorted into an incorrect and lower energy bin increases. However, the discrepancy between upper channel threshold and proton energies sorted into its channel remains below 25 % of the energy channel width. The angled protons are counted 15 to 20 % less efficiently than the on-axis particles. Even for the worst case off-axis proton beam travelling along the edge of the entrance cone through LL-SWEPT's FOV and the current binning regime is still able to sort particles

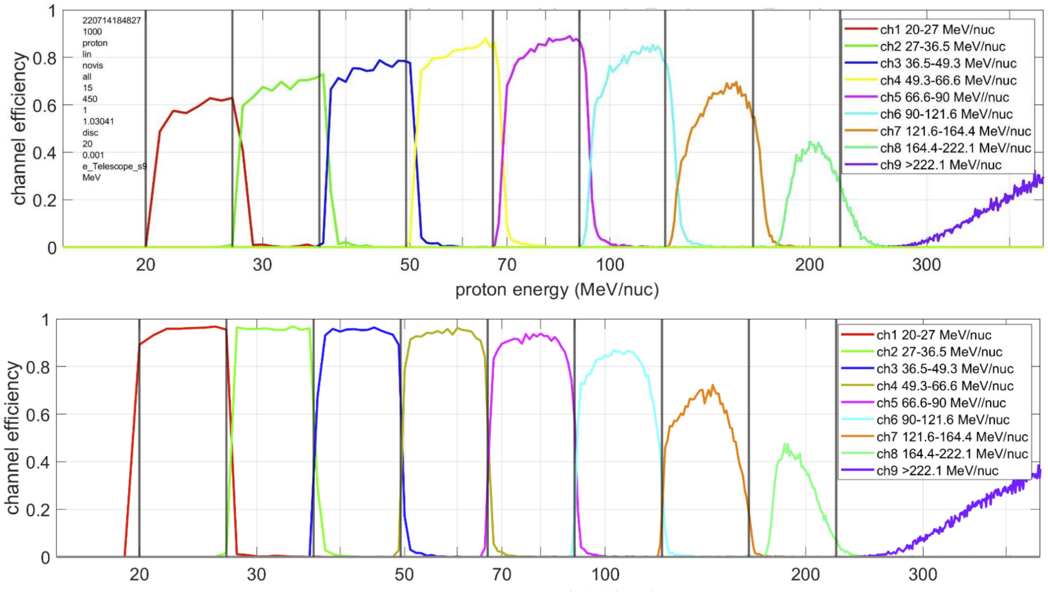

Figure 3.6: LL-SWEPT binning efficiency for protons travelling through the FOV at a 20 ° angle along LL-SWEPT's entrance cone (see Figure 3.5) (top panel) and on-axis through LL-SWEPT's aperture (bottom panel). The black vertical lines show the upper and lower thresholds for the energy channels.

with adequate binning resolution and efficiency. This simulation serves as a quick, measurable check to ensure that at the worst case, the proton energies are still resolvable for incidence angles up to or at the edge of the FOV.

3.3.2 Energy-dependant Geometric Factor

LL-SWEPT's response to an isotropic particle source gives a comprehensive picture of the instrument's ability to identify energetic particles travelling through the FOV into logic channels and to reject side penetrating particles. An isotropic source is a better representation of the space environment LL-SWEPT will operate in, noting that the lunar surface may provide some directional shielding as well as generate secondaries from the lunar surface, and SEP flux directionality changes throughout the event. The energy-dependant geometric factor of the instrument can be found with such isotropic source simulations. Blocking LL-SWEPT's aperture during isotropic source simulations is a method used to determine how effectively the coincidence detection can discriminate against particles travelling outside the FOV.

The isotropic particle source is created in Geant4 by shooting particles from randomly distributed points from the surface of a sphere centred at the geometric centre of LL-SWEPT. The particles are directed inward and have a random cosine distribution from each point on the inside surface of the sphere. A cosine distribution defines the intensity of each particle's direction as proportional to the cosine of the angle between the direction of a given particle and the normal of the surface element is it incident from (e.g., Zhao et al., 2013). The radius of the sphere is large enough to fully encompass LL-SWEPT. The equivalent isotropic particle fluence (counts/cm^2/sr) generated from the sphere per steradian is found with the following equation:

$$I = \frac{N}{4\pi^2 R^2}, \tag{3.1}$$

Where N is the total number of particles shot from the inside surface of the sphere and R is the radius of the sphere, in cm. With the counts recorded by LL-SWEPT during the isotropic simulations, the geometric factor of the instrument can then be determined with the Equation 2.3.

Protons from 15 to 270 MeV with a step size of 1 MeV and 10,000,000 protons per step were shot from an isotropic source with a radius of 20 cm surrounding LL-SWEPT. Figure 3.7 shows the energy-dependant geometric factor for protons. At lower energies, the geometric factor is around 1.2 cm^{2}sr, slightly lower than the targeted 1.3 cm^{2}sr. Only protons sorted into the energy channels are counted in the energy-dependant geometric factor calculation. As expected, the geometric factor decreases at higher energies with binning efficiency.

As mentioned, LL-SWEPT's ability to discriminate against off-axis particles travelling outside the FOV can also be addressed with isotropic Geant4 simulations. In this case, the front aperture of LL-SWEPT is fully blocked with a mass of sufficient stopping power to prevent protons from travelling through the instrument's FOV and registering as a valid event, i.e a particle travelling through the aperature inside the FOV. Therefore, any apparent true count which is registered is considered to be a false positive count.

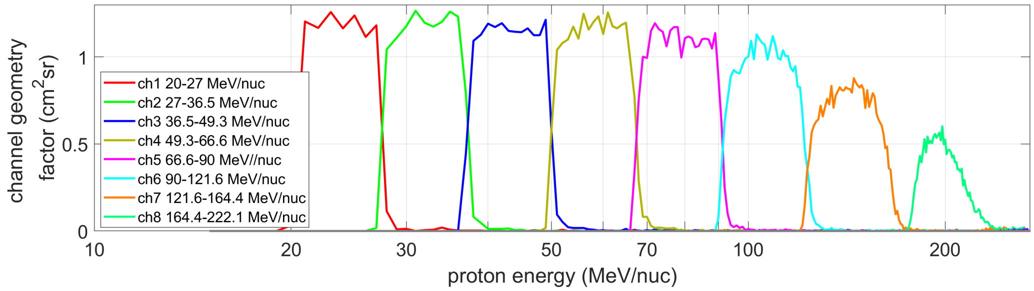

Figure 3.7: Energy-dependant geometric factor for LL-SWEPT baseline geometry for protons. The data plotted is from an isotropic proton source simulated in Geant4.

When the aperture is blocked, the isotropic proton source of one million protons at each energy step up to 180 MeV triggers a non significant (less than 15) false positive true counts. After 180 MeV, the false count rate increases since > 180 MeV protons begin to have enough energy to travel through the backside shielding of the instrument and all nine detectors, triggering the coincidence condition.

Section 3.4 details an additional method to differentiate between high energy forward and backward penetrating particles which satisfy the coincidence condition.

3.3.3 Dead Time Estimation

A dead time of a particle detector is defined as the amount of time any one of its silicon detectors spends processing a false event. During the dead time, the data acquisition system is unavailable to digitize, or unable to digitize with sufficient accuracy, any subsequent event. This hinders the performance of the instrument as a valid event may be missed completely, or energy depositions in one or more detectors could be missed which prevent the particle from being properly identified. Dead time is minimized with faster electronics, reducing the size of the detectors to minimize counting rate, or increasing the amount of shielding around the instrument to prevent off-axis particles with energy below a certain threshold from reaching the detectors. Shielding can provide some protection from lower energy particles, but to fully protect LL-SWEPT from the range of particle energies expected within SEP events and GCRs would require unreasonably large wall thickness (e.g., Posner, 2007).

The first order deadtime analysis simply finds the geometric factor of each detector in LL-SWEPT with Equation 2.3. A first order analysis is currently acceptable for LL-SWEPT as it likely measure only GCR flux during its 14 day mission. Equation 2.3 assumes each detector has no shielding, and both sides of the detector are unobstructed to isotropic particle source. This is done to be conservative and to simplify the analysis. The geometric factor of each detector is multiplied by the proton and alpha particle GCR integral source for particles between 1 to 10,000 MeV over a solid angle of 4π str, see Section 2.5 for GCR integral flux rates. A conservative dead time of one microsecond is assumed for every energy deposition event. This assumption is based on the maximum dead time output by the impulse response function for a energy deposition of a 40 MeV proton (with additional contingency) used in previous SWEPT contracts. To see a more detailed dead time estimation for P-SWEPT, see Figure 4.7 in Section 4.3.2. In reality, the dead time is dependant on the amount of energy deposited, but once again this is a conservative estimate that adds simplicity. Summing up the deadtime in each detector yields a total dead time fraction of 0.357%. In most cases, off-axis particles will travel through multiple detectors and deposit energies in multiple detectors at once. In this case, multiple detectors are dead simultaneously and not all equally contributing to the dead time fraction.

The LL-SWEPT summed dead time fraction is very low, even assuming bare detectors and a one microsecond dead time for each energy deposition event. Additionally, if a detector in the back of LL-SWEPT's stack is compromised, it does not prevent LL-SWEPT from making meaningful measurements of lower energy particles with its first few detectors. The 20 MeV side, and 60 MeV back, shielding which represents the shielding effects of the structure does not need to be increased to properly measure GCRs.

In the rare event of a large SEP event during LL-SWEPT's mission, the shielding around LL-SWEPT may not be enough to keep the deadtime of the detectors within reasonable limits. The National Oceanic and Atmospheric

Administration (NOAA) defines a SEP event as moderate when the integral proton flux > 10 MeV exceeds 100 counts/s/cm^2/sr. It is expected that moderate SEP can occur up to 12 times per year. A minor SEP event is reached when proton flux > 10 MeV exceeds 10 counts/s/cm^2/sr. Minor events may occur on average up to 20 times per year during solar max. Based on this dead time analysis, if a minor or moderate SEP event was to occur during LL-SWEPT's operational lifetime the increase in proton flux alone would saturate instrument and prevent its ability to make meaningful measurements, suggesting that additional shielding may be required. An in-depth analysis, similar to the one completed for P-SWEPT in Section 4.3, can be completed for a more accurate deadtime fraction estimate for LL-SWEPT during a SEP event of various sizes. However, it may be within an acceptable amount of risk to keep LL-SWEPT minimally shielded in attempts to keep the mass of the instrument low, if the mission on the lunar surface is confined to only 14 days.

3.4 LL-SWEPT Back Shielding Analysis

An analysis is performed to determine how LL-SWEPT responds to protons incoming from the back side of the instrument. Higher energy particles travelling through the back of the instrument that penetrate the entire detector stack without stopping could be misidentified as a proton entering through the front aperture of the telescope since such particles deposit similar amounts of energy in each detector and satisfy the coincidence condition. The on-board electronics are not fast enough to resolve the time between energy depositions in two subsequent detectors, so it will not be possible to determine the direction of a particle by following its trajectory through LL-SWEPT with the timing of energy depositions in the detector elements in the stack. This can be seen from the average energy deposition per detector for protons > 200 MeV in Figure 3.2 and for alpha particles > 700 MeV in Figure 3.4. Increased shielding on the backside of the instrument can prevent particles from travelling through the backside of the instrument. However, the amount of shielding required to stop particles at the higher energy range of GCRs and SEPs is unrealistic for a lunar mission where low mass is a priority. A method to determine the directionality of high energy particles is needed and is presented in this section.

Back penetrating protons can be simulated by shooting a pencil beam directly through the backside of LL-SWEPT along the long axis in Geant4. Lower energy (15 to 180 MeV) protons deposit their peak energy deposition within the detector stack and therefore are easily differentiated from protons travelling through the front aperture since they do not reach the front coincidence detector. These particles will already be rejected as they do not satisfy the coincidence condition of depositing energy into the first two detectors. Figure 3.8 shows the average energy deposition as function of proton energy for protons of energies from 10 to 370 MeV (1000 protons per step, 1 MeV step size) travelling on-axis through the backside of the instrument, simulated in Geant4. Comparing Figures 3.8 and 3.2, one can easily make the distinction between forward and backward penetrating protons between energies 20 to 180 MeV by examining the energy deposited into each detector.

An additional method is however required to determine the direction of higher energy particles which deposit energy in all nine detectors and do not deposit a Bragg Peak energy deposition in any of them. A distinguishing feature between $>$ 200 MeV protons travelling forward and backwards through the telescope for a given energy is the linear least-squares trend line of the average energy deposition as a function of detector number. The trend line is typically positive for protons entering through the front aperture and negative for backward-incident protons. The slope can be used to discriminate between forward and backward penetrating protons. Figure 3.9 shows the average energy deposition of a 250 MeV proton as a function of detector number for forward and backward penetrating protons as an example to show the difference in linear trend lines. The energy deposition values are derived from the average of 10,000, 250 MeV backward and forward penetrating protons, Figure 3.9 demonstrates how the linear slope can be used to determine the direction of the protons.

When a proton event deposits energy in all nine detectors, a least-squared

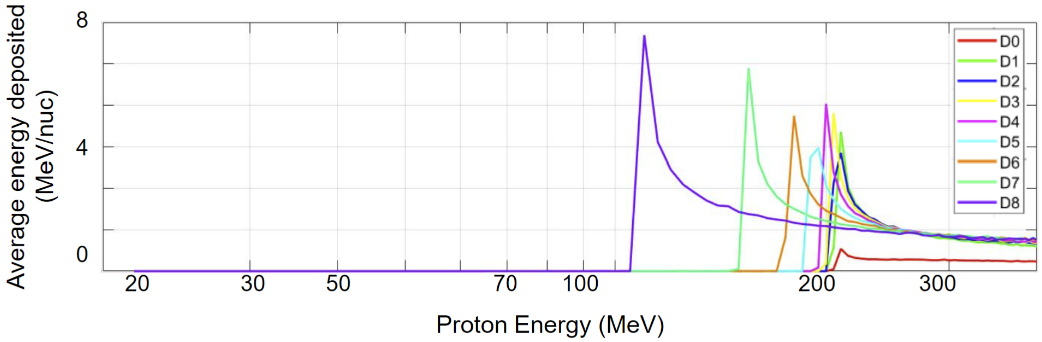

Figure 3.8: Average energy deposition per detector for a proton beam travelling directly through the backside of LL-SWEPT, simulated in Geant4.

linear trend line is calculated and the sign of its slope is checked. If the slope of the fit line is negative, the proton can be assumed to have traveled through the back of the instrument. If it is positive, the proton can be assumed to have traveled through the front aperture. To check how accurately this simple algorithm can discriminate between forward and backward proton particles, the sign check is applied to 225 to 300 MeV protons at a 25 MeV step size and 10,000 protons at each step entering through the entrance aperture and through the back of the instrument in Geant4. From the 10,000 protons, events which do not deposit energy in all nine detectors are discarded. The linear trend line is therefore calculated for protons which deposited energy into every detector. The accuracy for each direction is found by dividing the number of events which have a positive and negative slope sign by the number of events which deposit energy into every detector. Table 3.6 shows the results of the sign check for protons with selected energies in the 225 to 300 MeV range.

Detector D0 is thinner than the rest of the detectors, so protons deposit less energy into it. This skews the linear trend line calculation, so detectors D1 through D8 are used to calculate the energy deposition slope. As proton energy increases, protons travelling through the instrument increasingly deposit similar energy deposition in each of detectors 2 through 8, as shown in the $>$ 200 MeV energy range of the average energy depositions for protons in Figure 3.2. As the amount of energy deposition in each detector becomes closer together, the linear slope of the energy deposition vs. detector number

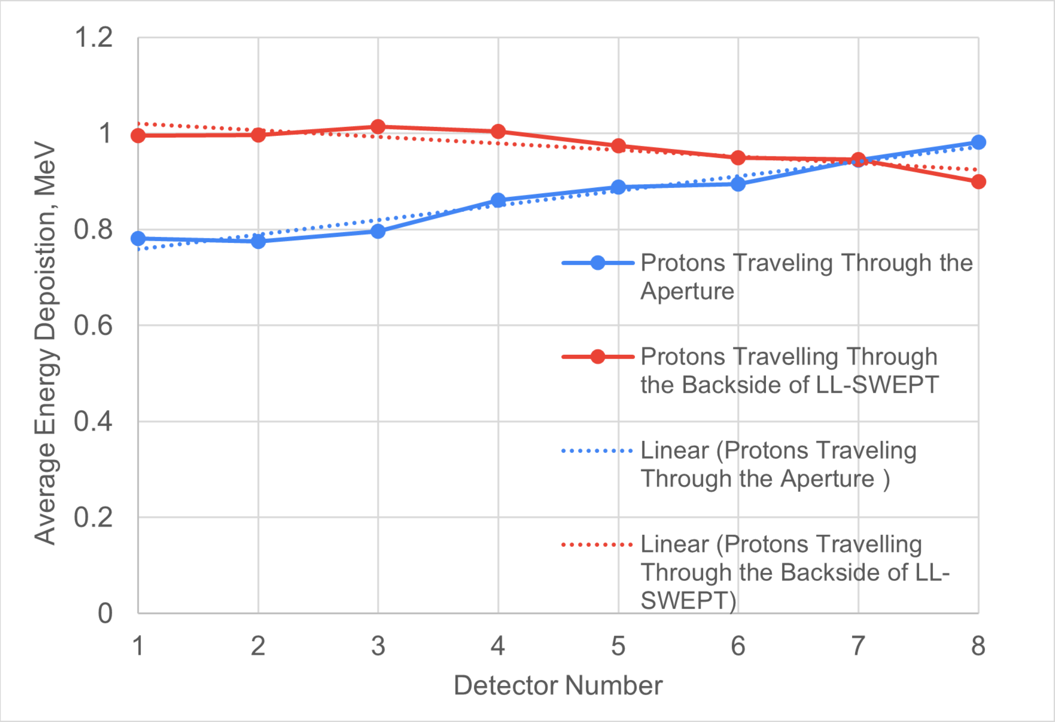

Figure 3.9: Average energy deposition per detector for a 250 MeV proton pencil beam travelling along axis through LL-SWEPT's aperture and through the backside of the LL-SWEPT simulated in Geant4.

Table 3.6: The accuracy with which the sign-check gradient algorithm correctly identifies the direction of proton events which deposit energy in all nine detectors over the 225 to 300 MeV range.

Forward incident protons				
Proton Energy	225 MeV	250 MeV	275 MeV	300 MeV
Number of protons whose slope is positive	7668	8145	7668	7272
Number of protons whose slope is negative	1865	1330	1865	2687
% Accuracy	80.45%	85.98%	80.25%	75.35%
Backward incident protons				
Proton Energy	225 MeV	250 MeV	275 MeV	300 MeV
Number of protons whose slope is negative	5330	5084	5434	7068
Number of protons whose slope is positive	475	119	478	2772
% Accuracy	91.85%	97.75%	95.17%	84.27%

becomes more shallow. This increases the chance the slope does not match the correct sign for the particle's direction, which reduces in the efficiency of the slope check.

The efficiency of this additional gradient algorithm negates the need for additional shielding at the backside of the instrument. An identical study can be performed for alpha particles and other ion species present in GCRs, and similar results are expected. LL-SWEPT's gimbal mount will also provide additional shielding to the backside of the instrument to further protect the instrument from higher energy backward penetrating particles. With the accuracy of the gradient sign check algorithm well characterized over a range of high energy protons, the actual number of protons travelling in both directions can be corrected for in post processing.

3.5 High-Energy Identification Regime

Up to energies around 165 MeV, the efficiency of the method to identify proton energies by comparing energy deposition values from each detector to logic thresholds, as described in Section 3.2.1, is significantly reduced for the higher energy protons. Protons with excess of 165 MeV have just enough energy required to travel through the detector stack without stopping, depositing a peak energy deposition within the last detector. Without this signature, it becomes increasingly difficult to accurately sort the energies of > 165 MeV protons. As seen in Figure 2.4, > 165 MeV protons make up a large portion of the expected SEP and GCR flux. LL-SWEPT is required to measure 30 to 300 MeV protons, derived from the expect proton populations in the SEP and GCR spectra. Therefore, a different energy identification method is required to accurately identify these higher energy protons. In this section, an energy identification algorithm is presented whose preliminary results show that it is able to identify 160 to 370 MeV protons with the improved efficiency to the logic table method. The algorithm may also be computationally simple enough to be completed on-board. In this case, large raw datasets do not need to be down-linked to Earth, saving communication resources. As shown in

Section 3.2.1, the logic table method is simple, robust and identifies the energy of protons with sufficient efficiency and resolution up to 165 MeV protons. Therefore, this method will still be used to measure lower energy protons between 15 to 165 MeV. This identification method is called the low energy regime through the rest of this thesis. The initial sorting of particles into the low and high energy regime, the methodology behind the high energy regime algorithm, and Geant4 simulations showing the algorithm's performance are presented below.

First, measured proton events are sorted into either the low or high energy regime. Protons which deposit energy into all nine detectors or are sorted into the low energy regime's last two energy channels (see Figure 3.3) are sorted into the high energy regime. The remainder of the protons are sorted into the low energy regime, as described in Section 3.2.1. The lower energy threshold of the high energy regime is around 165 MeV, the approximate energy at which protons travel through all nine detectors without depositing their peak energy deposition. The high energy regime compares the energy deposition in each detector to thresholds which define minimum and maximum energy ranges for three new high energy channels: 165 to 240 MeV, 240 to 370 MeV and $>$ 370 MeV. The values are manually tuned to achieve maximum binning efficiency. The thresholds values for these high energy channels are based on the expected energy deposition values in each detector for a proton at the channel threshold energy. Table 3.7 presents the energy deposition thresholds per detector used to create the high energy channels. The proton is sorted into the energy channel in which most of its detector's energy deposition are sorted into, i.e. the majority vote of all detector assignments.

For example, consider a proton that deposits energy shown in Table 3.8 into each detector. The energy deposition value in each detector is compared to the threshold values for the respective detector in Table 3.7. In this example, detectors one through four have a larger energy deposition than the 240 MeV threshold, so they are labeled as channel one (165 to 240 MeV). Detector five and nine is between the 240 and 370 MeV values, as is assigned channel two (240 to 370 MeV). The rest of the energy depositions are less than the

Table 3.7: Energy deposition values for 240 MeV and 370 MeV bin thresholds values for each detector in LL-SWEPT. Energy depositions in each detector are compared to these values to determine the high energy channel they are assigned to.

Energy Threshold	Energy Deposition (MeV) per Detector								
	1	2	3	4	5	6	7	8	9
240 MeV	0.3836	0.7397	0.7430	0.7484	0.7529	0.7539	0.7700	0.7959	0.8319
370 MeV	0.3187	0.6085	0.6150	0.6230	0.6186	0.6267	0.6232	0.6366	0.6423

Table 3.8: Example energy deposition values for a proton travelling through the LL-SWEPT instrument.

Energy Deposition (MeV) per Detector								
1	2	3	4	5	6	7	8	9
0.4120	0.8014	0.7943	0.7782	0.6635	0.6032	0.6161	0.6199	0.7012

370 MeV threshold, so they are assigned channel three (> 370 MeV). High energy channel one (165 to 240 MeV) has the most detectors assigned to it, therefore this proton is assigned to the first channel of 165 to 240 MeV. In the case where an equal number of detectors are assigned to more than one channel, the proton is automatically assigned to high energy channel 2 (240 to 370 MeV). It can be expected that events whose detectors are assigned to multiple bins have energies close to the middle of the high energy range. This corrective measure is shown to increase the binning efficiency for protons. The bottom plot of Figure 3.10 shows the binning efficiency as a function of proton energy for the low energy regime and the top plot is combined low and high energy regime. The data used to create both plots in Figure 3.10 is from a Geant4 simulation in which a pencil beam of protons with energies from 1 to 450 MeV with a 1 MeV stepsize, and 1000 particles per step, are shot directly through LL-SWEPT's front aperture. The high energy channel efficiency at each proton energy is found by dividing the number of particles sorted into each energy bin by the number of particles simulated at each energy step.

As mentioned previously, the on-axis proton simulations represent the best case instrument performance. It does not take off-axis or backwards travelling particles which may trigger the coincidence detection and be erroneously counted as a true count into account. It also does not simulate off-axis particles travelling inside the FOV which deposit more energy into each detector as

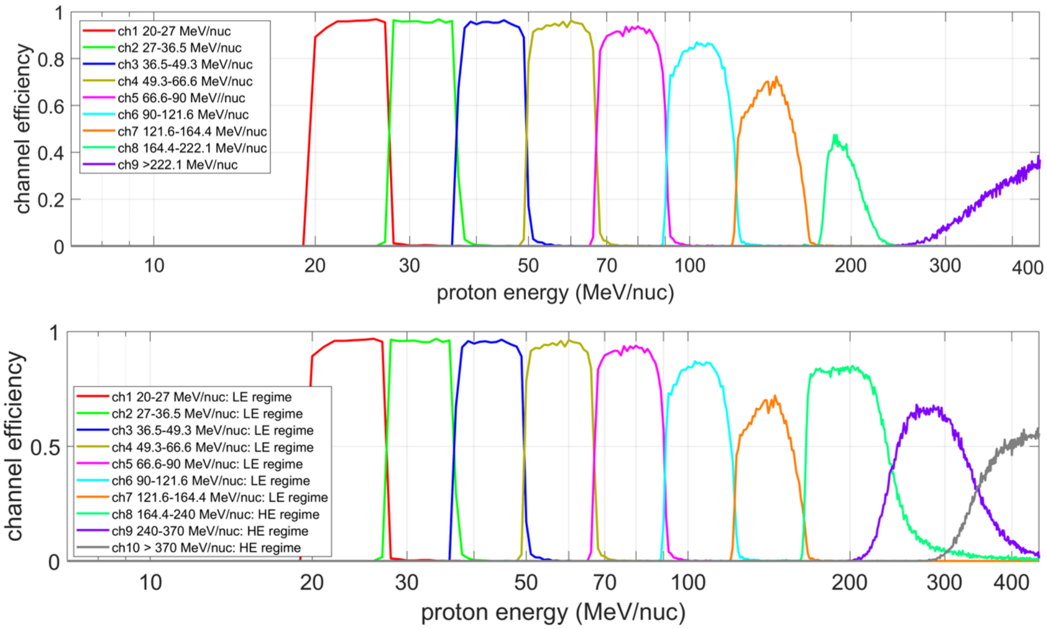

Figure 3.10: Top panel: LL-SWEPT axial proton binning efficiency as a function of proton energy using the low energy regime only. Bottom panel: LL-SWEPT axial proton binning efficiency using both high and low energy binning regime. The data from both plots are from a proton pencil beam incident on-axis through the aperture in Geant4.

they travel diagonally through the material of the detectors in the instrument. Therefore, isotropic Geant4 data is used to determine the energy-dependant geometric factor in the high energy regime. The same Geant4 simulation set up as presented in Section 3.3.2 is used, except the simulated proton energy range is increased to 600 MeV to properly capture the range of proton energies which the high energy regime is able to identify. Figure 3.11 shows LL-SWEPT's energy dependant geometric factor using both the low and high energy regime to sort protons into energy channels. The data plotted in Figure 3.11 is from a Geant4 simulation imparting an isotropic proton source from 1 to 600 MeV at 1 MeV energy steps and 10,000,000 protons per step. The isotropic source set up is the same as described in Section 3.3.2.

The trend line sign check detailed in Section 3.4 to identify and discriminate against backward travelling high energy protons is added to the data processing used calculate LL-SWEPT's on-axis channel efficiency and energy dependant geometric factor. Without this measure, the maximum geometric factor above

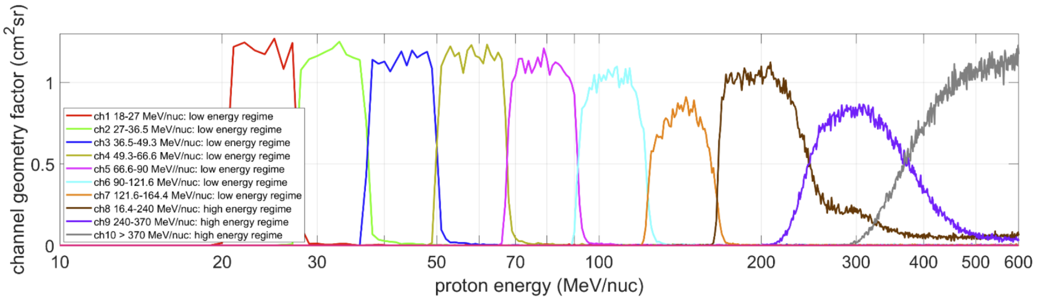

Figure 3.11: Energy-dependant geometric factor as a function of proton energy for LL-SWEPT, employing the low and high energy identification regime. The data is from an isotropic electron source simulated in Geant4.

200 MeV exceeds 2 cm^{2}sr as it is erroneously counting high energy backward incident protons as valid events.

The high energy regime keeps the geometric factor of LL-SWEPT within a reasonable range of its nominal geometric factor to 370 MeV. The last energy channel is a integral channel for all particles above 370 MeV. Due to the nature in which protons are sorted, the high energy energy channels have larger transition periods between successive bins. The channel thresholds are defined as the point where the channel geometric factor curves cross. Comparing 3.10 and 3.11, the upper energy channel thresholds for the geometric factor channels are slightly larger than the on-axis channel efficiencies thresholds. Shown in Section 3.3.1, protons travelling at angles inside the FOV deposit larger amounts of energy into each detector than protons travelling directly through the detectors. Since the high energy regime depends on a majority vote of detector energies to sort protons into bins, it only requires 3 of 9 detector energy depositions to be larger than the channel threshold to be sorted into the lower energy bin. This makes the high energy regime more susceptible to an extended upper energy threshold when particles travelling at all angles through the FOV are simulated. In the lower energy regime, such protons may be rejected from the binning logic entirely.

3.6 LL-SWEPT Summary and Future Work

In this chapter, LL-SWEPT's geometry and energy identification algorithm is matured from a previous version of the SWEPT instrument to better suit for detection of GCRs and SEPs during a short-term mission on the lunar surface. LL-SWEPT is able to make differential energetic proton measurements from 20 up to 370 MeV, extending past the 30 to 300 MeV proton measurement requirement. By verifying the energy dependant geometric factor from isotropic Geant4 simulations, the coincidence detection along with the side and back shielding is sufficient to prevent particles travelling off axis through the side of LL-SWEPT to be counted as a true count. LL-SWEPT is also able to measure alpha particles from 80 to 660 MeV, with no modifications to the layout designed to measure protons. To better characterize LL-SWEPT's response in Geant4, SEP and GCR environments, along with lunar albedo particles should be simulated in the Geant4 particle sources. Modelling LL-SWEPT's gimbal mount and the lunar lander structure in higher fidelity will provide more shielding than what is currently represented in the Geant4 model and will further reduce the dead time. A comprehensive dead time analysis, similar to what is preformed on P-SWEPT, see Section 4.3.2, should be preformed on the instrument to determine the largest SEP event for which LL-SWEPT can make meaningful measurements in. The high energy regime can be extended to sort and measure alpha particles, and its ability to measure angled particle flux through the FOV needs to be characterized. Characterizing the noise in the silicon detectors used in the LL-SWEPT model to determine that the minimum resolvable signal is well below the minimum threshold values in order to verify LL-SWEPT's measurement accuracy.

Chapter 4

P-SWEPT

The Planetary Sweeping Energetic Particle Telescope (P-SWEPT) is the second variation of the energetic particle telescope, designed for operation on the Lunar Gateway. As this chapter will show, P-SWEPT's overall mechanical design and particle detection technique is similar to that used for LL-SWEPT, and presented in Chapter 3. However, the layout and shielding of P-SWEPT are optimized for a long-term lunar orbiting mission rather than for monitoring the particle flux during a short term mission on the lunar surface.

P-SWEPT's geometry and shielding is shown in Figure 4.1. P-SWEPT shares many of the geometrical characteristics of LL-SWEPT, therefore the results from the back penetrating protons (Section 3.4), angled protons travelling inside the FOV (Section 3.3.1), and alpha particle response (Section 3.2.2) studies completed for LL-SWEPT can are carried over to P-SWEPT and will not be repeated in this chapter. A detailed dead time analysis, using Geant4 simulations that takes an energy-dependent dead time fraction into account, is completed for P-SWEPT to ensure that it can operate effectively during the worst case expected SEP flux. The baseline design for P-SWEPT has a 27 cm by 10.1 cm by 10.1 cm volume envelope and has a mass of 4.9 kg.

P-SWEPT's primary goal is to measure the angular dependence of high energy solar energetic particles outside the Earth's magnetosphere in interplanetary space. The sources of particle flux are primarily SEPs, GCRs and neutron secondaries generated by interactions with spacecraft material. More information on the relevant space environment and expected particle fluxes can

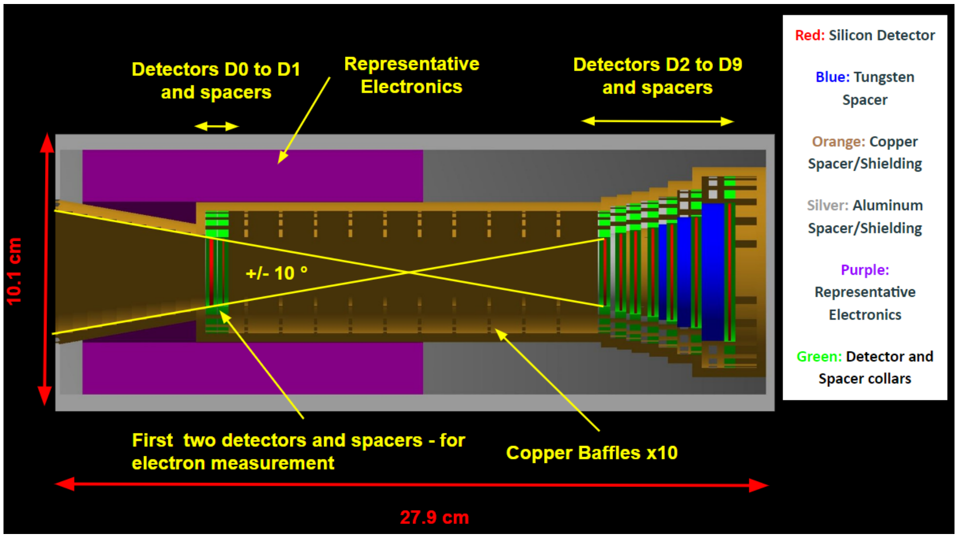

Figure 4.1: An annotated cross section of P-SWEPT baseline geometry in Geant4.

be found in Chapter 1. Measurements of the angular-dependent particle flux is important for the effective design of future radiation shielding for crewed planetary exploration missions, in terms of optimizing the directionality and thickness and composition of the spacecraft shielding needed to protect astronauts and hardware. Unlike LL-SWEPT, P-SWEPT is not limited by its inability to survive the harsh lunar night, allowing the mission lifetime to be extended to five years or more. Over P-SWEPT's mission lifetime, extended measurements can be made on the intensity and number of SEP events at different times in the solar cycle. P-SWEPT is also designed to measure electron flux which precede the proton SEP events, more details on the expected electron flux is detailed in Section 2.4.2.

4.1 P-SWEPT Instrument Introduction

Similar to LL-SWEPT, P-SWEPT measures energetic particles based on their energy deposition in a stack of silicon detectors. The radius and spacing between the detectors D1 and D2 define P-SWEPT's geometric factor, see Figure 4.1 for detector location within the instrument. Copper baffles between detectors D1 and D2 prevent scattered and off-axis particles from travelling into the rest of the detector stack. Protons with energy greater than 22 MeV can travel through detectors D0 to D2 to reach the rest of the detector stack without stopping, this defines the lower proton energy limit for P-SWEPT. Only proton events which deposit energy in detectors D1 and D2 are counted as events travelling through the P-SWEPT FOV. The radius of the detector stack increases with detector number, to allow particles travelling through the aperture along the inside of the entrance cone to be successfully measured by the detectors deeper in the stack. The larger back detectors also ensure that higher energy particles which scatter as they travel through multiple detectors are still sufficiently counted by the instrument.

P-SWEPT has two detectors at the front of the instrument directly behind the entrance cone primarily to facilitate electron measurements. Therefore, the nominal geometric factor is calculated with the radius and spacing of detectors D1 and D2. P-SWEPT has a 10° full angle conical FOV and the radius and separation distance between detectors D1 and D2 yield a 0.113 cm^2sr geometric factor, using Equation 2.4. The geometric factor balances P-SWEPT's ability to measure the lower GCR flux while preventing the instrument from becoming saturated during the worst case SEP events. A cross section of P-SWEPT's baseline design is shown in Figure 4.1 and shows the P-SWEPT has a 6 mm aluminum outer packing and a 3.4 mm copper support wall. Behind the detector stack, 7.8 mm of copper shielding protects against particles travelling through the backside of the instrument. The cumulative shielding from the support wall, back shielding and outer packaging stops protons lower than 60 MeV from travelling from the side of the instrument, and 100 MeV protons from travelling through the back. Aluminum, copper, and tungsten degraders in between the detectors increase the energy range of protons which come to rest in the stack, expanding the upper energy range, similar to LL-SWEPT.

P-SWEPT's representative electronics package is modeled as the purple volume surrounding the entrance cone of the instrument in Figure 4.1. The position of the electronics is arbitrary; however, in this configuration the electronics and its enclosure provides additional shielding for detector D0 and D1 from off-axis particles travelling through the entrance cone from the side of P-SWEPT. It is expected the P-SWEPT electronics will be radiation hard-

Table 4.1: P-SWEPT baseline geometry dimensions.

P-SWEPT Subcomponent Geometry		
Parameter	Value	Unit
Number of Detectors	10	
Geometric Factor	0.113	cm^2sr
FOV (1/2 angle)	5	°
Support Wall Thickness (Copper)	3.39	mm
Back Shielding Thickness (Copper)	7.81	mm
Outer Package Thickness (Aluminum)	6	mm
Detector Collar Thickness (PCB Material)	4	mm
Spacer Collar Thickness (PCB Material)	3	mm
P-SWEPT Overall Dimensions		
Width	10.1	cm
Length	26.9	cm

ened and therefore not susceptible to additional damage arising from being mounted in this location. As the electronics design for P-SWEPT matures, the electronics can be better represented in the Geant4 model. Similar to LL-SWEPT, the material, surface area and height of the representative electronics are based on design work from previous SWEPT contracts and is scaled to the number of detectors in the stack. The composition of the representative electronics material is shown in Table 3.1 and is based on typical materials found in printed circuit boards (Gerbase and Oliveira, Camila Reis de, 2012).

Tables 4.1 and 4.2 show the size and mass breakdown of the P-SWEPT baseline geometry. Details for the detector thicknesses and degrader material and thicknesses are given in Table 4.3.

4.1.1 P-SWEPT Proton Response

Geant4 simulations are used to determine P-SWEPT ability to measure protons. A proton pencil beam incident on-axis through the centre of the P-SWEPT's aperture from 7 to 600 MeV at 1 MeV step size and 1000 protons per step is simulated in Geant4. The top panel of Figure 4.2 shows the average energy deposition as a function of proton energy in P-SWEPT's ten silicon detectors. Protons which deposit energy in the detectors D1 and D2 satisfy

Table 4.2: P-SWEPT baseline geometry mass breakdown.

Mass	Value (kg)	% of Total Mass
Total Mass	4.93	
Collar Spacer Mass	0.07	1.4%
Detector Spacer Mass	0.06	1.2%
Spacer Mass	0.50	10.1%
Detector Mass	0.01	0.2%
Backplate Mass	0.27	5.5%
Baffle Ring Mass	0.12	2.4%
Entrance Cone Mass	0.25	5.1%
Wall Mass	1.23	24.9%
Outer Package Mass	1.88	38.1%
PCB Mass	0.54	11.0%

Table 4.3: P-SWEPT silicon detector thicknesses and degrader material and thicknesses.

Detector	Silicon Detector thicknesses		Degrader thicknesses (positioned before the detectors)		
0	0.15	cm	Aluminum	0.025	cm
1	0.05	cm	Aluminum	0.025	cm
2	0.10	cm	Aluminum	0.011	cm
3	0.10	cm	Aluminum	0.052	cm
4	0.10	cm	Copper	0.182	cm
5	0.10	cm	Copper	0.131	cm
6	0.10	cm	Tungsten	0.240	cm
7	0.10	cm	Tungsten	0.290	cm
8	0.10	cm	Tungsten	0.486	cm
9	0.10	cm	Tungsten	0.815	cm

the coincidence condition and are sorted into high and low energy identification regimes. The principles behind the low and high energy identification regimes are the same as described for LL-SWEPT in the previous chapter. See Sections 3.2.1 and 3.5 for details on the low and high energy identification regimes. Detector D0 is not included in the coincidence condition and is essentially used as a degrader to reject lower energy protons from entering the detector stack. Detector D0 is exclusively used to make electron measurements, see Section 4.2 for more details. The low energy channel widths for P-SWEPT and LL-SWEPT are of similar size. However, since the lower and upper energy thresholds are based on the expected energy deposition in each detector, the threshold values are changed in the low and high energy regime for P-SWEPT to accommodate the differences in detector number and thickness. An additional high energy channel is added for P-SWEPT. The logic tables for P-SWEPT's high and low energy regime are found in Appendix A.

The top plot of Figure 4.2 shows the average energy deposition as a function of proton energy. As shown in figure 4.2, the average energy deposition of detector D0 has a large relative maximum due to its larger thickness (1.5 mm) compared to the rest of the detectors in the stack. The bottom panel of Figure 4.2 shows the binning efficiency into the energy bins listed Appendix A up to 600 MeV protons for the low and high energy regime. The sign check algorithm used to differentiate between particles incoming through the front and back of the instrument (see Section 3.4 for more details) is employed when finding the channel efficiency plotted in Figure 4.2. Despite the proton pencil beam only being incident on P-SWEPT's entrance aperture in the Geant4 simulation, the sign check algorithm is applied to make the sorting algorithm identical to what is used when calculating the energy dependant geometric factor. Similar to LL-SWEPT, the low and high energy binning algorithms are able to measure protons with sufficient efficiency and energy resolution with energies up to and exceeding 300 MeV, which is the required minimum upper energy range for P-SWEPT to make comprehensive measurements of GCRs and SEP events.

An isotropic proton source is be used to determine P-SWEPT's energy-dependent geometric factor. This measure provides a better picture of the

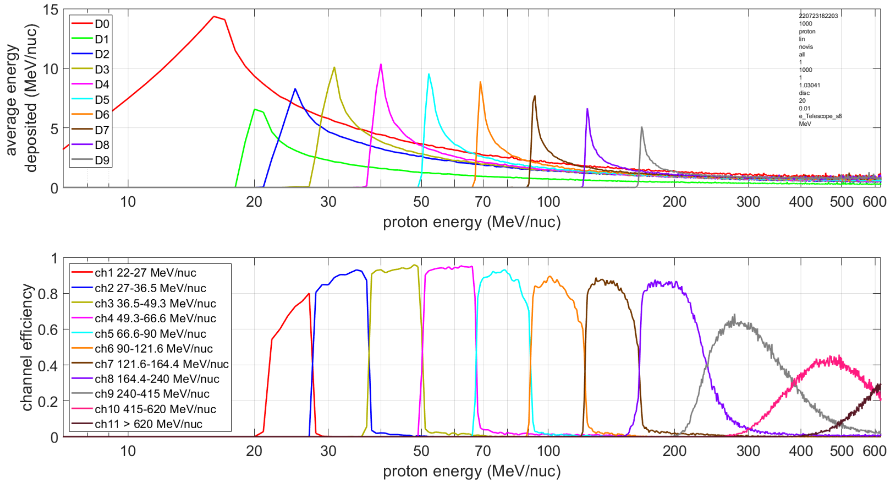

Figure 4.2: Top panel: P-SWEPT's average energy deposition for a proton pencil beam travelling on-axis through P-SWEPT's aperture in Geant4. Bottom panel: P-SWEPT's proton binning efficiency sorted using the high and low energy regime.

instruments counting efficiency as a function of proton energy in the space environment. Protons with energies ranging from 18 to 635 MeV with a 1 MeV step size at 10,000,000 protons per step are generated from the inside surface of a sphere with a radius of 20 cm, positioned at the geometric centre of P-SWEPT. The simulation set up for the isotropic source in Geant4 identical to what is described in Section 3.3.2. Figure 4.3 shows P-SWEPT's energy-dependent geometric factor for the low and high energy regime channels. Using the low and high energy regimes, protons are able to be identified differentially with reasonable (>50 %) efficiency up to 400 MeV, which extends past the instrument's 300 MeV proton measurement requirement. The last four energy channels in the bottom plot of Figure 4.2 and 4.3 (channels 8 through 11) are sorted using the high energy regime. Similarly to LL-SWEPT, the upper channel thresholds in the geometric factor plots occur at a slightly higher energy than the upper thresholds in the axial efficiency plot. Protons travelling at an angle through the FOV deposit more energy in each detector and can be misidentified as a lower energy particle. The channel thresholds energy ranges are based on the proton energy where the geometric factor curves intersect in Figure 4.3.

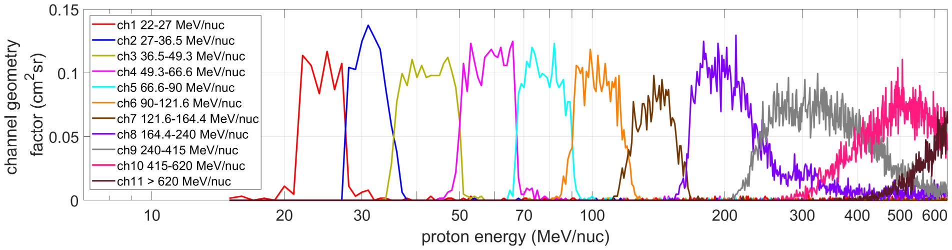

Figure 4.3: P-SWEPT geometric factor as a function of proton energy, using the low and high energy regime. The data plotted is from an isotropic proton source simulation in Geant4.

4.2 P-SWEPT Electron Response

As mentioned in Section 2.4.2, energetic proton populations can be predicted by measuring the relativistic electron flux which can precede the proton flux by up to an hour in advance during a SEP event (e.g., Posner, 2007). Therefore it is useful for P-SWEPT to also be able to measure the electron population and use it as an advance warning for astronauts for the impending and potentially dangerous proton flux. In P-SWEPT, electrons typically deposit energy in detectors D0 and D1. They either stop completely in these detectors or undergo significant scattering before reaching detector D2. Therefore, electrons will exclusively be measured based on the energy deposition in detectors D0 and D1. A thin 0.25 mm aluminum shield in front of detector D0 stops the low energy electrons whose energy deposition values cannot be discriminated from the noise generated by the detectors and electronics. The material and size of all the degraders and detectors in P-SWEPT is shown in Table 4.1.

The Geant4 simulation used to determine the on-axis electron response consist of an electron beam from 0.01 to 5 MeV in 0.01 MeV steps and 1000 electrons per step travelling directly on-axis through the centre of the P-SWEPT aperture. Only energy deposition events above 0.1 MeV are recorded in detectors D0 and D1 as it is expected that any lower signal will not be distinguishable from the noise in the detectors. The top panel of Figure 4.4 shows the average energy deposition as a function of electron energy per detector. There is very little average energy deposition in detectors D2 to D9, supporting the reasoning to exclusively use signals from detectors D0 and D1 to measure

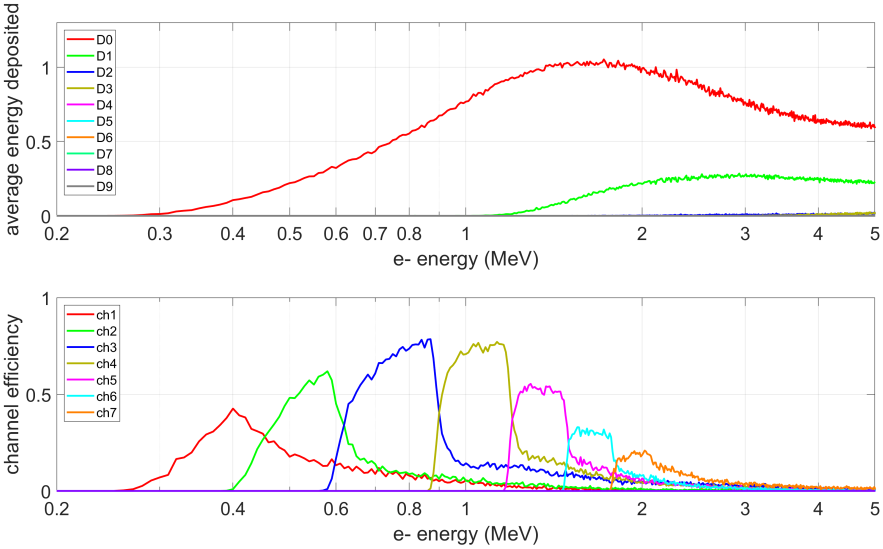

Figure 4.4: Top panel: P-SWEPT's average electron energy deposition as a function of electron energy per detector. Bottom panel: channel efficiency as a function of electron energy. The data plotted is from a Geant4 simulation of an electron pencil beam travelling on-axis through P-SWEPT's aperture.

electrons.

The energy deposited into detectors D0 and D1 are used to sort each electron with energies up to 2.2 MeV to seven energy channels. Electrons which deposit energy into detector D1 are only sorted into the last channel, which defines the high energy electron measurement threshold. Table 4.4 shows the energy deposition range required in detector D0 to be sorted into each channel. The width of the energy bins is determined by trading channel resolution and efficiency.

Unlike protons, P-SWEPT does not have an electron coincidence detection technique. The instrument is currently designed with 0.6 cm of copper and 0.34 cm of aluminum side shielding, thick enough to stop and shield electrons up to around 9 MeV. If these electrons are misidentified as a lower energy electron travelling through the instrument's FOV, >9 MeV electron flux is low enough in SEP flux spectrum to not skew the electron data (e.g. Klecker, 2013). Additionally, protons with energies <1 MeV deposit energy into D0 within the range of the lower electron channels in Table 4.4, and would not reach D1. Such protons are indistinguishable from electrons sorted into the same

Table 4.4: Energy channel thresholds for electron energy identification up to 2 MeV.

Energy Channel Number	Channel energy range (MeV)	Minimum D0 energy deposition (MeV)	Maximum D0 energy deposition (MeV)
1	0.30-0.47	0.1	0.3
2	0.47-0.62	0.3	0.5
3	0.62-0.90	0.5	0.8
4	0.9-1.2	0.8	1.1
5	1.2-1.5	1.1	1.4
6	1.5-1.81	1.4	1.7
7* *Energy can be deposted in D1	1.7-2.2	1.5	2

channels, however such false counts can be corrected for with the expected <1 MeV proton flux during data processing. If the <1 MeV proton flux is expected to significantly skew the electron flux measurements, changes to P-SWEPT's layout to identify the species of low energy particles, such as adding an anti-coincidence detector similar to the RADHEPT instruments (see Section 5.1.2), can be implemented.

The bottom plot of Figure 4.4 shows P-SWEPT's binning efficiency as a function of electron energy. Up to the right edge of energy channel 4 (0.9 to 1.2 MeV), the binning efficiency remains over 60 %. At about 1.0 MeV electron energy, the binning efficiency drops significantly. Electrons with energies above 1.0 MeV consistently deposit energy in detector D1. Electrons scattering outside of the instrument while travelling in between detectors D0 and D1 and failing to deposit within the expected energy range could provide an explanation for the reduction in electron binning efficiency. Reducing the space between the two detectors or increasing the thickness of the D0 could increase the binning efficiency for particles above 1.0 MeV. Currently, the space between each detector in the baseline design is 2.25 mm, corresponding to the thickness of the PCB ring that surrounds the Micron Semiconductor ("Micron Semiconductor Ltd. Silicon Catalouge Long Form," 2018). There are options to procure custom detectors with increased silicon thickness should we determine the need to increase the electron binning efficiency. Due to the drop in efficiency <50 % in energy channels 6 and 7, P-SWEPT is considered capable of measuring electrons with energies from 0.3 to 1.5 MeV.

During its operation, P-SWEPT will be bombarded by electrons from all

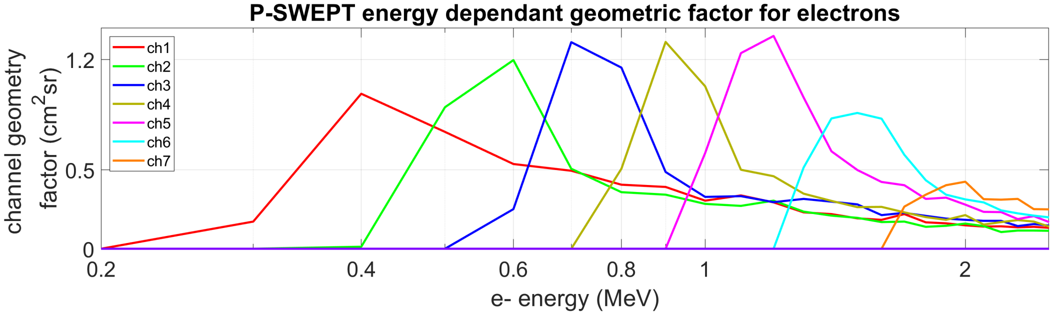

Figure 4.5: Geometric factor for P-SWEPT electrons as a function of electron energy. The data plotted is from an isotropic electron source simulation in Geant4.

directions. An isotropic source Geant4 simulation can be used to determine the energy-dependent geometric factor for the P-SWEPT electron response. A Geant4 simulation shooting an isotropic source of electrons with energies 0.2 to 2.5 MeV, with a 0.1 MeV step size and 10,000,000 was run. The Geant4 simulation set up is similar to that described in Section 3.7, was run. Figure 4.5 shows the energy-dependent geometric factor as a function of electron energy.

As mentioned previously, P-SWEPT does not have a electron coincidence technique, which explains why the channel geometric factors span over larger energy ranges for electrons than protons. Also, the tight spacing between D0 and D1 increases the FOV for electron detection. This explains why the maximum channel geometric factor is much larger when compared to protons. The larger FOV for electron detection may be beneficial to increase the sensitivity and acceptance cone angle for observing precursor electrons.

Overall, the Geant4 simulations show that P-SWEPT is able to measure electrons with energies ranging from 0.3 to 1.5 MeV, which is within the scientifically useful range for the electron flux preceding a SEP event and therefore can be used to produce early warning for the SEP proton flux. Further work is required to improve the energy identification resolution for electrons. Continuing to design P-SWEPT with the ability to measure electrons as a secondary goal to a direct measurement of SEP ions is a strategy to increase the scientific value to be gained from P-SWEPT through its flight on the Lunar Gateway, without significantly increasing the mass, volume, or design complexity.

4.3 P-SWEPT Dead Time Analysis

A detailed analysis taking energy-dependent proton count rates and the dead time function into account is performed to determine P-SWEPT's total dead time fraction during a 1-in-20 year worst case SEP proton flux. The dead time contribution due to electron flux during a SEP event is also investigated.

4.3.1 P-SWEPT Dead Time

The dead time of P-SWEPT is determined first by finding the differential count rate during the worst case particle flux P-SWEPT is expected to operate in. The differential proton count rate for a 1-in-20 year SEP event as predicted by the SAPPHIRE model (Jiggens et al., 2018) is shown in Figure 2.9. To find the energy-dependent count rates, an isotropic proton source is imposed on the P-SWEPT baseline geometry in Geant4. The set up for this isotropic simulation is identical to the set up used for the isotropic source simulations for LL-SWEPT, see Section 3.3.2 for more details. The equivalent isotropic dose per steradian generated from the sphere source can be found with Equation 3.1.

In the Geant4 simulation, proton energies ranged from 1 to 1000 MeV at a 1 MeV step size, with 100,000 protons at each energy step. A proton source is created in Geant4, although for the sake of the dead time analysis it is assumed that the generated proton source occurs every second, translating the proton source and amount of counts P-SWEPT measures into proton flux and count rate. Every proton event which deposits at least 0.05 MeV in any detector is recorded as a count. It is expected that only energy deposition events below 0.1 MeV would be indistinguishable from detector noise; however, the threshold is reduced to 0.05 MeV to be conservative for the dead time analysis. The number of counts per detector at each proton energy step (1 to 1000 MeV, 1 MeV proton energy step) are divided into the equivalent isotropic flux from the Geant4 proton sphere source (calculated using Equation 3.1) to find the energy-dependent geometric factor per detector. The energy-dependent geometric factor is then multiplied by the 1-in-20 year SEP event proton flux

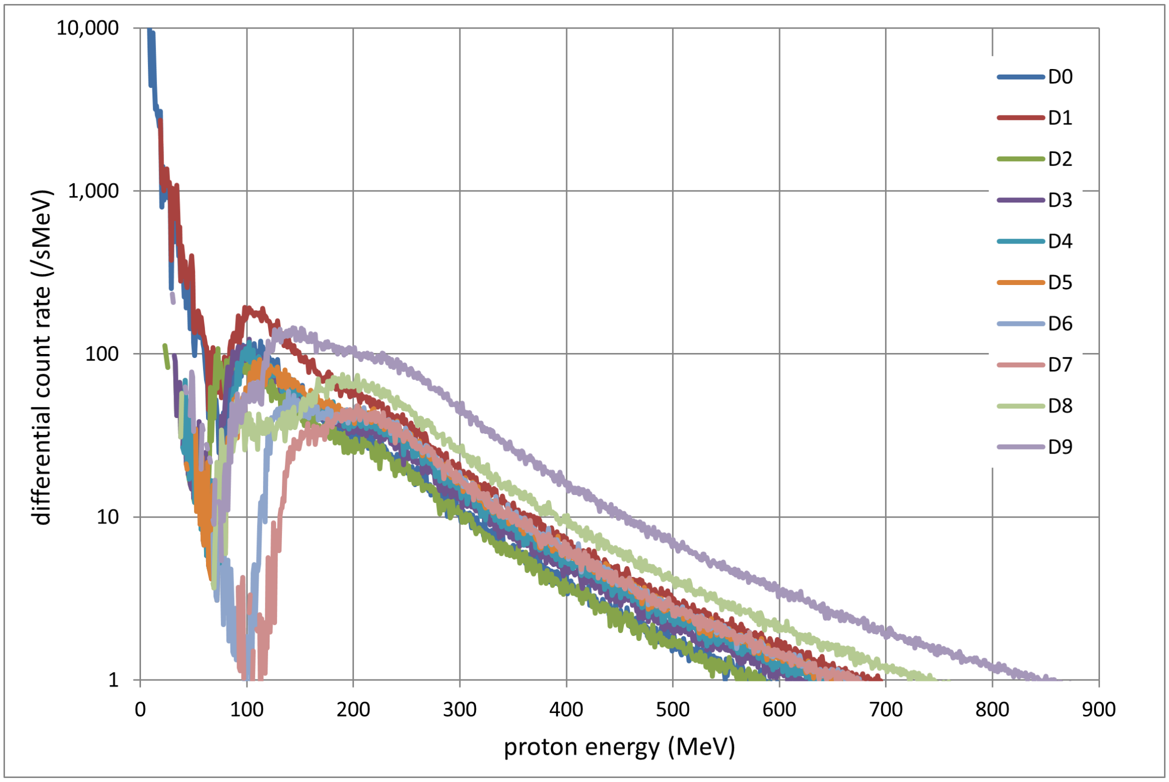

Figure 4.6: P-SWEPT's differential count rate for energy depositions > 0.05 MeV per detector from protons during a 1-in-20 year SEP event. See text for details. The data plotted is from an isotropic proton source simulation in Geant4.

at each proton energy step, shown in 2.9, to find P-SWEPT's differential count rate per detector, plotted in Figure 4.6.

A similar process is followed to find the differential dead time fraction. A histogram is created sorting the energy deposition events from the Geant4 isotropic simulation into bins with energies ranging from 0.05 to 20 MeV with a 0.2 MeV bin width. This provides the number of counts within discrete energy ranges per detector at each proton energy step.

A dead time function is required to assign each energy deposition value with a dead time. An impulse response function of the preamplifer electronics is used to determine how long the electronics take to process an energy deposition event of a given size. Figure 4.7 shows the impulse response function for a 2.5 MeV energy deposition event (left panel) and the rise and fall dead time for energy deposition events up to 40 MeV (right panel). Each energy deposition

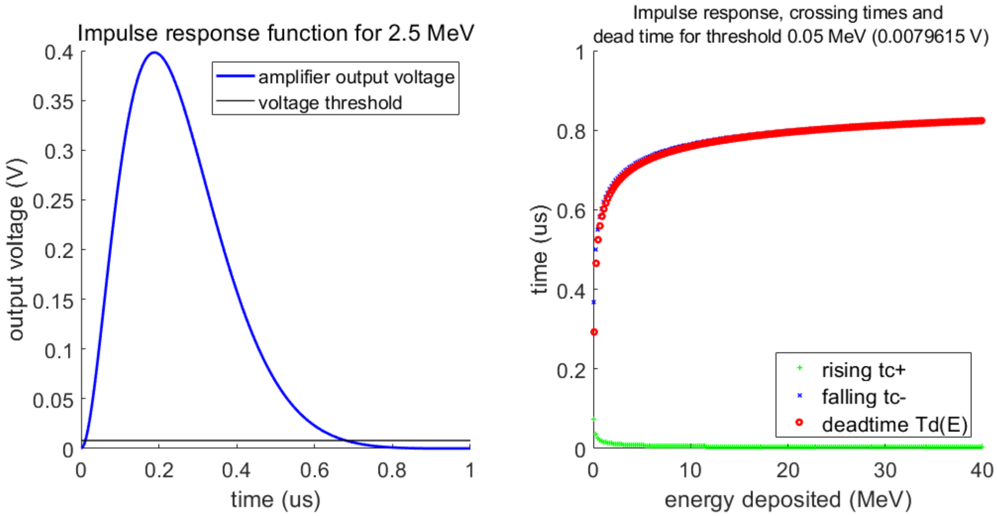

Figure 4.7: Left panel: P-SWEPT's representative electronics detector amplifier impulse response to a 2.5 MeV energy deposition, showing the 0.008 voltage threshold. Right panel: impulse response as a function of energy deposition, assuming a 0.008 V (0.05 MeV) cut off threshold.

event is assigned a dead time based on the time that the impulse response function remains above 0.008 V, corresponding to a 0.05 MeV cut off signal based on the detector calibration. The 0.05 MeV threshold is shown in the left plot of Figure 4.7. The impulse function is taken from the preamplifier electronics designs used in previous SWEPT contracts (H. Tiedje, personal communications, 2022). To be conservative, any energy deposition event above 20 MeV is assigned a dead time of 1 microsecond.

The dead time at each energy step is found by finding the dead time for energy deposition events from 0.05 to 20 MeV and multiplying it by the respective energy deposition frequency in the histogram. The result is the total dead time per detector at each proton energy step. Assuming the isotropic source modeled in Geant4 is the differential proton fluence per second, differential proton flux, the differential dead time (μs/MeV) can be equated to total dead time fraction (μs/s/MeV) and is plotted in Figure 4.8.

The dead time fraction per detector at each proton energy step is divided into the equivalent isotropic source imposed on the instrument at each proton energy step to find the dead time per detector from any one proton travelling in an isotropic source, or the dead time geometric factor. The dead time geo-

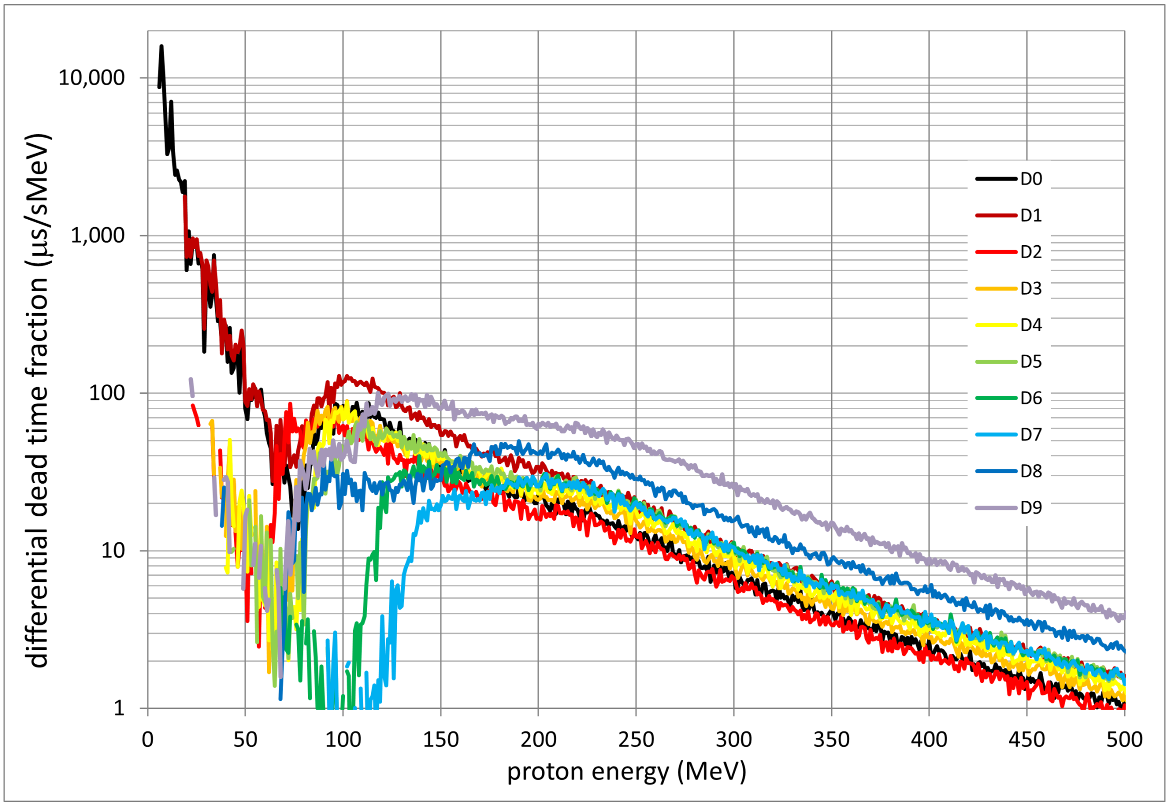

Figure 4.8: P-SWEPT differential dead time fraction during a 1-in-20 year SEP event flux per detector as a function of proton energy. The data plotted is from an isotropic proton source simulation in Geant4.

metric factor is multiplied by the 1-in-20 year SEP event flux at each proton energy step to determine the energy-dependent dead time fraction. This calculation is completed per detector. The differential dead time fractions are summed to obtain the integral dead time per detector, shown in Figure 4.9. Summing up the dead time in each detector gives a total dead time fraction due to protons, of 19.3 %

An identical process is completed to determine electron's dead time fraction contribution during a SEP event. The electron flux measured during the November 2001 SEP event is used as the expected electron flux incident on P-SWEPT, shown in Figure 2.8. Electrons add an additional 1.4 % to the total dead time fraction.

Figure 4.9 shows that detectors D0 and D1 have the largest dead times, which is expected as they sit directly behind the entrance cone and only 250 micron aluminum shielding. As mentioned in Section 3.3.3, 20 % dead time fraction is assumed to be the approximate upper limit in which a particle detector's performance is not significantly comprised. The assessed combined proton and electrons dead time fraction is just above the 20 % limit. The section below introduces a corrective measure which calculates a more accurate dead time fraction which brings the dead time below 20 %.

4.3.2 Dead time Correction Factor

The above analysis calculates the integrated dead time fraction under the assumption that no energy deposition events in any detector occur simultaneously. However, in most cases, particles deposit energy in multiple detectors as they travel through the instrument. The preamplifer response time is too long to resolve the time between separate energy deposition events and therefore are effectively measured to occur at the same time. Under the assumption that the instrument is not able to make accurate measurements when at least one detector is dead, there are many cases in which the dead time fraction is counting dead times of multiple detectors that occur at the same time. A dead time correction factor can be applied to the total worst case dead time to eliminate simultaneous energy deposition events from the summed dead time

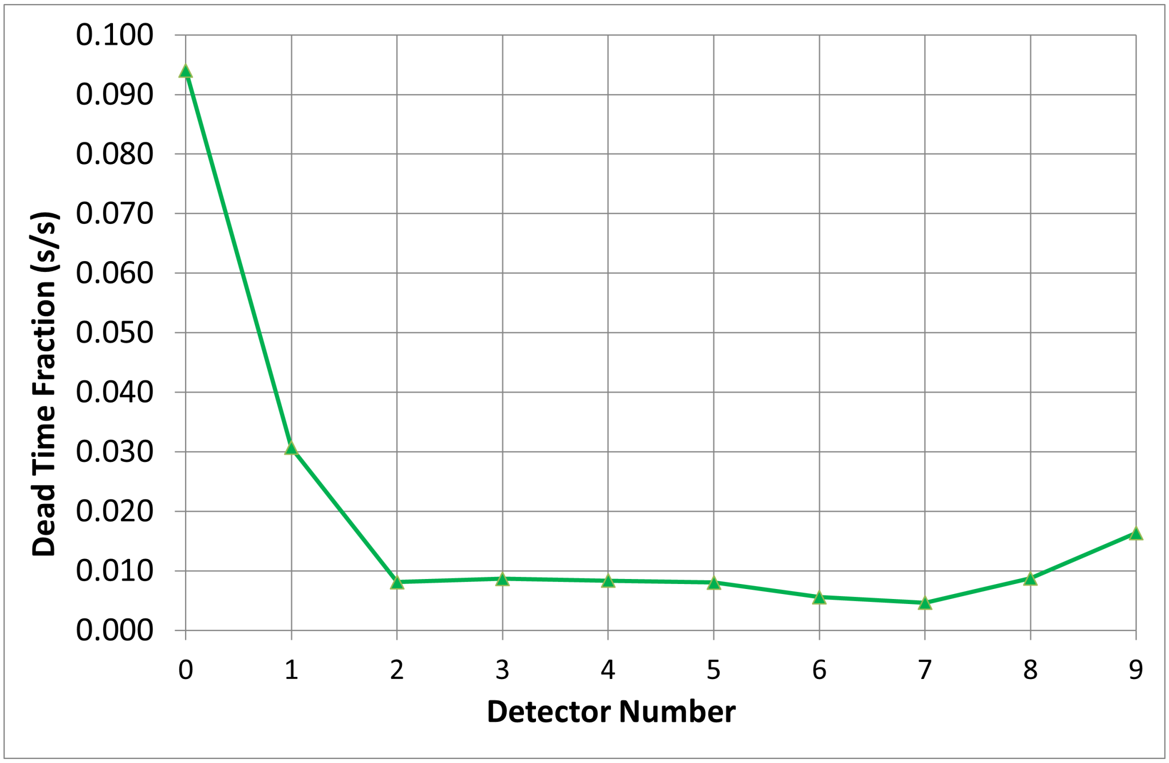

Figure 4.9: P-SWEPT integral (summed over 1 to 1000 MeV) dead time fraction from protons during a 1-in-20 year SEP event per detector as a function of detector number.

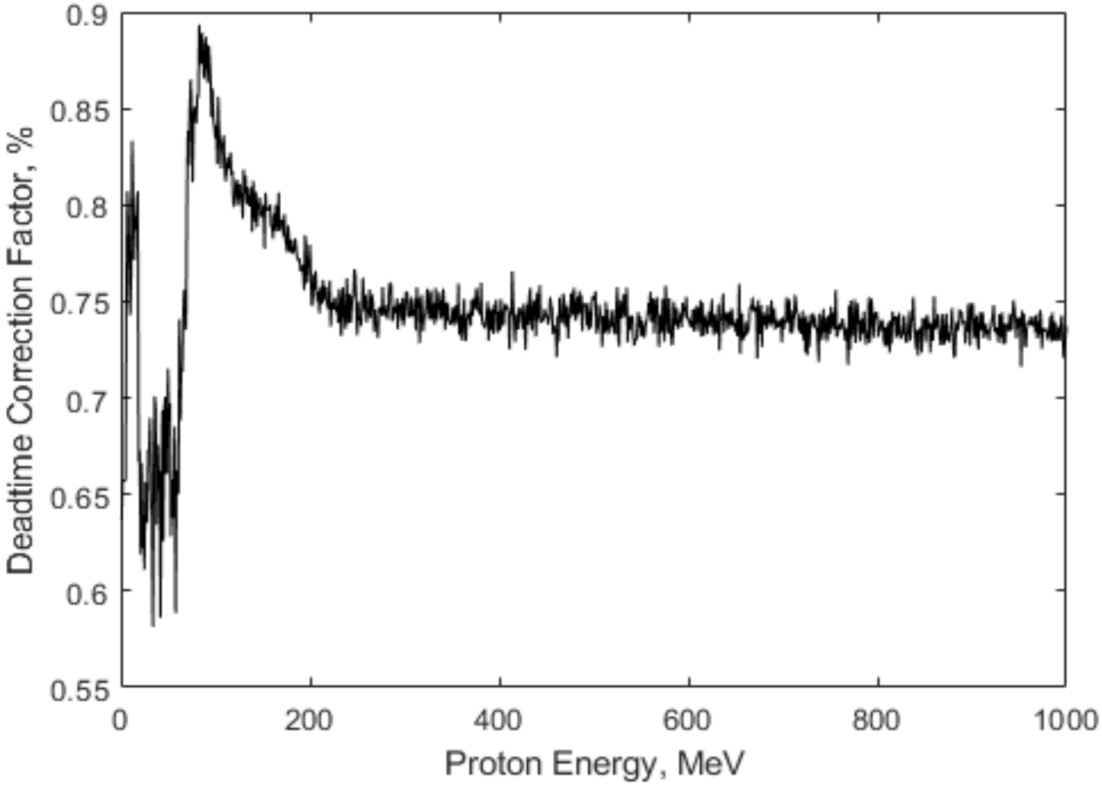

Figure 4.10: P-SWEPT's dead time correction factor as function of proton energy.

fraction. The number of proton events which one, two, three, four ... ten detectors recorded energy deposition events is determined for each energy step. Then, the following equation is used to determine the fractional dead time correction factor at a given energy:

$$\begin{aligned} Z &= \mathit{single\ energy\ deposition\ event} + \frac{\mathit{double\ energy\ deposition\ event}}{2} \ldots \\ &\quad + \frac{10\ \mathit{times\ energy\ deposition\ event}}{10} \end{aligned}$$

$$\mathit{Deadtime\ Correction\ Factor} = \frac{Z}{\mathit{Total\ number\ of\ energy\ deposition\ events}} \tag{4.1}$$

The energy dependant dead time correction factor is plotted in Figure 4.10 and ranges between 60 % to 90 %. The correction factor remains high until protons have enough energy to travel through detectors D0 and D1, around 20 MeV. The correction factor increases quickly at above 60 MeV, the energy in which protons are able to penetrate through P-SWEPT's side shielding. Protons which just penetrate the shielding are able to deposit energy into one detector, which increases the correction factor. As proton energy increases, the dead time fraction decreases and plateaus to about 73 %. At the high energies, both particles travelling through the shielding and through the entrance cone deposit energy in multiple detectors. After multiplying the differential dead time correction factor by the differential dead time and summing the dead time to each detector energy and detector, the total dead time fraction from protons is reduced from 19.3 % to 14.7 %, which is below the 20 % recommendation. The process is not completed on electrons due to their relatively low dead time fraction contribution.

This analysis also does not take other particle populations into account. Heavier ions will deposit more energy per unit length of material in the stack, which result in larger dead times. Future work includes modeling the other heavy particle populations found in SEP events simultaneously with protons and make any required changes to the instrument's shielding to keep the dead time fraction below 20 %.

4.3.3 P-SWEPT Summary and Future Work

On-axis and isotropic Geant4 simulations show P-SWEPT's geometry and energy identification algorithms are able to detect particles originating from solar and cosmic origins at the fluxes and energy ranges observable from the Lunar Gateway. P-SWEPT is able to make differential energetic proton measurements from 22 MeV up to 400 MeV, extending past the required proton energy range, 20 to 300 MeV. A detailed dead time analysis shows that P-SWEPT can continue to make scientifically useful measurements from the proton flux generated during a 1-in-20 year worst case SEP event. The dead time fraction contribution from electrons during a SEP event is small, and electron flux during a large SEP event increased the dead time fraction by less than 2 %. By verifying the energy dependant geometric factor from isotropic

Geant4 simulations over the measurable proton energy range, the coincidence logic along with the side and back shielding is sufficient to reject particles travelling off axis through the side of P-SWEPT. With a second detector behind the entrance cone, P-SWEPT is able to measure electrons with energies from 0.3 up to 1.5 MeV which can be used an early warning of the intensity and rise time of the dangerous proton flux which follows electron flux during a SEP event. A better understanding P-SWEPT's performance during large SEP events can be found by adding the heavier ions and neutrons present in GCR and SEP flux. Modelling P-SWEPT's gimbal mount, the relevant LOP-G structures, and P-SWEPT's structure in higher fidelity will provide more shielding than what is currently represented in the Geant4 model, and will further decrease dead time. Characterizing the noise in the silicon detectors to determine the minimum resolvable signal is required to verify P-SWEPT's measurable range. The addition of a Cerenkov detector to the backside of the instrument to increase the measurable energy range of the instrument is also currently being investigated.

Chapter 5

RADHEPT

As discussed in Chapter 2, the energetic particle telescopes for the RADiation Impacts on Climate and Atmospheric Loss Satellite (RADICALS) mission comprise of a lower (RADHEPT-LE) and higher energy (RADHEPT-HE) telescope. The RADHEPT instrument suite along with an X-ray imager, and fluxgate and search coil magnetometers, will work together to study the physical processes which control energetic particle precipitation into the atmosphere and its affect on Earth's climate. More information on the science requirements and background for RADICALS and RADHEPT can be found in Section 2.4.3.

In LEO, higher energy electrons (> 1 MeV) typically have orders of magnitude lower flux than the lower energy electrons in the ~ 100 to 1000 keV range. See e.g., Figure 2.12 in Section 2.4.3 for more details on the electron and proton populations expected at the RADICALS orbit. To accommodate this wide flux range, the RADHEPT instrument suite is separated into two detectors with different geometric factors. To resolve the relevant electron and proton population which are expected in the Van Allen Belts at LEO altitude, ≈ 600 km, RADHEPT is required to measure electrons with energies from 0.1 to 3 MeV, and protons with energies from 1 to 20 MeV, with a stretch goal to measure electrons up to 5 MeV and protons up to 40 MeV. The RADHEPT instrument suite is similar to LL-SWEPT and P-SWEPT as it relies on silicon detectors as its primary energy measurement technique. However, the layout of the instrument and anti-coincidence technique differ and are better optimized to detect the trapped and precipitating electron and proton populations in

LEO. Unlike P-SWEPT and LL-SWEPT, the RADHEPT instruments will not be on a gimbal mount to make angular resolved measurements. Instead, the RADICALS spacecraft has an approximately 30 second spin period which allows RADHEPT and the other instruments on board measure pitch angle resolved electron and ion flux data. The one second integration time provides an angular resolution of 12 °, sufficient to obtain pitch angle distributed data with an appropriate resolution to address RADICALS mission goals.

In this chapter, the design work and analysis completed on RADHEPT-HE and -LE instruments are reviewed separately. The design of RADHEPT-HE's entrance aperture and baffles are shown to be able to reject particles travelling off-axis through the side of the instrument. RADHEPT-HE's response to protons and electrons, and binning logic is also presented, along with a demonstration of an anti-coincidence scintillator to reject off-axis particles. A method to discriminate against lower energy electrons and protons that is integrated into the binning logic is presented. Similar to the following chapters, and Geant4 simulations are used to show the effectiveness of the detector geometry.

RADHEPT-LE has an identical entrance aperture geometry to RADHEPT-HE. The geometric factor for RADHEPT-LE is smaller and has less silicon detectors, to measure the higher flux, lower energy protons and electrons. Figure 2.12 shows the majority of electrons measured from POES-14 have energies below 800 keV. Like RADHEPT-HE, the geometric factor for RADHEPT-LE is chosen to be able to resolve the minimum required flux in an approximately one second integration time corresponding to an approximate 10 ° angular resolution for a 30 second spin period, while being capable of measuring the highest expected flux without saturating the detectors. RADHEPT-LE's binning logic is presented, along with its response to on-axis and isotropic electrons and protons. Two design considerations for RADHEPT-LE's enclosure are also presented: an anti-coincidence scintillator and tungsten shielding.

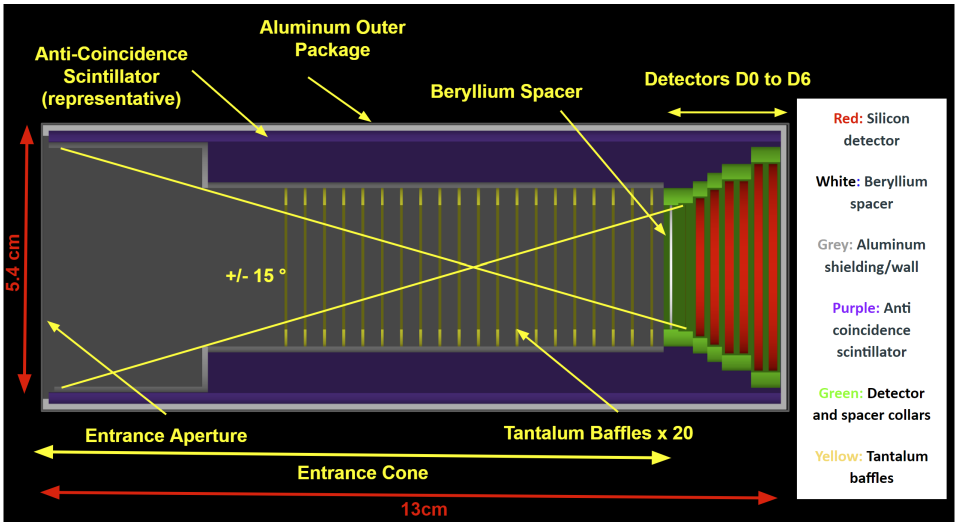

Figure 5.1: An annotated cross section of the baseline design for RADHEPT-HE as modeled in Geant4.

5.1 RADHEPT-HE

5.1.1 RADHEPT-HE Geometry

Figure 5.1 shows the baseline geometry of RADHEPT-HE. RADHEPT-HE's entrance cone is an aluminum tube, which steps down to a smaller tube lined with internal baffles and is designed to reject particles travelling outside the FOV from reaching the detector stack. The step between the entrance aperture and the baffle tube also help reject particles travelling off-axis through the FOV, see Figure 5.1. A 0.425 mm beryllium (Be) degrader in front of the detector stack prevents front incident electrons below 300 keV and protons below 7 MeV from reaching detector D0. This defines the low particle energy limits that RADHEPT-HE can measure. The detector radius and spacing between the detector stack and the opening in the entrance define its geometric factor.

RADHEPT-HE does not have a detector directly behind the entrance aperture like LL-SWEPT and P-SWEPT. Placing a coincidence detector directly behind the entrance aperture can significantly scatter electrons before they reach the back detector stack. Since RADHEPT-HE is primarily required to measure electrons, this method of using coincidence detection to improve the instrument's signal to noise is not feasible. To replace the front coincidence detector, the RADHEPT-HE detector stack is enclosed within a scintillator which will act as an anti-coincidence detector, detecting particles travelling off-axis through the side of the instrument. Any particle which deposits energy in both the scintillator and any subset of the seven silicon detectors in the stack will be rejected in the binning logic, and not sorted as a legitimate count into an energy channel. There is flight heritage and precedent for this approach, For example, particle detectors on board the Mission Demonstration Test Satellite 1 (MDS-1) (Matsumoto et al., 2001), Mars Science Laboratory, (Hassler et al., 2012), and the WIND Spacecraft (Lin et al., 1995) all utilized plastic scintillators as an anti-coincidence detection method.

In the analysis presented in this chapter using Geant4, the anti-coincidence scintillator is represented by an eighth, tube shaped detector which encloses the detector stack, see the purple anti-coincidences scintillator in Figure 5.1. Off-axis and side penetrating particles that deposit energy in the representative scintillator are identified in the Geant4 simulation and rejected, thus operating in a similar manner to an anti-coincidence scintillator. With this approach, significant side and back shielding are not needed to protect the detectors from particles travelling through the side of the instrument, as the anti-coincidence scintillator will be able to detect off-axis particles which travel through the instrument.

RADHEPT-HE will be mounted on the RADICALS spacecraft and will also benefit from the shielding of the spacecraft structure and other internal components. Once the layout of the spacecraft is finalized, adding shielding around the scintillator to ensure the dead time of the scintillator and detectors remains within an appropriate range can be revisited, optimized and added to the design. Tantalum baffles in the entrance tube help to prevent scattered and off-axis particles from travelling into the detector stack. Tantalum is used due to its high stopping power and relatively low secondary particle generation (e.g., Schiller et al., 2010).

RADHEPT-HE's detector D0 is thin as is is used to identify lower energy protons and electrons, see Section 5.1.3 for more information on the electron and proton discrimination. The radius of the detectors increases with detector number and progression further into the stack, to allow higher energy particles travelling through the entrance aperture at an angle inside the FOV to be successfully measured by the detectors deeper in the stack. The larger area back detectors also help when measuring higher energy particles which scatter as they travel through the previous detectors. The diameter and thickness of the detectors are available commercially off the shelf through Micron Semiconductor ("Micron Semiconductor Ltd. Silicon Catalouge Long Form," 2018).

RADHEPT's analog preamplifer and pulse shaper electronics are not represented in the Geant4 model used here. However, the mass of the electronics is expected to be similar to that on LL-SWEPT and P-SWEPT and is scaled to the number of silicon detectors within the instrument. Table 5.1 details the thicknesses of components and overall dimensions of RADHEPT-HE. However, the design and Geant4 analysis for the anti-coincidence scintillator and the associated photon detection electronics are outside the scope of this thesis. The entire instrument is enclosed in an outer aluminum package, for structural integrity. The dimensions of the structural and shielding members are estimated as the minimum to maintain structural integrity of the instrument. An estimated mass for RADHEPT-HE is shown in Table 5.2.

As mentioned in Section 2.3, the geometric factor determines the number of counts the instrument will measure when subjected to an isotropic particle source. To obtain sufficient angular resolution as RADICALS spins through its approximately 30 second spin period, RADHEPT-HE will have a one second integration time. This means that RADHEPT-HE must be able to measure at least one particle count per second to produce angular resolved measurements. Figure 2.12 in Section 2.4.3 shows that minimum integral electron flux (1st percentile) above energies >300 keV as measured by MEPED's 0 degree detector on-board POSE in LEO is 10 counts/s/cm^2/sr. Therefore, the minimum geometric factor to resolve 10 counts/s/cm^2/sr with a one second integration period (to count at least one particle over the integration time) is 0.1 cm^{2}sr. RADHEPT-HE's geometric factor is set to 0.2 cm^{2}sr to remain

Table 5.1: RADHEPT-HE's baseline geometry dimensions.

RADHEPT-HE's Subcomponent Geometry		
Parameter	Value	Unit
Number of Detectors	7	
Geometric Factor	0.2	cm^{2}sr
FOV (1/2 angle)	10	°
Entrance Cone Thickness (Aluminum)	1	mm
Scintillator Thickness (CBE)	2	mm
Outer Package Thickness (Aluminum)	1	mm
Detector Collar Thickness (PCB Material)	3	mm
Spacer Collar Thickness (PCB Material)	3	mm
RADHEPT-HE Overall Dimensions		
Width	5.4	cm
Length	13	cm

Table 5.2: RADHEPT-HE baseline geometry mass breakdown.

Mass	Value (kg)	% of Total Mass
Total Mass	1.93	
Scintillator Mass (CBE)	0.34	17.6%
Spacer Mass	0.05	2.6%
Detector Mass	0.17	8.8%
Baffle Ring Mass	0.20	10.4%
Entrance Cone Mass	0.22	11.4%
Package Mass	0.35	18.1%
PCB/electronics Mass (CBE)	0.60	31.1%

conservative, as electron count rate estimates are continuing to be refined from other satellite datasets. During the maximum worst case integral flux for electrons > 300 keV and protons above > 6900 keV will be subjected to 1.1×10^6 counts/s/cm^2/sr flux (See Figure 2.12 and Section 2.4.3 for more details). With a 0.2 cm^{2}sr geometric factor, the instrument is required to measure 220,000 cps, which is within the capabilities of current silicon detectors commercially available, and the baseline design of the RADHEPT electronics. The diameter of the entrance tube opening, and the distance between the opening and detector D0 define the geometric factor. The energy-dependent geometric factor is determined with isotropic particle simulations in Geant4, and is presented in Section 5.1.4 for protons and 5.1.5 for electrons.

Table 5.3: RADHEPT-HE detector material properties and thicknesses.

Detector Number	Silicon Detector Radius (cm)	Detector Thickness (mm)
0	1.08	0.02
1	1.20	1.50
2	1.35	1.50
3	1.50	1.50
4	1.50	1.50
5	1.80	1.50
6	1.80	1.50

5.1.2 RADHEPT-HE Entrance Design

As shown in Figure 5.1, the entrance cone of RADHEPT-HE is a tube with a single step, attached to a smaller tube lined with tantalum baffles. The entrance geometry defines the FOV of the instrument and is designed to block particles travelling through the entrance aperture outside the FOV from entering the detector stack. Particles travelling into the front of the entrnace aperture from outside the FOV may not travel through the anti-coincidence scintillator and would be impossible to discriminate from particles travelling through the FOV, and will be misidentified as such. Geant4 simulations are used to assess this to seek to optimize the design of the RADHEPT instrument.

Specifically, Geant4 simulations were performed to determine the extent to which the entrance design off-axis particles from travelling to reach detector D1 without depositing energy in the anti-coincidence scintillator. The low mass electrons are consistently pushed off course as they interact with free conductance electrons of equal mass in the silicon detector and shielding (e.g., Stacy and Vestrand, 2003). Protons are able to travel through matter in a more ballistic fashion and experience less scattering. Therefore, an excess of particles travelling through the entrance with angles outside the FOV which scatter into the detectors is an issue primarily for electrons. In the Geant4 simulations, electrons from a disc source are shot forward, at the front of RADHEPT-HE, directed at the centre of the front entrance opening. The disc source has a diameter of 3.7 cm, the same diameter as the entrance aperture of RADHEPT-HE, large enough to completely flood the entrance aperture with

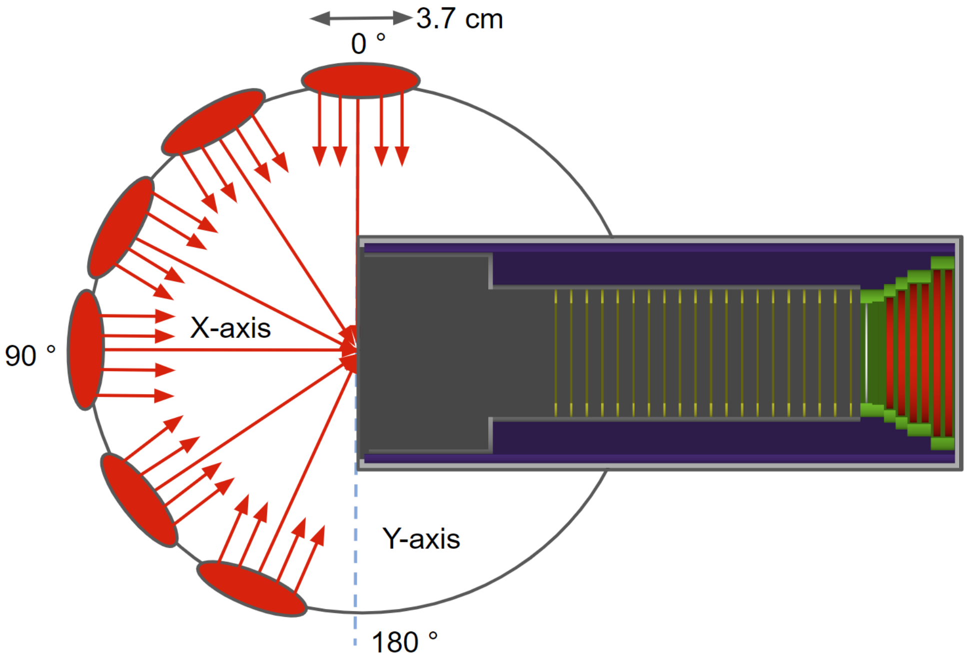

Figure 5.2: A schematic showing the cross section of RADHEPT-HE and the angled disc source Geant4 simulation set-up.

incident electrons. The disc source is shot at the entrance aperture at angles ranging from +/- 90 ° from the long axis of the instrument. 100,000, 0.5 MeV energy electrons are released at each angle from a 20 cm distance from the front entrance, and the angle between the disc source and the instrument's long axis increases by 0.573 radians each step. This particle pattern simulates an isotropic source incident only on the front entrance from one hemisphere. Figure 5.2 shows a schematic of the Geant4 simulation setup. Before the simulation data is plotted, all electron events are run through RADHEPT-HE's electron binning logic, presented in Table 5.6, and only electrons sorted into an energy channel are plotted. See Section 5.1.5 for details on the electron binning regime. The plots in Figure 5.3 show the number of 0.5 MeV electrons sorted into each electron energy channel against the disc source angle relative to vertical.

Figure 2.12 in Section 2.4.3 shows the maximum ratio between the 90° and 0° detectors, for the POES MEPED instrument, and which are generally representative of the trapped and precipitating electron populations, to be 10,000. While measuring electrons inside the loss cone, trapped electrons with pitch angles outside the RADHEPT-HE's FOV and which are scattered such a way that they travel through the front entrance could be misidentified as precipitating electrons if they are not sufficiently blocked. To ensure RADHEPT-HE measures the correct particle population while rotating through areas inside and outside the loss cone, RADHEPT-HE must be able to reject off-axis particles travelling through the aperture by more than 99.99 %, or 1 in 10,000.

The left panel of Figure 5.3 shows that the entrance aperture successfully rejects 99.99 % of off-axis 0.5 MeV energy electrons up to incident angles of about +/- 35 ° from the instrument's long axis. Table 5.4 shows the number of off-axis 1 MeV and 3 MeV energy electrons at select angles relative to vertical, that are sorted into energy channels. The entrance cone becomes less effective at rejecting off-axis electrons at higher energies, exceeding the 99.99 % rejection rate for angles +/- 30 ° from the long axis. The right plot of Figure 5.3 shows that the FOV of RADHEPT-HE is around 16 ° (FWHM), small enough to allow the RADHEPT-HE to make angular resolved measurements during a RADICALS spin period. When the disc source is directly in front of the front entrance (90 ° relative to vertical), just under 30 % of the electrons from the disc source are sorted into an electron energy channel. This is largely because the disc source has a diameter of 3.7 cm, larger in area than detector D0 with a diameter of 2.2 cm.

Given the current level of preliminary design of the RADHEPT instrument, these simulation results are considered acceptable performance both in count rates and side penetrating particle rejection as a first iteration of the baffle and entrance cone design. Future work includes optimizing the geometry, material and coating of the baffles to ensure the entire electron energy measurement

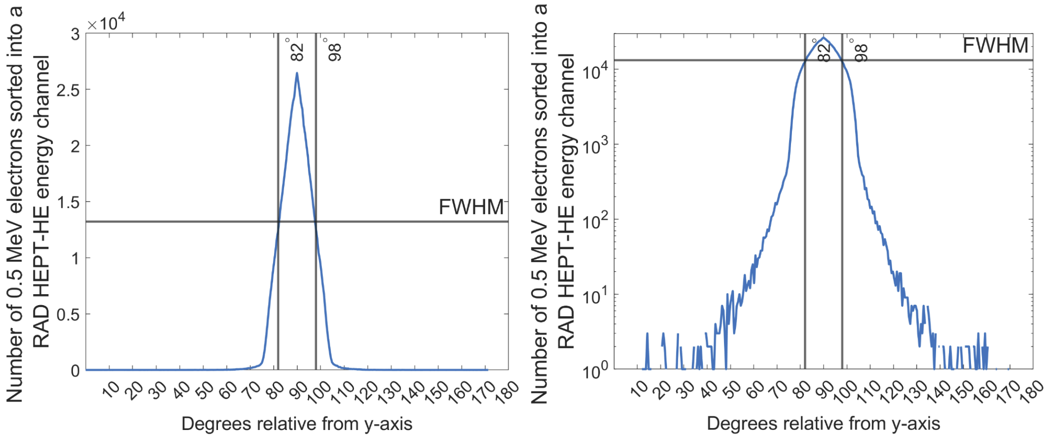

Figure 5.3: Number of 0.5 MeV electrons from a disc source, R = 1.84 cm, travelling through the centre of RADHEPT-HE's entrance aperture sorted into an electron energy channel as a function of disc source angle, relative to vertical. The right panel's y-axis is logarithmically scaled, and the left plot is linearly scaled. See the text and Figure 5.2 for details of the Geant4 simulation set up.

Table 5.4: Number of electrons with energies 1.0 and 3.0 MeV sorted into electron energy channels from a disc source with a radius of 1.84 cm at select angles relative to vertical, travelling through RADHEPT-HE's front entrance, simulated in Geant4.

Angle relative to vertical (Y-axis)	Number of electrons sorted into an energy channel travelling at select angles, out of 1,000,000 electrons	
	1.0 MeV	3.0 MeV
45 °	70	53
60 °	310	521
120 °	370	615
135 °	50	52

range of RADHEPT-HE has a rejection ratio of 99.99 % for electrons outside the FOV travelling through the front entrance.

5.1.3 Electron and Proton Discrimination

RADHEPT-HE is designed to measure both proton and electron populations simultaneously. P-SWEPT also has this ability (see Section 4.2 for more details), however P-SWEPT is limited to measuring electrons energies up to 1.5 MeV with signals deposited in its detectors D0 and D1, positioned directly behind its entrance cone. This causes the FOV and geometric factor for P-SWEPT's electron detection to be much larger than that for its proton detection. P-SWEPT measures the proton energy with the back detector stack exclusively, using the energy deposition signals in its detectors D1 and D2 as a proton coincidence detection method only. RADHEPT-HE, however, requires the simultaneous detection of angulary resolved electrons and protons with the same FOV.

As shown in Figure 5.1, all of RADHEPT-HE's detectors sit in the back of the instrument. Electrons and protons are measured with the same detector stack. With this detector layout, it is impossible to identify and separate the species for lower energy electrons and protons which deposit energy in only detector D0. These particles would be sorted into the lower energy channels as both protons and electrons.

However, protons have a much higher stopping power than electrons, meaning they will deposit more energy into the detectors per unit length. More details on energy deposition in silicon detectors can be found in Section 2.1.1. The difference in stopping power between electrons and protons can be used to differentiate between them as they travel through RADHEPT-HE's 20 micron thick detector D0. Virtually all particles which don't stop in the beryllium degrader will also travel through the D0 without stopping. Protons will deposit more than 100 keV into D0, with electrons depositing much less energy due to their relatively low stopping power. Based on the current design, the electron's energy deposition in D0 will be low enough to be undetectable from the noise of the detector. The signal from D0 can therefore be used as a proton identifier; only particles which deposit more than 100 keV in D0, and no energy in detectors D3 to D7 are sorted into the lowest proton channel (8 to 10 MeV). The proton coincidence is only required for low energy protons, so the check will only be applied to those sorted into the lowest energy proton bin. Higher energy protons are easily identifiable by their energy deposition in successive detectors deeper in the stack. When this proton identifier check is applied to the electron and proton binning logic, a negligible amount of particles are misidentified as the wrong species. For example, when 100,000 electrons ranging from 0.01 to 10 MeV (0.01 MeV step size, 100 electrons per step) are generated as a pencil beam through the entrance aperture of RADHEPT-HE in Geant4 and sorted with the proton binning logic, 38 of the electrons (0.038 %) were sorted into a proton channel. When 100,000 protons ranging from 0.1 to 100 MeV (0.1 step size, 100 protons per step) were generated as a pencil beam through the front entrance of RADHEPT-HE in Geant4 and sorted with the proton binning logic, 1 proton (0.001 %) was sorted into an electron channel. The proton coincidence has therefore been integrated into the RADHEPT-HE proton and electron binning logic, see Sections 5.1.4 and 5.2.2 respectively.

5.1.4 RADHEPT-HE Proton Response

The top panel of Figure 5.4 shows the average energy deposition as a function of proton energy in RADHEPT-HE's seven silicon detectors. For each event, the energy deposited into each detector is summed. The summed energy deposition, along with the number of detectors where energy is deposited and the amount of energy the proton deposits in each, and the proton coincidence logic (see the section above for details), are used to sort into the protons into energy channels. Only energy depositions above 100 keV are considered as true counts, any signal below 100 keV would most likely be unidentifiable above the noise of the detectors. See Table 5.5 for the RADHEPT-HE proton binning conditions for each energy channel. The energy channel widths give an energy resolution of +/- 1 MeV, and are set to minimize binning resolution while maximizing binning efficiency.

A Geant4 simulation shooting a pencil beam of protons with energies from 1 to 100 MeV with a 0.1 MeV step size at 1000 protons per step through the centre of RADHEPT-HE's FOV is completed. The top panel of Figure 5.4 shows the average proton energy deposition in each detector as a function of proton energy. The bottom panel of Figure 5.4 shows the proton binning efficiency into the energy bins up to energies of 70 MeV. The current detector number, geometry, and binning logic is able to detect protons up to 70 MeV, well above RADHEPT-HE's required upper energy range required of 20 MeV. RADHEPT-HE does not require proton measurements with energies up to 70 MeV. However it is able to do so with its seven detectors. All seven detectors are required to measure electrons with energies up to 4.4 MeV which approaches RADHEPT's electron measurement goal of 5 MeV. See Section 5.1.5 for more information on electron identification.

Note that the last five energy channels in Figure 5.4 have more gradual thresholds compared to the lower energy channels. These energy bins are defined by the gradual decrease in the summed energy deposition once the protons travel through the entire energy stack without stopping, see the black curve ($x = \geq 42$ MeV) in the top panel of Figure 5.4. The summed energy does not decrease as steeply as it increases, causing the energy channel threshold to be less well defined.

An isotropic flux source, with a Geant4 simulation set up identically to the one described in Section 3.3.2, is completed for RADHEPT-HE. Protons with energies from 7 to 75 MeV with a 0.5 MeV step size and 1,000,000 particles per step are simulated. Figure 5.5 shows RADHEPT-HE's energy-dependent geometric factor. Figure 5.5 shows that the geometric factor remains around the expected value of 0.2 cm^2sr for energies from 7 to 70 MeV.

As mentioned previously, RADHEPT-HE will be mounted on the RADICALS spacecraft, so the spacecraft structure and other components are expected to provide some back shielding. This shielding will likely solve the problem of backward penetrating particles, and based on the current assessment we conclude that no further data processing needs to be put in place. Additionally, the current baseline geometry of RADHEPT-HE measures pro-

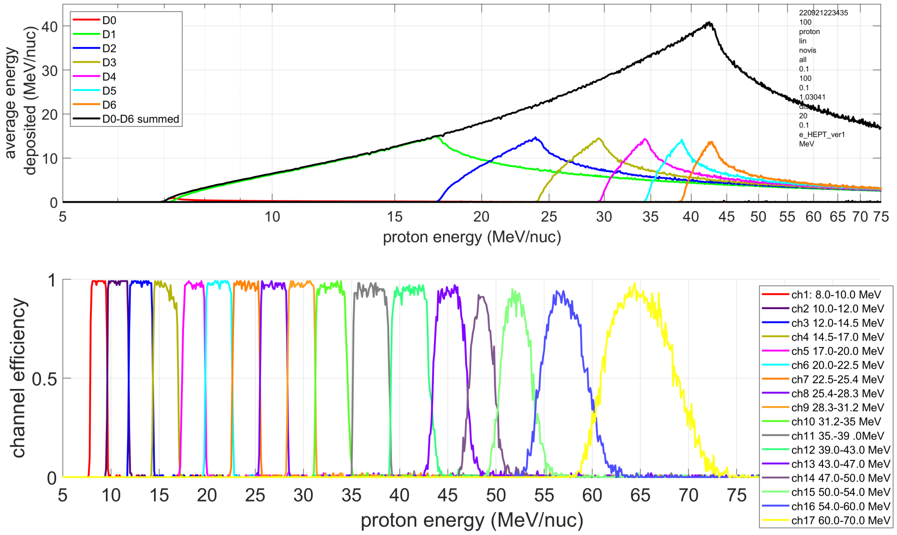

Figure 5.4: Geant4 simulations of the RADHEPT-HE proton response. Top panel: Average energy deposition as a function of electron energy for each detector element RADHEPT-HE for a proton beam travelling through the centre of RADHEPT-HE's entrance aperture in Geant4. Bottom panel: Binning efficiency for a proton beam travelling through the centre of RADHEPT-HE's entrance aperture sorted using the channel binning logic in Table 5.5.

Table 5.5: RADHEPT-HE proton energy binning logic.

Energy channel Number	Energy channel range (MeV)	Min. summed energy deposition (MeV)	Max. summed energy deposition (MeV)	Other conditions (keV)
1	8.0-10.0	1	3	D0-D1 >100, D2-D6 <100
2	10.0-12.0	3	6	D0-D1 >100, D2-D6 <100
3	12.0-14.5	6	9	D0-D1 >100, D2-D6 <100
4	14.5-17.0	9	12	D0-D1 >100, D2-D6 <100
5	17.0-20.0	12	15	D0-D1 >100, D2-D6 <100
6	20.0-22.5	15	18	D0-D2 >1000, D3-D6 <100
7	22.5-25.4	18	21	D0-D2 >100, D3-D6 <100
8	25.4-28.3	21	24	D0-D2 >100, D3, D5-D6 <100
9	28.3-31.2	24	27	D0-D3 >100, D4-D6 <100
10	31.2-35.0	27	30	D0-D3 >100, D5-D6 <100
11	35.0-39.0	30	34	D0-D4 >100, D5-D6 <100
12	39.0-43.0	34	38	D0-D5 >100, D6 <100
13	43.0-47.0	38	42	D0-D4, D6 >100, D5 >700
14	47.0-50.0	30	27	D0-D5 >100, D6 >700
15	50.0-54.0	27	24	D0-D5 >100, 585 <D6 <719
16	54.0-60.0	24	21	D0-D5 >100, 490 <D6 <585
17	60.0-70.0	21	18	D0-D5 >100, 410 <D6 <490

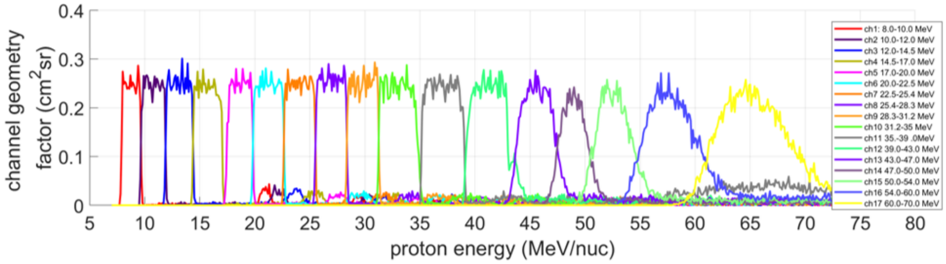

Figure 5.5: Geant4 simulations of the RADHEPT-HE proton response to an isotropic proton source. RADHEPT-HE's energy-dependent geometric factor per energy channel as a function of proton energy. The data plotted is from an isotropic proton source simulated in Geant4.

tons well above the stretch measurement goal for protons, 40 MeV. If the shielding from the spacecraft does not sufficiently protect the backside of the instrument from higher energy protons, then the slope check algorithm used on LL-SWEPT and P-SWEPT proton data analysis (see Section 3.4 for more details) can be integrated into the RADHEPT-HE energy identification regime.

5.1.5 RADHEPT-HE Electron Response

The Geant4 simulations used to determine the on-axis electron response for RADHEPT-HE consist of an electron beam with energies from 0.01 to 6 MeV, in 0.01 MeV steps, and with 1000 electrons per step travelling directly on-axis of RADHEPT-HE. The top panel of Figure 5.6 shows the average energy deposition as a function of electron energy per detector. As shown in Figure 5.6, there is very little average energy deposition in detector D0. Any significant (100 keV or larger) energy deposition in this detector classifies the particle as a proton. See Section 5.1.3 for more details on the use of the D0 for electron and proton discrimination.

Table 5.6 shows the parameters for sorting electrons into each energy channel, plotted in Figure 5.6. Like the protons, the summed energy deposition in all seven detectors is used to assign each electron with to an energy channel. The number of detectors the electron deposits energy into is also considered in the binning logic. The width of the energy bins is determined by trading off channel resolution and efficiency. After the summed energy deposition

Table 5.6: RADHEPT-HE electron binning logic.

Energy channel number	Energy channel range (MeV)	Min. summed energy deposition (MeV)	Max. summed energy deposition (MeV)	Other conditions (keV)
1	0.3-0.5	0.1	0.4	D0 <100, D1 >100, D2-D6<100
2	0.5-0.8	0.4	0.7	D0 <100, D1 >100, D2-D6 <100
3	0.8-1.1	0.7	1.0	D0 <100, D1 >100, D2-D6 <100
4	1.1-1.4	1.0	1.3	D0 <100, D1 >100, D3-D6 <100
5	1.4-1.7	1.3	1.6	D0 <100, D1 >100, D3-D6 <100
6	1.7-2.0	1.6	1.9	D0 <100, D1 >100, D4-D6 <100
7	2.0-2.3	1.9	2.2	D0 <100, D1-D2 >100, D4-D6 <100
8	2.3-2.6	2.2	2.5	D0 <100, D1-D2 >100, D5-D6 <100
9	2.6-2.9	2.5	2.8	D0 <100, D1-D2 >100, D5-D6 <100
10	2.9-3.2	2.8	3.1	D0 <100, D1-D2 >100, D5-D6 <100
11	3.2-3.5	3.1	3.4	D0 <100, D1-D3 >100, D6 <100
12	3.5-3.8	3.4	3.7	D0 <100, D1-D3 >100, D6 <100
13	3.8-4.1	3.7	4.0	D0 <100, D1-D3 >100, D6 <100
14	4.1-4.4	4.0	4.3	D0 <100, D1-D3 >100, D6 <100
15	>4.4	2.0	10.0	D0 <100, D1-D6 >100

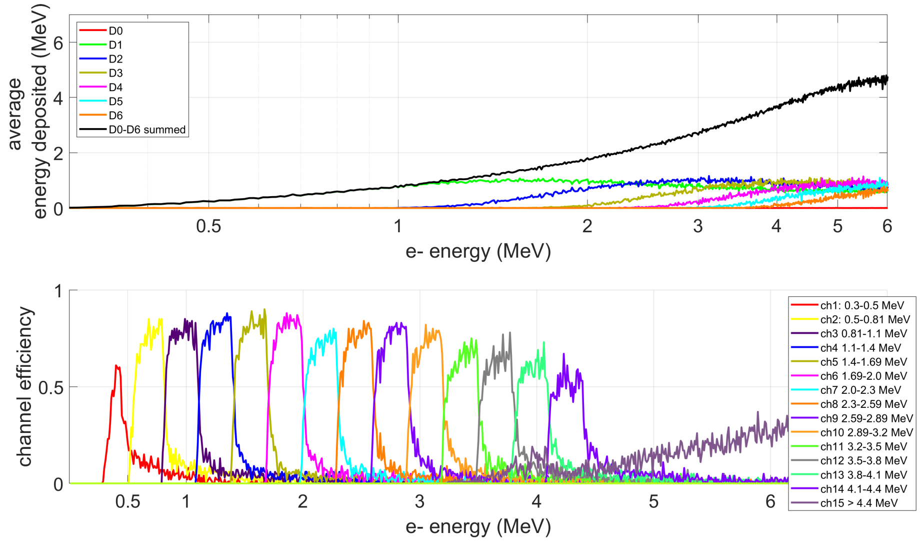

Figure 5.6: Geant4 simulations of the RADHEPT-HE electron response. Top panel: Average energy deposition as a function of electron energy for each detector element of RADHEPT-HE for an electron pencil beam travelling through the centre of RADHEPT-HE's entrance aperture in Geant4. Bottom panel: Binning efficiency for an electron pencil beam travelling through the centre of RADHEPT-HE's entrance aperture sorted using the channel binning logic in Table 5.6. The black curve on the top plot of is the sum of energy depositions for all seven detectors.

reaches a maximum (4.4 MeV, see black curve on the top panel of Figure 5.6), the summed energy deposition does not decrease as steeply as the protons. Therefore the summed energy deposition cannot be used to identify electrons with energies above 4.4 MeV with any reasonable binning resolution. Instead of creating higher energy bins, an integral bin measures electrons with energies $>$ 4.4 MeV. Regardless, RADHEPT-HE's baseline geometry is still able to measure well over the RADHEPT's 3 MeV electron measurement requirement, and close to the 5 MeV measurement goal.

A Geant4 simulation is run to determine RADHEPT-HE's energy-dependent geometric factor for electrons. The Geant4 isotropic simulation set up is similar to that presented in Section 3.3.2, except electrons with energies from 0.1 to 6 MeV with a 0.05 MeV step size at 1,000,000 electrons per step is simulated. Figure 5.7 shows RADHEPT-HE's energy-dependent geometric factor for electrons. Figure 5.7 shows, as expected, that the channel specific geometric factor remains around 0.2 cm^2sr until 3.8 MeV and begins to decrease until the last integral channel ($>$4.4 MeV, in Figure 5.7). This aligns with the reduction in on-axis channel efficiency for electrons with energies $>$3.5 MeV energy electrons, see Figure 5.6. After about 5 MeV, electrons travelling either through the front aperture or through the backside of RADHEPT-HE consistently travel through all seven detectors and are indistinguishable. Forward and backward travelling electrons are counted in the integral channel. When compared to protons the electron channel geometric factor thresholds are less defined. Figure 5.7 shows the geometric factor curves bleeding into larger energies than the expected maximum energy threshold as defined in the legend on the right side of Figure 5.6. This is similar to the results from the pencil beam on-axis irradiation shown in Figure 5.6. Due to their relatively low momentum, electrons can scatter to positions outside the detector area, thereby depositing less than their total energy into the stack and causing them to be sorted into a lower energy channel. With the geometric factor well-characterized for an isotropic source, the count rates measured by RADHEPT-HE could be corrected to account for this effect using the exact instrument response function in post-processing. Regardless, the energy-dependent channel geometric fac-

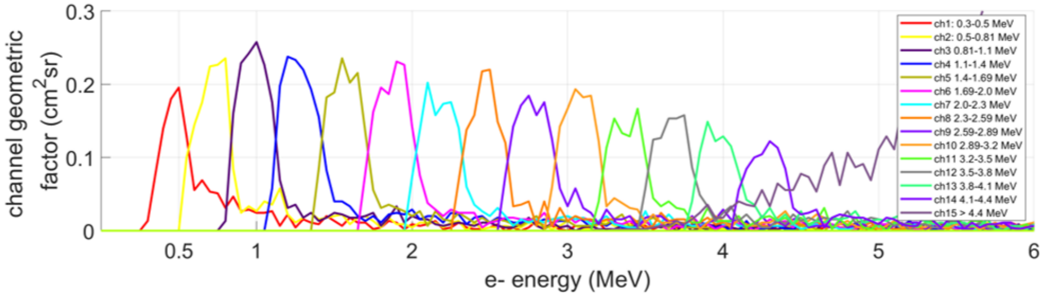

Figure 5.7: Geant4 simulations of the RADHEPT-HE electron response to an isotropic source. RADHEPT-HE's energy-dependent geometric factor per energy channel as a function of electron energy. The data plotted is from an isotropic electron source simulated in Geant4.

tor shows that the preliminary design and binning logic for RADHEPT-HE is able to measure electrons with energies from 0.3 to 4.4 MeV, with sufficient binning efficiency and resolution to support the RADHEPT-HE science objectives. The next steps for the RADHEPT-HE development are outlined in Section 5.3.

5.2 RADHEPT-LE

5.2.1 RADHEPT-LE Geometry

The schematic in Figure 5.8 shows the preliminary baseline geometry of RADHEPT-LE. RADHEPT-LE's entrance cone is identical to RADHEPT-HE, but the entire instrument is scaled down in size from RADHEPT-HE to fit RADHEPT-LE's detector sizes. Two options to protect the detectors from side penetrating particles are being considered: an anti-coincidence scintillator, identical to RADHEPT-HE, or 0.5 cm of tungsten shielding placed around the entire instrument, as shown in Figure 5.8. The shielding is the simplest option, and RADHEPT-LE is small enough that the relatively thick shielding does not introduce significant additional mass. However, the shielding is only able to block particles up to a certain energy thresholds, after which RADHEPT-LE will not be able to distinguish between side penetrating higher energy particles and lower energy ones travelling through the entrance cone. The scintillator would be able to identify all side penetrating particles, but may add unnec-

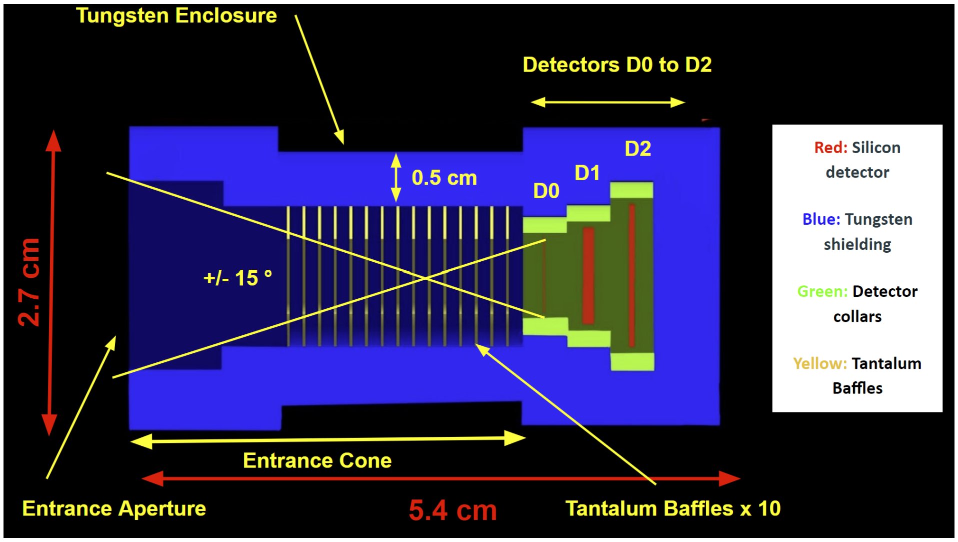

Figure 5.8: An annotated cross section of RADHEPT-LE, with a tungsten shielding enclosure, as modeled in Geant4.

essary complexity to the design, especially considering the relatively low flux expected for high energy particles which are able to penetrate the shielding. Additionally, RADHEPT-LE will be mounted on the RADICALS spacecraft and will partially benefit from the shielding of the spacecraft structure and other internal components. Once the layout of the spacecraft is finalized and the expected electron and proton count flux estimates are refined, a decision on RADHEPT-LE's enclosure can be made. Geant4 isotropic simulations showing RADHEPT-LE's response with thick shielding and an anti-coincidence scintillator are shown for comparison in Section 5.2.3.

RADHEPT-LE's thin detector D0 is used to accurately identify lower energy protons and electrons similarly to RADHEPT-HE, see Section 5.1.3 for details on this design feature. RADHEPT-LE's detectors have a much smaller area than RADHEPT-HE, therefore the expected noise levels in the detector elements will be lower than those for RADHEPT-HE. It is assumed that any signal below 40 keV will not be distinguishable from the noise in the detectors, which defines the lower energy limit that can be used in the channel logic tables for RADHEPT-LE. The radius of the detectors in RADHEPT-LE also increases with detector number, to allow higher energy particles travelling through the aperture along the inside of the entrance cone to be successfully measured by the detectors deeper in the stack. The larger area back detector ensures that higher energy particles which scatter as they travel through the previous detectors are still sufficiently counted. The diameter and thickness of the detectors chosen for elements in the stack are available commercially off the shelf through Micron Semiconductor ("Micron Semiconductor Ltd. Silicon Catalouge Long Form," 2018). In front of detector D0, a thin (15 micron) aluminum foil protects blocks light from entering the detector stack.

The count rates of electrons and protons in the energy range of RADHEPT-LE spans six orders of magnitude, from 10 to 1×10^7 counts/s/cm^2/sr. RADHEPT-LE's geometric factor is set to 0.02 cm^{2}sr, to be able to measure particles flux as low as 50 counts/s/cm^2/sr during a one second integration time. In a 1×10^7 counts/s/cm^2/sr flux, the instrument will be required to count at 200,000 cps without saturating, which is approximately within the capabilities of the silicon detectors commercially available and of the RADHEPT readout electronics. As the expected minimum count rate continues to be refined, the geometric factor can be modified to prioritize lower count rates if needed.

With the 0.5 cm tungsten shielding, RADHEPT-LE has a 2.7 cm by 2.7 cm by 5.4 cm volume envelope and has a mass of 0.663 kg. With the anti-coincidence scintillator, RADHEPT-LE has a 2.2 cm by 2.2 cm by 5.0 cm volume envelope and has an estimated mass of 0.370 kg. Tables 5.7 and 5.8 show the size and mass current best estimate breakdowns of the RADHEPT-LE geometry with the tungsten shielding enclosure. Table 5.9 shows the dimensions and thicknesses of RADHEPT-LE's three detectors.

5.2.2 RADHEPT-LE Proton Response

The top panel of Figure 5.9 shows the average energy deposition as a function of proton energy in RADHEPT-LE's three silicon detectors as simulated in Geant4. As explained earlier, protons which deposit at least 100 keV in detector D0 are sorted into the RADHEPT-HE proton binning logic. The protons are then sorted into an energy channel based on their energy deposition in D1. See Table 5.10 for the RADHEPT-LE proton binning logic for each energy channel. The energy channel widths minimize binning resolution while

Table 5.7: RADHEPT-LE's baseline geometry dimensions, with tungsten shielding.

RADHEPT-LE's Subcomponent Geometry		
Parameter	Value	Unit
Number of Detectors	3	
Geometric Factor	0.02	$\mathrm{cm}^2\mathrm{sr}$
FOV (1/2 angle)	10	°
Entrance Cone Thickness (Tungsten)	1	mm
Side Shielding Thickness (minimum thickness) (Tungsten)	5	mm
Detector Collar Thickness (PCB Material)	3	mm
Back Shielding Thickness (Tungsten)	5	mm
RADHEPT-LE Overall Dimensions		
Width	5.4	cm
Length	13	cm

Table 5.8: RADHEPT-LE baseline geometry mass breakdown, with tungsten shielding.

Mass	Value (kg)	% of Total Mass
Total Mass	0.66	
Detector Mass	0.01	1.5%
Detector Collar Mass	0.01	1.5%
Baffle Ring Mass	0.05	7.6%
Tungsten Enclosure Mass	0.39	59.1%
PCB/electronics Mass (CBE)	0.20	30.2%

Table 5.9: RADHEPT-LE detector sizes and thicknesses.

Detector Number	Detector Radius (cm)	Detector Thickness (mm)
0	0.34	0.02
1	0.45	1.0
2	0.66	0.5

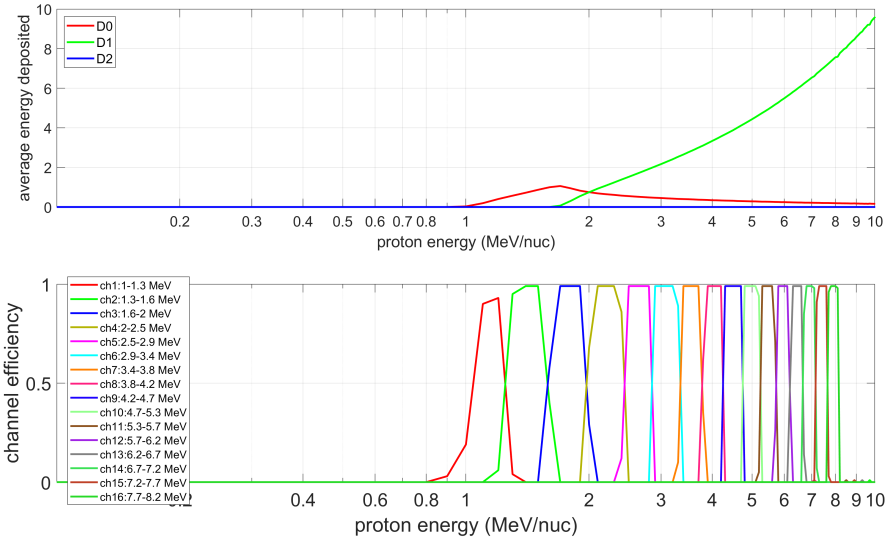

Figure 5.9: Geant4 simulations of the RADHEPT-LE proton response. Top panel: RADHEPT-LE's average energy deposition from a proton pencil beam incident on-axis through RADHEPT-LE's aperture in as simulated in Geant4. Bottom panel: Binning efficiency for on-axis protons sorted using the channel binning logic in Table 5.10.

maximizing binning efficiency. A Geant4 simulation shooting a pencil beam of protons with energies 1 to 10 MeV with a 0.1 MeV step size at 1000 protons per step through the centre of RADHEPT-LE's FOV is completed to determine the binning efficiency. RADHEPT-LE is required to measure protons with energies only up to 8 MeV, while RADHEPT-HE measures the rest of the required energy range. Protons with energies beyond 8 MeV stop inside detector D1, so particles which deposit energy in detector D2 are rejected as either high energy, side or back penetrating particles in the RADHEPT-LE binning logic. The bottom panel of Figure 5.9 shows RADHEPT-LE's channel binning efficiency for protons in energy bins up to 8 MeV.

RADHEPT-LE is irradiated with an isotropic source in Geant4 simulations to determine its energy-dependent geometric factor for protons. The same Geant4 simulation set up as described in Section 3.3.2 is used. Protons with energies from 0.1 to 10 MeV at a 0.05 MeV step size and 10,000,000 protons per step are simulated. From this simulation, the energy-dependent channel geometric factor can be calculated, and this is shown in Figure 5.10.

Table 5.10: RADHEPT-LE proton binning logic.

Energy channel number	Energy channel range (MeV)	Min. D1 energy deposition (MeV)	Max. D1 energy deposition (MeV)	Other conditions (keV)
1	1-1.3	0.04	0.5	D0 >100, D2 <40
2	1.3-1.6	0.5	1	D0 >100, D2 <40
3	1.6-2.0	1	1.5	D0 >100, D2 <40
4	2.0-2.5	1.5	2.0	D0 >100, D2 <40
5	2.5-2.9	2.0	2.5	D0 >100, D2 <40
6	2.9-3.4	2.5	3.0	D0 >100, D2 <40
7	3.4-3.8	3.0	3.5	D0 >100, D2 <40
8	3.8-4.2	3.5	4.0	D0 >100, D2 <40
9	4.2-4.7	4.0	4.5	D0 >100, D2 <40
10	4.7-5.3	4.5	5.0	D0 >100, D2 <40
11	5.3-5.7	5.0	5.5	D0 >100, D2 <40
12	5.7-6.2	5.5	6.0	D0 >100, D2 <40
13	6.2-6.7	6.0	6.5	D0 >100, D2 <40
14	6.7-7.2	6.5	7.0	D0 >100, D2 <40
15	7.2-7.7	7.0	7.5	D0 >100, D2 <40
16	7.7-8.2	7.5	8.0	D0 >100, D2 <40

Figure 5.10 shows that RADHEPT-LE is able to measure protons with energies from 1 to 8.0 MeV. As mentioned above, protons travelling through the aperture within RADHEPT-LE's required proton energy range below 8 MeV do not deposit energy into RADHEPT-LE's third detector. Therefore, signals in the third detector provide a method to detect backwards travelling particles. Figure 5.10 shows the geometric factor for proton energies up to 10 MeV. If tungsten shielding is used, the minimum thickness (0.5 cm) around the detectors is able to block protons up to around 70 MeV, the vast majority of the expected incident proton flux. If the anti-coincidence enclosure is used, it will be able to detect all side penetrating protons. Therefore, it is expected that RADHEPT-LE's overall response to isotropic proton flux will be very similar for both tungsten or anti-coincidence scintillator enclosures.

5.2.3 RADHEPT-LE Electron Response

On-axis Geant4 simulations are used to determine RADHEPT-LE's response to electrons. An electron pencil beam with energies from 0.01 to 5 MeV, in 0.01 MeV steps, and 1000 electrons per step, travelling directly through the entrance aperture of RADHEPT-LE is simulated in Geant4. The top panel

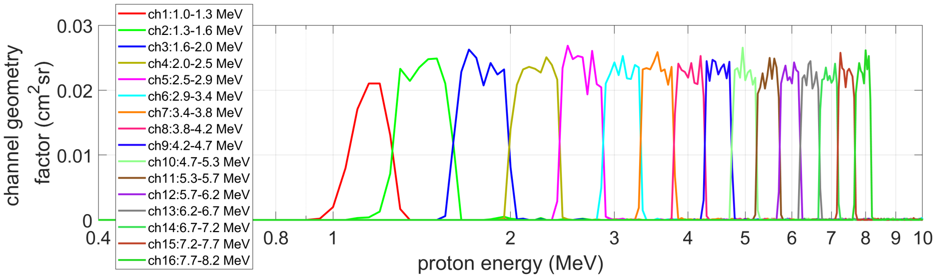

Figure 5.10: Geant4 simulations of the RADHEPT-LE proton response to an isotropic source. RADHEPT-LE's energy-dependent geometric factor per energy channel as a function of proton energy. The data plotted is from an isotropic proton source simulated in Geant4.

Table 5.11: RADHEPT-LE electron binning logic.

Energy channel number	Energy channel range (keV)	Min. D1 energy deposition (MeV)	Max. D1 energy deposition (MeV)	Other conditions (keV)
1	0.08-0.2	0.04	0.2	D0 <100, D2 <40
2	0.2-0.3	0.2	0.3	D0 <100, D2 <40
3	0.3-0.4	0.3	0.4	D0 <100, D2 <40
4	0.4-0.6	0.4	0.6	D0 <100, D2 <40
5	0.6-0.8	0.6	0.8	D0<100, D2 <40
6	0.8-1.0	0.8	1.0	D0 <100, D2 <40

of Figure 5.11 shows the average energy deposition as a function of electron energy per detector. The bottom panel shows the channel efficiency as a function of electron energy. The electron binning logic is shown in Table 5.11.

As shown in Figure 5.11, there is very little average energy deposition in detector D0. Typically, electrons do not deposit energy larger than around 0.02 MeV in the D0 detector. As mentioned, if a particle deposits a signal >100 keV in D0 detector it is assumed to be a proton. RADHEPT-LE's third, high energy threshold detector is used to distinguish high energy electrons travelling through the D0 without stopping. Particles which deposit more than 40 keV into the third detector are rejected by the RADHEPT-LE binning logic, see Table 5.11. Electron energies above 1 MeV are measured by RADHEPT-HE. As Figure 5.11 shows, RADHEPT-LE is able to measure electrons with energies from 0.08 to 1 MeV, covering the low electron energy range required for the RADHEPT instrument suite.

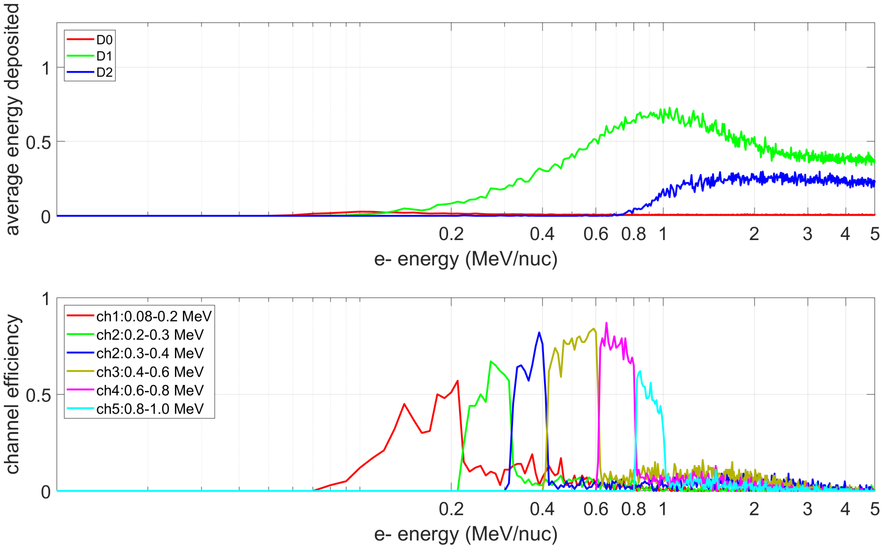

Figure 5.11: Top panel: Average energy deposition as a function of electron energy per detector in RADHEPT-LE from an electron pencil beam travelling on-axis through RADHEPT-LE's aperture in Geant4. Bottom panel: axial channel efficiency as a function of electron energy for a pencil beam of electrons travelling on-axis through RADHEPT-LE's entrance aperture.

RADHEPT-LE Enclosure Trade Study

As a secondary option to side and back shielding, an anti-coincidence scintillator similar to what is proposed for RADHEPT-HE is considered for RADHEPT-LE. As the RADHEPT instrument and the RADICALS mission matures, a final decision on RADHEPT-LE's enclosure can be made.

Figure 5.12 compares the Geant4 schematics for the tungsten shielding and anti-coincidence scintillator options for the RADHEPT-LE instrument enclosure. The anti-coincidence scintillator model has an aluminum entrance cone and side wall, dense material such as tungsten is not required for additional shielding. The 0.5 cm thick tungsten shielding has a mass of 338 grams, and it is expected that the anti-coincidence scintillator and photon detection electronics will be less massive than the tungsten shielding. The mass of the scintillator and required electronics can only be estimated currently as its design is preliminary. The scintillator option will increase RADHEPT-LE's design complexity and power draw during operation.

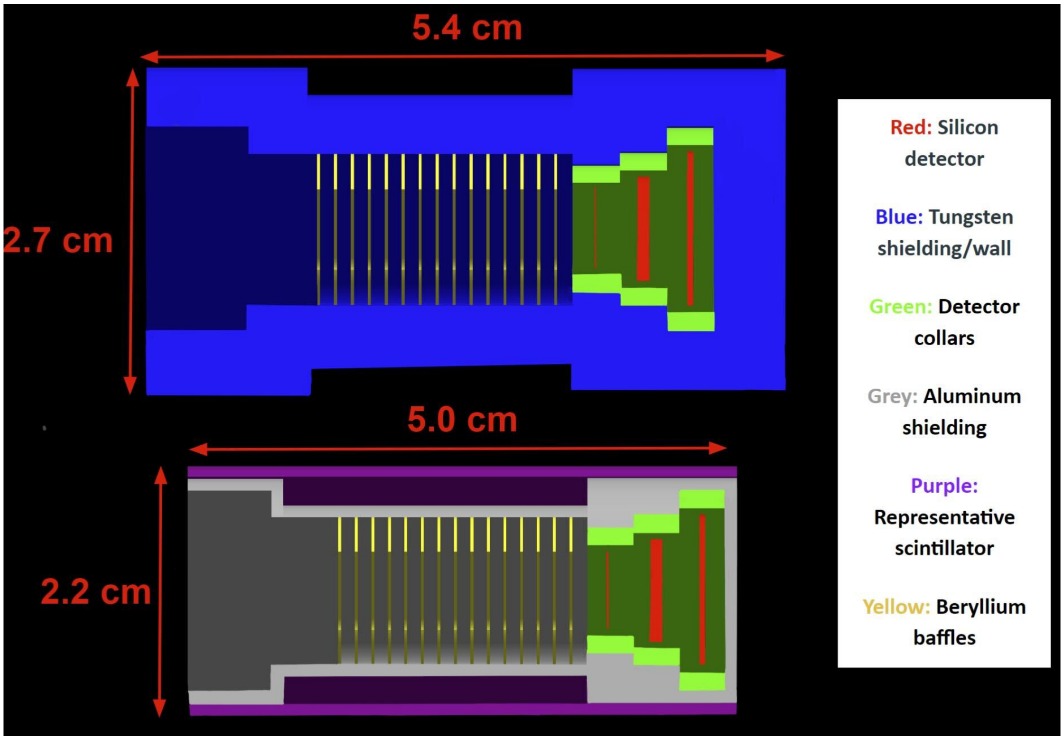

Figure 5.12: Geant4 schematic comparing the layout of RADHEPT-LE with the tungsten shielding (top) and anti-coincidence scintillator enclosure (bottom).

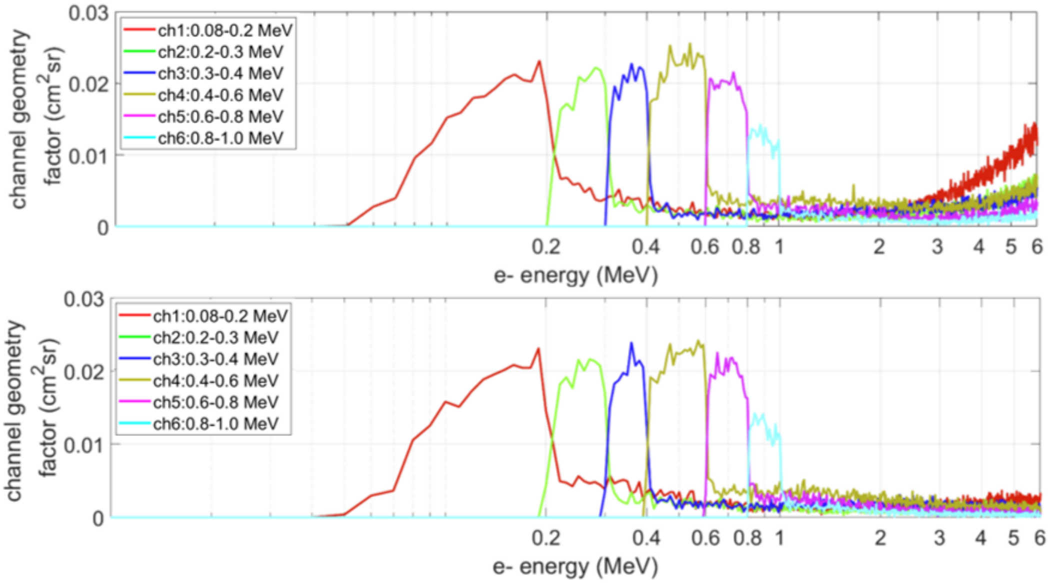

Figure 5.13: Geant4 simulations of the RADHEPT-LE electron response to an isotropic source. Top panel: energy-dependent geometric factor as a function of electron energy for RADHEPT-LE with 0.5 cm tungsten shielding. Bottom panel: energy-dependent geometric factor as a function of electron energy for RADHEPT-LE with the anti-coincidence scintillator design. The data in both plots is from an isotropic electron source simulated in Geant4.

An isotropic electron source is inflicted on RADHEPT-LE instrument with both the options of tungsten shielding and anti-coincidence scintillator enclosures in Geant4. An identical set up to that is described in Section 3.3.2 is used, however electrons with energies from 0.01 to 6 MeV, with 0.01 MeV steps, and 10,000,000 electrons at each step, are simulated. The top panel of Figure 5.13 shows the channel geometric factor against electron energy for RADHEPT-LE with the tungsten enclosure, and the bottom panel shows the results for RADHEPT-LE with the anti-coincidence scintillator.

As Figure 5.13 shows, the 0.5 cm thick tungsten shielding enclosure is only able to effectively reject side penetrating electrons with energies below about 3 MeV as the channel geometric factor begins to increase in all energy channels with increasing electron energy, particularly in channel one. As expected, the bottom panel shows that the anti-coincidence scintillator is able to measure a similar rate off-axis particles over the entire simulated energy range. In both cases, a relatively large percentage of higher energy electrons travelling through the FOV are still sorted into the lower energy bins. In these cases, the higher energy particles may be scattering after depositing energy in detector D1, and do not reach the high energy threshold detector D2. Since only one of RADHEPT-LE's detectors is used for energy identification, there is less data available for the binning logic to identify the electron energy than in the design of RADHEPT-HE. RADHEPT-LE's response to isotropic electron flux outside the cone angle of the front FOV may be acceptable to still achieve its science objectives, as corrections could be made to the measured count rates if RADHEPT-LE's response to the full angular-dependent flux is measured.

5.3 RADHEPT Summary and Future Work

This chapter details the RADHEPT instrument suite, comprised of a low and a high energy head, designed to measure the large range of electron and proton flux required to make pitch angle resolved measurements across the particle energies found in the Van Allen belts. In the design presented, RADHEPT-HE has a 0.2 cm^{2}sr geometric factor, and is able to measure electrons with energies from 0.3 to 4.4 MeV, and protons with energies from 8 MeV to 70 MeV. The upper energy range is well above RADHEPT's electron measurement requirement of 3 MeV, and proton measurement requirement and goal of 20 and 40 MeV, respectively. A simple entrance cone design is proposed, and a method to distinguish between lower energy electron and protons is introduced. Electron and proton isotropic Geant4 simulations show the geometric factor of RADHEPT-HE is within reasonable limits of 0.2 cm^{2}sr over the entire requirement and goal energy range. An anti-coincidence scintillator is introduced into the RADHEPT-HE design to detect side penetrating particles, in lieu of thick side and tungsten back shielding. The anti-coincidence scintillator provides protection against off-axis particles of all energies, and may reduce the mass of the instrument as heavy side and back shielding is no longer required.

The design presented for RADHEPT-LE has a 0.02 cm^{2}sr geometric factor and is capable of measuring electrons with energies from 0.08 to 1 MeV, and protons with energies from 1 to 8.0 MeV. These energy ranges sufficiently cover RADHEPT's lower energy electron and proton measurement requirements. The RADHEPT-LE geometry is similar to RADHEPT-HE's geometry but differs in the number and size of detectors. Tungsten shielding and an anti-coincidence scintillator are the two enclosure designs under consideration for RADHEPT-LE. The tungsten shielding is the simplest to implement in the hardware, but adds additional mass and cannot reject high energy particles. The anti-coincidence scintillator introduces additional complexity to RADHEPT-LE's mechanical and embedded systems design, but it is able to reject side penetrating particles at all electron energies. RADHEPT-LE uses signals in detector D0 to distinguish between electrons and protons, D1 for energy deposition measurements, and D2 as a high energy threshold detector. Since it uses only one detector to measure energy deposition, higher energy particles can scatter and deposit less than nominal energy deposition in D1, causing higher energy particles to be sorted into a lower energy channel. Given the rapid decrease in incident flux at proton and electron energies increase, this reduction in quality may be acceptable for RADHEPT-LE's instrument performance. As the design of the spacecraft matures, a final decision on this trade-off can be made.

Some additional work is required to develop the RADHEPT design from where it currently stands. This includes: modeling the anti-coincidence scintillator, with appropriate optical properties, sensor placement, and efficiencies, and calculating its response to off-axis particles. A comprehensive dead time analysis, similar to what was completed for P-SWEPT in Section 4.3.2, is required to determine if the scintillators of the surface area to be used in RADHEPT-HE, and potentially also in RADHEPT-LE, will saturate during conditions with the worst case particle flux. A detailed optimization study on the number and thickness of baffles, and material for the entrance cone is also required. The entrance cone geometry may also be modified to increase its ability to reject off-axis electrons. The noise floor of the detectors and scintillators require further characterization, and any resulting changes to the binning logic will be made. The work presented in this chapter is considered preliminary, as the layout of the RADICALS spacecraft, mission operations, and expected electron and proton fluxes continue to be refined. RADHEPT-LE's detector layout and binning algorithms may also need to be revisited in an attempt to reduce the amount of high energy electrons sorted into lower energy channels. Nevertheless, the work presented here demonstrates the validity of the RADHEPT design.

Changes to the missions objectives, mass and power budgets, or mission operations may require further modifications to the instrument design such as the entrance cone size and geometry, geometric factor, or detector number. However, the work completed here provides a strong basis for an energetic particle instrument suite and data processing regime which meets the requirements of the RADICALS mission.

Chapter 6

Conclusion

This thesis outlines advances in the design and development of the layout and energy identification algorithms for three energetic particle telescope instruments, LL-SWEPT, P-SWEPT and RADHEPT, designed for the lunar surface, Lunar Gateway, and LEO missions, respectively. The basis for this work is derived from previous designs of energetic particle instruments developed at the UofA, and makes use of Geant4 simulations to validate instrument performance and inform design trades.

All three instrument suites are designed to be capable of angularly resolved particle measurements, and do so with an instrument design based on a stack of silicon detectors. The layout of each instrument is designed to measure the energetic particles observable from their vantage points in near-Earth and interplanetary space. The geometric factors of each instrument are optimized to resolve the minimum expected count rates in each particle environment, while ensuring the instrument dead time is at appropriate levels during the maximum worst case particle fluxes. Each instrument employs methods within its design and energy identification algorithms to reject particles travelling outside the FOV. P-SWEPT and LL-SWEPT are required to measure a higher energy range so degraders are placed between the detectors to increase the energy range of protons and alpha particles stopping and coming to rest in the detector stack. RADHEPT prioritizes the measurement of electrons, which scatter significantly as they travel through detector substrates and degraders. To minimize scattering and improve energy identification efficiency, RADHEPT does not have degraders between its detectors. RADHEPT is comprised of a low energy and a high energy head, whose geometric factors are set to measure the count rates of the lower and higher energy electrons and protons in the Van Allen belts. Geant4 simulations are used to determine the instrument's ability to shield off-axis particles and to test the particle energy identification algorithms.

LL-SWEPT's design, particularly the detector layout and shielding, are optimized for a short 14-day mission in sunlit conditions on the surface of the moon. To keep its mass low, LL-SWEPT's shielding is kept to the minimum amount expected to ensure the instrument's structural integrity and to adequately shield the detectors from the expected particle flux during a 14-day period on the lunar surface. LL-SWEPT's response to protons and alpha particles is characterized here using Geant4 simulations. Two methods of particle energy identification are proposed, designed to measure both low and high energy protons. Lower energy particles are sorted into an energy channel if they deposit energy within certain thresholds in each detector. Higher energy particles have a larger distribution in energy deposition in the detectors and they deposit energy into a higher number of detectors, both of which make this energy identification regime less efficient.

The energy depositions in each detector for high energy particles are also compared to energy thresholds per detector. Instead of assigning particles if their energy deposition falls into the detection energy range in every detector, they are assigned to the energy channel in which most of their energy depositions fall within the appropriate range. Particles are initially sorted into the low and high energy identification regimes based on their energy deposition and the number of detectors which energy is deposited in. It is shown that the direction of propagation of high energy protons can also be identified by calculating the linear slope of the energy deposition as a function of detector number in the stack. This sign check is used to determine and reject particles travelling through the back of the instrument which can mimic the energy deposition signals of high energy particles travelling through the aperture at the front of the instrument. Using the combined low and high energy regimes, along with the sign check, protons with energies from 20 to 370 MeV can be efficiently identified from LL-SWEPT data. LL-SWEPT is designed to have a 1.3 $\mathrm{cm^2sr}$ geometric factor, and Geant4 isotropic proton simulations presented here show that LL-SWEPT maintains an energy-dependent channel geometric factor close to the target of 1.3 $\mathrm{cm^2sr}$, depending on the binning efficiency of each channel.

The P-SWEPT instrument is designed to have a 0.113 $\mathrm{cm^2sr}$ geometric factor and has thicker shielding than LL-SWEPT, as it is much more probable that P-SWEPT will observe a large SEP event during its five-year mission. P-SWEPT is equipped with two detectors immediately behind the entrance cone to efficiently measure electrons, which have been shown to precede proton flux in SEP events by up to one hour and which could be used as a potential early warning signal for astronaut radiation risk from the proton event. Geant4 on-axis simulations show P-SWEPT's ability to measure protons with energies from 22 MeV up to 400 MeV, extending past the 20 to 300 MeV measurement requirement, and electrons with energies from 0.3 up to 1.5 MeV.

The RADHEPT instrument is required to measure electrons from 0.1 to 3 MeV, and protons from 1 to 20 MeV in the low-Earth orbit of the RADICALS mission. To measure across this large energy range and resolve the range of their associated count rates, the RADHEPT detector is separated into two heads, RADHEPT-HE (high energy) and RADHEPT-LE (low energy). RADHEPT-HE is able to measure protons from 8 to 70 MeV, and electrons from 0.3 to 4.4 MeV with a 0.2 $\mathrm{cm^2sr}$ geometric factor. RADHEPT-LE is designed to measure electrons from 0.08 to 1 MeV and protons from 1 to 8.0 MeV with a 0.02 $\mathrm{cm^2sr}$ geometric factor. On-axis and isotropic Geant4 simulations are used to determine both the instrument's binning efficiency and energy-dependent geometric factors. Tantalum baffles are used to deflect scattered particles travelling through the aperture. Electrons and protons are differentiated by the signals each particle deposits in the first, thin silicon detector. The detectors within RADHEPT-HE are enclosed with a hollow cylindrical scintillator to detect off-axis particles travelling through the sides of the instrument. Design considerations for RADHEPT-LE's enclosure include either an anti-coincidence scintillator or a 0.5 cm thick tungsten shielding. Based on the expected count rates, the actual RADICALS spacecraft layout, and available mass, and after power and data down link budgets for the instruments are finalized, a decision on the final enclosure design can be made.

The future work regarding the next steps of the detailed design and analysis of each instrument are explained at the end of the relevant chapters. Each instrument is on a separate mission development timeline for flight qualification. RADHEPT will continue development at the UofA in preparation for the RADICALS spacecraft integration in 2024. The RADICALS spacecraft is currently in its design phase, and the spacecraft bus design and integration will be led by the University of Toronto's Space Flight Laboratories. P-SWEPT development will continue, hopefully with ongoing support from the Canadian Space Agency (CSA) towards a potential mission on the Lunar Gateway platform. An engineering model prototype of P-SWEPT will be shortly tested at the TRIUMF proton beam facility, to test P-SWEPT's proton identification algorithms and the functionality of its electronics. At the time of writing, LL-SWEPT development is not currently being funded further. However, in the future, should there be interest in particle measurements from the lunar surface, LL-SWEPT's design is a viable option as a payload for a future lunar station.

In summary, baseline designs for high energy proton and electron detectors have been presented and their performance characteristics tested for three different mission environments using Geant4 and other forms of analysis. In each case, the results demonstrate that the mission objectives can be met using the baseline designs which are all based on a telescopic approach using a stack of silicon detectors. Future work will be required to carry out final optimization of the designs for the these instruments in advance of their flight on missions to low-Earth orbits, to deep space, and to the moon. Future opportunities may also present themselves to fly on missions to Mars or beyond.

References

Agostinelli, S., Allison, J., Amako, K., Apostolakis, J., Araujo, H., Arce, P., Asai, M., Axen, D., Banerjee, S., Barrand, G., Behner, F., Bellagamba, L., Boudreau, J., Broglia, L., Brunengo, A., Burkhardt, H., Chauvie, S., Chuma, J., Chytracek, R., … Zschiesche, D. (2003). Geant4—a simulation toolkit. *Nuclear Instruments and Methods in Physics Research Section A: Accelerators, Spectrometers, Detectors and Associated Equipment*, *506*(3), 250–303. https://doi.org/10.1016/S0168-9002(03)01368-8.

Allison, J., Amako, K., Apostolakis, J., Arce, P., Asai, M., Aso, T., Bagli, E., Bagulya, A., Banerjee, S., Barrand, G., Beck, B., Bogdanov, A., Brandt, D., Brown, J., Burkhardt, H., Canal, P., Cano-Ott, D., Chauvie, S., Cho, K., … Yoshida, H. (2016). Recent developments in Geant4. *Nuclear Instruments and Methods in Physics Research Section A: Accelerators, Spectrometers, Detectors and Associated Equipment*, *835*, 186–225. https://doi.org/10.1016/j.nima.2016.06.125.

Chancellor, J. C., Blue, R. S., Cengel, K. A., Auñón-Chancellor, S. M., Rubins, K. H., Katzgraber, H. G., & Kennedy, A. R. (2018). Limitations in predicting the space radiation health risk for exploration astronauts. *npj Microgravity*, *4*(1), 8. https://doi.org/10.1038/s41526-018-0043-2.

Chen, F. F. (2016). Single-Particle Motions. In F. F. Chen (Ed.), *Introduction to Plasma Physics and Controlled Fusion* (pp. 19–49). Springer International Publishing. https://doi.org/10.1007/978-3-319-22309-4_2.

Cranmer, S. R. (2005). Why is the Fast Solar Wind Fast and the Slow Solar Wind Slow? *"Proceedings of the Solar Wind 11 / SOHO 16, "Connecting Sun and Heliosphere" Conference (ESA SP-592).*, *592*, 5. Retrieved April 29, 2022, from https://ui.adsabs.harvard.edu/abs/2005ESASP.592..159C.

Dunai, T. J. (Ed.). (2010). Cosmogenic nuclides. In *Cosmogenic Nuclides: Principles, Concepts and Applications in the Earth Surface Sciences* (pp. 25–59). Cambridge University Press. https://doi.org/10.1017/CBO9780511804519.003.

Fennell, J. F., Claudepierre, S. G., Blake, J. B., O'Brien, T. P., Clemmons, J. H., Baker, D. N., Spence, H. E., & Reeves, G. D. (2015). Van Allen Probes show that the inner radiation zone contains no MeV electrons:

ECT/MagEIS data. *Geophysical Research Letters*, *42*(5), 1283–1289. https://doi.org/https://doi.org/10.1002/2014GL062874.

Fiori, R. A. D. (2020). *Detailed explanation of modelling absorption due to polar cap absorption and shortwave fadeout* (tech. rep. Open File 8704). Geological Survey of Canada. Ottawa, Ontario. https://doi.org/10.4095/321793.

Gerbase, A. E., & Oliveira, Camila Reis de. (2012). Reciclagem do Lixo de Informatica: Uma Oportunidade Para a Quimica. *Quim. Nova*, *35*(7), 6.

Grdanovska, S. (2015). *Characterization of Radiation Damage to a Novel Photonic Crystal Sensor* (PhD Thesis). University of Maryland, College Park. Maryland, USA. https://doi.org/10.13016/M2BZ0D.

Hargreaves, J. (1992). *The Solar-Terrestrial Environment: An Introduction to Geospace - the Science of the Terrestrial Upper Atmosphere, Ionosphere, and Magnetosphere* (Vol. 5). Cambridge University Press. https://doi.org/10.1017/CBO9780511628924.

Hassler, D. M., Zeitlin, C., Wimmer-Schweingruber, R. F., Böttcher, S., Martin, C., Andrews, J., Böhm, E., Brinza, D. E., Bullock, M. A., Burmeister, S., Ehresmann, B., Epperly, M., Grinspoon, D., Köhler, J., Kortmann, O., Neal, K., Peterson, J., Posner, A., Rafkin, S., . . . Cucinotta, F. A. (2012). The Radiation Assessment Detector (RAD) Investigation. *Space Science Reviews*, *170*(1-4), 503–558. https://doi.org/10.1007/s11214-012-9913-1.

Heilbronn, L., Nakamura, T., Iwata, Y., Kurosawa, T., Iwase, H., & Townsend, L. W. (2005). Overview of secondary neutron production relevant to shielding in space. *Radiation Protection Dosimetry*, *116*(1-4), 140–143. https://doi.org/10.1093/rpd/nci033.

Janni, J. F. (1982). Energy loss, range, path length, time-of-flight, straggling, multiple scattering, and nuclear interaction probability. *Atomic Data and Nuclear Data Tables*, *27*(2-3), 147–339. https://doi.org/10.1016/0092-640X(82)90004-3.

Jiggens, P., Heynderickx, D., Sandberg, I., Truscott, P., Raukunen, O., & Vainio, R. (2018). Updated Model of the Solar Energetic Proton Environment in Space. *Journal of Space Weather and Space Climate*, *8*, A31. https://doi.org/10.1051/swsc/2018010.

Kersten, T., Horne, R. B., Glauert, S. A., Meredith, N. P., Fraser, B. J., & Grew, R. S. (2014). Electron losses from the radiation belts caused by EMIC waves. *Journal of Geophysical Research: Space Physics*, *119*(11), 8820–8837. https://doi.org/10.1002/2014JA020366.

Kilifarska, N. A., Bakhmutov, V. G., & Melnyk, G. V. (2020). Galactic cosmic rays and solar particles in Earth's atmosphere. In *The Hidden Link between Earth's Magnetic Field and Climate* (pp. 101–131). Elsevier. https://doi.org/https://doi.org/10.1016/B978-0-12-819346-4.00005-X.

Klecker, B. (2013). Current understanding of SEP acceleration and propagation. *Journal of Physics: Conference Series*, *409*(1), 012015. https://doi.org/10.1088/1742-6596/409/1/012015.

Li, W., & Hudson, M. (2019). Earth's Van Allen Radiation Belts: From Discovery to the Van Allen Probes Era. *Journal of Geophysical Research: Space Physics*, *124*(11), 8319–8351. https://doi.org/https://doi.org/10.1029/2018JA025940.

Lin, R. P., Anderson, K. A., Ashford, S., Carlson, C., Curtis, D., Ergun, R., Larson, D., McFadden, J., McCarthy, M., Parks, G. K., Rme, H., Bosqued, J. M., Coutelier, J., Cotin, F., D'Uston, C., Wenzel, K. .-., Sanderson, T. R., Henrion, J., Ronnet, J. C., & Paschmann, G. (1995). A Three-dimensional Plasma and Energetic Particle Investigation for the WIND Spacecraft. *Space Science Reviews*, *71*(1-4), 125–153. Retrieved September 19, 2022, from http://link.springer.com/10.1007/BF00751328.

Lutz, G., & Klanner, R. (2020). Solid State Detectors. In H. Schopper (Ed.), *Particle Physics Reference Library* (pp. 137–200). Springer, CHam. https://doi.org/10.1007/978-3-030-35318-6_5.

Malandraki, O. E., & Crosby, N. B. (2018). Solar Energetic Particles and Space Weather: Science and Applications. In O. E. Malandraki & N. B. Crosby (Eds.), *Solar Particle Radiation Storms Forecasting and Analysis* (pp. 1–26). Springer Cham. https://doi.org/10.1007/978-3-319-60051-2_1.

Matsumoto, H., Koshiishi, H., Goka, T., Kimoto, Y., Green, B., Galica, G., Nakamura, T., Abe, T., Badono, S., Murata, S., & Sullivan, J. (2001). Compact, lightweight spectrometer for energetic particles. *IEEE Transactions on Nuclear Science*, *48*(6), 2043–2049. https://doi.org/10.1109/23.983170.

Micron Semiconductor Ltd. Silicon Catalouge Long Form. (2018). Retrieved May 1, 2021, from http://www.micronsemiconductor.co.uk/wp-content/uploads/2018/03/2018-Micron-Semiconductor-Ltd-Silicon-Catalogue_Long-Form.pdf.

Naito, M., Kodaira, S., Ogawara, R., Tobita, K., Someya, Y., Kusumoto, T., Kusano, H., Kitamura, H., Koike, M., Uchihori, Y., Yamanaka, M., Mikoshiba, R., Endo, T., Kiyono, N., Hagiwara, Y., Kodama, H., Matsuo, S., Takami, Y., Sato, T., & Orimo, S.-i. (2020). Investigation of shielding material properties for effective space radiation protection. *Life Sciences in Space Research*, *26*, 69–76. https://doi.org/10.1016/j.lssr.2020.05.001.

Northrop, T. G. (1963). Adiabatic charged-particle motion. *Reviews of Geophysics*, *1*(3), 283. https://doi.org/10.1029/RG001i003p00283.

Núñez, M. (2015). Real-time prediction of the occurrence and intensity of the first hours of greater than 100 MeV solar energetic proton events. *Space Weather*, *13*(11), 807–819. https://doi.org/10.1002/2015SW001256.

Parker, E. (1959). Extension of the Solar Corona into Interplantary Space. *Journal of Geophysical Research*, *64*(11), 7.

Posner, A. (2007). Up to 1-hour forecasting of radiation hazards from solar energetic ion events with relativistic electrons: *Space Weather*, *5*(5), 28. https://doi.org/10.1029/2006SW000268.

Rodger, C. J., Clilverd, M. A., Green, J. C., & Lam, M. M. (2010). Use of POES SEM-2 observations to examine radiation belt dynamics and energetic electron precipitation into the atmosphere. *Journal of Geophysical Research: Space Physics*, *115*(A4), 13. https://doi.org/https://doi.org/10.1029/2008JA014023.

Ross, E., & Chaplin, W. J. (2019). The Behaviour of Galactic Cosmic-Ray Intensity During Solar Activity Cycle 24. *Solar Physics*, *294*, 17. https://doi.org/10.1007/s11207-019-1397-7.

Sadiq, F. (2012). *High Energy Proton Telescope* (Master's thesis). University of Alberta. Retrieved April 4, 2022, from https://ui.adsabs.harvard.edu/abs/2012MsT.........16S.

Schiller, Q. G., Mahendrakumar, A., & Li, X. (2010). REPTile: A Miniaturized Detector for a CubeSat Mission to Measure Relativistic Particles in Near-Earth Space. *Connecting the Dots: Bringing Visionaries, System Implementers & Mission Sponsors Together*, 12. Retrieved September 26, 2022, from https://digitalcommons.usu.edu/smallsat/2010/all2010/43/.

Schumacher, U. (2005). Basics of Plasma Physics. In A. Dinklage, T. Klinger, G. Marx, & L. Schweikhard (Eds.), *Plasma Physics: Confinement, Transport and Collective Effects* (pp. 1–20). Springer Berlin Heidelberg. https://doi.org/10.1007/11360360_1.

Schwadron, N. A., Wilson, J. K., Looper, M. D., Jordan, A. P., Spence, H. E., Blake, J. B., Case, A. W., Iwata, Y., Kasper, J. C., Farrell, W. M., Lawrence, D. J., Livadiotis, G., Mazur, J., Petro, N., Pieters, C., Robinson, M. S., Smith, S., Townsend, L. W., & Zeitlin, C. (2016). Signatures of volatiles in the lunar proton albedo. *Icarus*, *273*, 25–35. https://doi.org/https://doi.org/10.1016/j.icarus.2015.12.003.

Selesnick, R. S., Baker, D. N., Jaynes, A. N., Li, X., Kanekal, S. G., Hudson, M. K., & Kress, B. T. (2014). Observations of the inner radiation belt: CRAND and trapped solar protons. *Journal of Geophysical Research: Space Physics*, *119*(8), 6541–6552. https://doi.org/https://doi.org/10.1002/2014JA020188.

Shprits, Y. Y., Drozdov, A. Y., Spasojevic, M., Kellerman, A. C., Usanova, M. E., Engebretson, M. J., Agapitov, O. V., Zhelavskaya, I. S., Raita, T. J., Spence, H. E., Baker, D. N., Zhu, H., & Aseev, N. A. (2016). Wave-induced loss of ultra-relativistic electrons in the Van Allen radiation belts. *Nature Communications*, *7*(1), 7. https://doi.org/https://doi.org/10.1038/ncomms12883.

Stacy, J. G., & Vestrand, W. T. (2003). Gamma-Ray Astronomy. In R. A. Meyers (Ed.), *Encyclopedia of Physical Science and Technology (Third*

Edition) (Third Edition, pp. 397–432). Academic Press. https://doi.org/https://doi.org/10.1016/B0-12-227410-5/00274-X.

Sullivan, J. D. (1971). Geometrical Factor and Directional Response of Single and Multi-element Particle Telescopes. *Nuclear Instruments and Methods*, *95*(1), 5–11. https://doi.org/10.1016/0029-554X(71)90033-4.

Thorne, R. M., Smith, E. J., Burton, R. K., & Holzer, R. E. (1973). Plasmaspheric hiss. *Journal of Geophysical Research*, *78*(10), 1581–1596. https://doi.org/10.1029/JA078i010p01581.

Turner, D. L., Shprits, Y., Hartinger, M., & Angelopoulos, V. (2012). Explaining sudden losses of outer radiation belt electrons during geomagnetic storms. *Nature Physics*, *8*(3), 208–212. https://doi.org/10.1038/nphys2185.

Walt, M. (1994). *Introduction to Geomagnetically Trapped Radiation* (1st ed.). Cambridge University Press. https://doi.org/10.1017/CBO9780511524981.

Wright, D., & Kelsey, M. (2015). The Geant4 Bertini Cascade. *Nuclear Instruments and Methods in Physics Research Section A: Accelerators, Spectrometers, Detectors and Associated Equipment*, *804*, 175–188. https://doi.org/10.1016/j.nima.2015.09.058.

Wurz, P. (2005). Solarwind Composition. In D. Danesy, S. Poedts, A. de Groof, & J. Andries (Eds.), *The Dynamic Sun: Challenges for Theory and Observations (ESA SP-600)* (p. 9). ESA Publications Division.

Yando, K., Millan, R. M., Green, J. C., & Evans, D. S. (2011). A Monte Carlo simulation of the NOAA POES Medium Energy Proton and Electron Detector instrument: TECHNIQUE. *Journal of Geophysical Research: Space Physics*, *116*(A10), 13. https://doi.org/10.1029/2011JA016671.

Zhao, X.-Y., Wang, H.-Y., Wu, F., Meng, X.-C., Ma, Y.-Q., Lu, H., Wang, H., Wang, P., Li, X.-Q., Xu, Y.-B., Shi, F., Jiang, W.-Q., An, Z.-H., Yu, X.-X., & Liu, H.-Y. (2013). A geometric factor calculation method based on the isotropic flux assumption. *Chinese Physics C*, *37*(12), 6. https://doi.org/10.1088/1674-1137/37/12/126201.

Appendix A

Table A.1: LL-SWEPT's energy deposition decision thresholds for detectors D0 to D8, for alpha particles.

Channel 1: 80 -108 MeV/particle									
LL-SWEPT Detector number	D0	D1	D2	D3	D4	D5	D6	D7	D8
Max Energy Deposition	20	50.6	24	0.10	0.10	0.10	0.10	0.10	0.10
Min Energy Deposition	8.41	16.0	0.10	0	0	0	0	0	0
Channel 2: 108-146 MeV/particle									
Max Energy Deposition	11.12	27.68	50.60	17.63	0.10	0.10	0.10	0.10	0.10
Min Energy Deposition	5.84	12.68	15.55	0.10	0	0	0	0	0
Channel 3: 146-197.2 MeV/particle									
Max Energy Deposition	7.72	16.76	20.57	50.60	14.08	0.10	0.10	0.10	0.10
Min Energy Deposition	4.35	9.05	9.83	12.30	0.10	0	0	0	0
Channel 4: 197-266 MeV/particle									
Max Energy Deposition	5.76	11.97	13.00	16.27	50.60	11.16	0.10	0.10	0.10
Min Energy Deposition	3.33	6.80	7.08	7.75	9.67	0.10	0	0	0
Channel 5: 266-360 MeV/particle									
Max Energy Deposition	4.41	8.99	9.36	10.25	12.74	50.60	8.80	0.10	0.10
Min Energy Deposition	2.62	5.29	5.40	5.65	6.18	7.63	0.10	0	0
Channel 6: 360-484 MeV/particle									
Max Energy Deposition	3.46	7.00	7.15	7.48	8.17	10.10	50.60	7.04	0.10
Min Energy Deposition	2.084	4.20	4.25	4.35	4.55	4.95	6.12	0.10	0
Channel 7: 484-658 MeV/particle									
Max Energy Deposition	2.76	5.55	5.62	5.75	6.01	6.54	8.09	50.60	5.64
Min Energy Deposition	1.68	3.38	3.40	3.44	3.52	3.67	4.00	4.90	0.10
Channel 8: >658 MeV/particle									
Max Energy Deposition	2.23	4.47	4.50	4.56	4.66	4.86	5.29	6.48	50.60
Min Energy Deposition	1.38	2.77	2.78	2.80	2.84	2.90	3.02	3.27	3.98

Table A.2: P-SWEPT's energy deposition decision thresholds for detectors D0 to D9, for protons.

Channel 1: 22-27 MeV/nuc										
P-SWEPT Detector number	D0	D1	D2	D3	D4	D5	D6	D7	D8	D9
Max Energy Deposition	23.00	0.10	0.10	0.10	0.10	0.10	0.10	0.10	0.10	0.10
Min Energy Deposition	0.10	0.00	0.00	0.00	0.00	0.00	0.00	0.00	0.00	0.00
Channel 2: 27-36.5MeV/nuc										
Max Energy Deposition	10.85	7.20	12.65	0.10	0.10	0.10	0.10	0.10	0.10	0.10
Min Energy Deposition	7.38	3.12	0.10	0.00	0.00	0.00	0.00	0.00	0.00	0.00
Channel 3: 36.5-49.3 MeV/nuc										
Max Energy Deposition	8.79	4.54	8.08	12.65	0.10	0.10	0.10	0.10	0.10	0.10
Min Energy Deposition	5.94	2.36	5.15	0.10	0.00	0.00	0.00	0.00	0.00	0.00
Channel 4: 49.3-66.6 MeV/nuc										
Max Energy Deposition	5.46	5.46	2.05	4.53	5.65	12.65	0.10	0.10	0.10	0.10
Min Energy Deposition	4.38	1.51	3.30	3.64	0.10	0.00	0.00	0.00	0.00	0.00
Channel 5: 66.6-90 MeV/nuc										
Max Energy Deposition	4.38	1.51	3.30	3.64	4.95	12.65	0.10	0.10	0.10	0.10
Min Energy Deposition	3.27	1.11	2.27	2.38	2.61	0.10	0.00	0.00	0.00	0.00
Channel 6: 90-121.6 MeV/nuc										
Max Energy Deposition	3.27	1.11	2.27	2.38	2.61	3.32	12.65	0.10	0.10	0.10
Min Energy Deposition	2.60	0.90	1.81	1.82	1.91	2.11	0.10	0.00	0.00	0.00
Channel 7: 121.6-164.4 MeV/nuc										
Max Energy Deposition	2.60	0.90	1.81	1.82	1.91	2.11	2.76	12.65	0.10	0.10
Min Energy Deposition	2.16	0.72	1.44	1.44	1.44	1.44	1.66	0.10	0.00	0.00